NASA/TM–20210022214

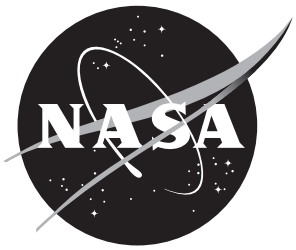

Identification of Best Practices for Predicting Inlet Performance Using FUN3D Part 2: Installed Inlets.

Michael D. Bozeman Jr. and Jan-Renee Carlson
Langley Research Center, Hampton, Virginia

March 2022

NASA STI Program Report Series

Since its founding, NASA has been dedicated to the advancement of aeronautics and space science. The NASA scientific and technical information (STI) program plays a key part in helping NASA maintain this important role.

The NASA STI program operates under the auspices of the Agency Chief Information Officer. It collects, organizes, provides for archiving, and disseminates NASA's STI. The NASA STI program provides access to the NTRS Registered and its public interface, the NASA Technical Reports Server, thus providing one of the largest collections of aeronautical and space science STI in the world. Results are published in both non-NASA channels and by NASA in the NASA STI Report Series, which includes the following report types:

- TECHNICAL PUBLICATION. Reports of completed research or a major significant phase of research that present the results of NASA Programs and include extensive data or theoretical analysis. Includes compilations of significant scientific and technical data and information deemed to be of continuing reference value. NASA counterpart of peer-reviewed formal professional papers but has less stringent limitations on manuscript length and extent of graphic presentations.

- TECHNICAL MEMORANDUM. Scientific and technical findings that are preliminary or of specialized interest, e.g., quick release reports, working papers, and bibliographies that contain minimal annotation. Does not contain extensive analysis.

- CONTRACTOR REPORT. Scientific and technical findings by NASA-sponsored contractors and grantees.

- CONFERENCE PUBLICATION. Collected papers from scientific and technical conferences, symposia, seminars, or other meetings sponsored or co-sponsored by NASA.

- SPECIAL PUBLICATION. Scientific, technical, or historical information from NASA programs, projects, and missions, often concerned with subjects having substantial public interest.

- TECHNICAL TRANSLATION. English-language translations of foreign scientific and technical material pertinent to NASA's mission.

Specialized services also include organizing and publishing research results, distributing specialized research announcements and feeds, providing information desk and personal search support, and enabling data exchange services.

For more information about the NASA STI program, see the following:

- Access the NASA STI program home page at http://www.sti.nasa.gov

- Help desk contact information:

https://www.sti.nasa.gov/sti-contact-form/
and select the "General" help request type.

NASA/TM–20210022214

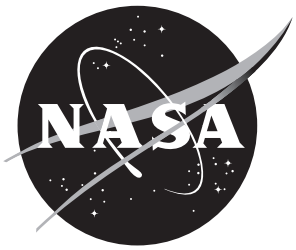

Identification of Best Practices for Predicting Inlet Performance Using FUN3D Part 2: Installed Inlets.

Michael D. Bozeman Jr. and Jan-Renee Carlson
Langley Research Center, Hampton, Virginia

National Aeronautics and
Space Administration

Langley Research Center
Hampton, Virginia 23681-2199

March 2022

Available from:

NASA STI Program / Mail Stop 148
NASA Langley Research Center
Hampton, VA 23681-2199
Fax: 757-864-6500

Abstract

A series of studies were performed to assess the impacts of boundary condition type and placement, grid refinement, and modeling parameters such as turbulence model and flux limiter on the predicted inlet performance for installed inlet configurations using the FUN3D flow solver. Two configurations were considered for the study; a wall-mounted Boundary Layer Ingestion (BLI) inlet and the C607 propulsion model tested in the 8x6 Supersonic Wind Tunnel at the NASA Glenn Research Center. The results of the studies were to be used to recommend best practices, as well as to assess the accuracy of FUN3D for inlet predictions. The results of BLI inlet studies showed a minimal impact of grid refinement on the predicted inlet performance for a constant mass flow rate through the inlet. For the C607 propulsion model, the results showed that while the FUN3D predictions at the Aerodynamic Interface Plane (AIP) qualitatively agree with the experimental data, FUN3D showed a tendency to overpredict the circumferential distortion metric (IDC_{max}) and underpredict both the radial distortion metric (IDR_{max}) and the pressure recovery at the AIP (PR_{AIP}), with the differences between FUN3D and the experimental data increasing with increasing grid refinement and Mach number. Additionally, the outflow boundary location studies performed for both geometries showed that the solution at the AIP was not significantly impacted by the outflow boundary location as long as it was not placed at the location of the AIP. The modeling parameter studies did not indicate a path forward for improved predictions for either inlet configuration. Finally, comparisons between the mass flow plug and outflow geometry versions of the C607 propulsion model illustrated favorable agreement, which indicates that the differences observed are not caused by the outflow boundary model for this problem. This problem poses significant challenges to Reynolds-averaged Navier-Stokes (RANS) solvers due to the presence of shocks and flow separation in the inlet.

Nomenclature

α	angle of attack [deg]
β	angle of sideslip [deg]
$\dot{m}$	mass flow rate [$\mathrm{lb_m/s}$]
γ	ratio of specific heats
θ	circumferential location [deg]
A	area [$\mathrm{in^2}$]
D	diameter of AIP [in]
$DPCP$	ARP1420 circumferential distortion
e	difference between target and actual flow condition
h	refinement factor
IDC_{max}	maximum value of the General Electric circumferential distortion metric, IDC
IDR_{max}	maximum value of the General Electric radial distortion metric, IDR
k_d	derivative weighting term
k_i	integral weighting term
k_p	proportional weighting term
M	Mach number
N	number of grid nodes
O	update equation for PID controller
P	static pressure [$\mathrm{lb/in^2}$ or psi]
P_t	total pressure [$\mathrm{lb/in^2}$ or psi]
PR	Pressure Recovery, $PR = P_t/P_{t,0}$
R	gas constant [ft-$\mathrm{lb_f}$/slug-R]
$r_{1,2}$	boundary layer growth rate parameters
T_t	total temperature [°R]
$W_{C,Plug}$	corrected flow rate [$\mathrm{lb_m/s}$]
x, y, z	coordinate axes [in]

y^+	dimensionless wall spacing
AIP	Aerodynamic Interface Plane
BC	Boundary Condition
BLI	Boundary Layer Ingestion
CFD	Computational Fluid Dynamics
CST	Commercial Supersonic Techology
LRR	Launder, Reece, and Rodi
MFP	Mass Flow Plug
PID	Proportional-Integral-Derivative
QCR	Quadratic Constitutive Relation
RANS	Reynolds-averaged Navier-Stokes
RC	Rotational correction
Re	Unit Reynolds number [per foot or 1/ft]
RSM	Reynolds Stress Model
SA	Spalart-Allmaras one-equation turbulence model
SA-neg	Spalart-Allmaras one-equation turbulence model with negative provisions
SPR	Static pressure ratio, P_{back}/P_∞
SSG	Speziale, Sarkar, and Gatski
SST	Menter Shear Stress Transport two-equation turbulence model
SST-V	Menter Shear Stress Transport two-equation turbulence model with vorticity source term
VG	Vortex Generator

1 Introduction

As part of the NASA Commercial Supersonic Technology (CST) project, an effort was launched to revisit the computational fluid dynamic (CFD) modeling of inlet geometries and flows. The goals of this effort were to investigate the impacts of boundary condition type and placement, grid refinement, and modeling parameters such as turbulence model and flux limiter, when applicable, on the predicted inlet performance. Additionally, the results of the studies were to be used to provide recommendations for best practices for performing inlet predictions. The described studies were separated into two parts. Part 1 focused on the isolated inlet problem, which utilized a "unit" s-duct configuration. Part 2, present work, focuses on the installed inlet problem and considers two inlet configurations; a Boundary Layer Ingestion (BLI) inlet mounted to a wall and the C607 propulsion model that was tested in the 8x6 Supersonic Wind Tunnel at the NASA Glenn Research Center [1].

The major difference between isolated and installed inlets is that isolated inlet simulations employ both inflow and outflow boundary conditions (BCs), while installed inlet simulations typically only employ an outflow BC. For the installed inlet case, the inlet is submerged in an external flow field that is defined by the given flight condition and upstream geometry. Then, the mass flow rate through the inlet is determined by the outflow BC value. The challenge is determining the appropriate outflow BC value to achieve the desired flow settings in the inlet. This work employs three methods for setting the flow condition in the inlet; a fixed static pressure ratio, Mach number, and mass flow rate at the outflow boundary. For the mass flow rate BC, a Proportional-Integral-Derivative (PID) controller developed by Carlson [2] was employed to iteratively update the back pressure at the outflow boundary until the target mass flow rate is achieved.

An overview of the computational methods employed for this work is provided in Section 2. Sections 3 and 4 describe the problem descriptions, results, and discussion for the BLI inlet and C607 propulsion model. Finally, the results of the studies for both configurations are summarized in Section 5.

2 Computational Methods

2.1 FUN3D Flow Solver

FUN3D is an unstructured three-dimensional, implicit, Navier-Stokes code. For all simulations performed, Roe's flux difference splitting [3] was used for the calculation of the inviscid terms. Additionally, the Jacobian calculation was performed using the van Leer flux function [4]. The C607 propulsion model simulations utilized the stencil-based van Leer flux limiter augmented with a heuristic pressure limiter. Flux limiters were not used in any of the simulations performed for the BLI inlet configuration. Solutions were computed using the Spalart-Allmaras turbulence model [5] with negative provisions (SA-neg), the rotational correction (RC) [6], and Quadratic Constitutive Relation (QCR) 2000 [7], which is designated as SA-neg-RC-QCR in the following discussions. Finally, all simulations for this paper were performed in steady-state mode using local time stepping. Other details regarding FUN3D can

be found in the manual [8], as well as in the extensive bibliography that is accessible at the FUN3D website [9].

2.2 Proportional-Integral-Derivative (PID) Controller

The PID controller provides a method to iteratively update the back pressure at an outflow boundary to achieve a target flow condition. Traditionally, this update process has been performed using trial and error, where the user will set an initial guess for the back pressure, run the simulation, evaluate the flow condition, and repeat until the target condition is met. This process can be tedious and time consuming. The PID-controller method automates this process and increases efficiency by performing the updates without stopping the code. A comparison of the two update methods is provided in Figure 1. Additionally, the update calculation employed by the PID controller is provided in Equation 1, where k_p, k_i, and k_d are user-defined proportional, integral, and derivative weighting terms, respectively, and e_j is the difference between the actual flow condition and the target at the current iteration.

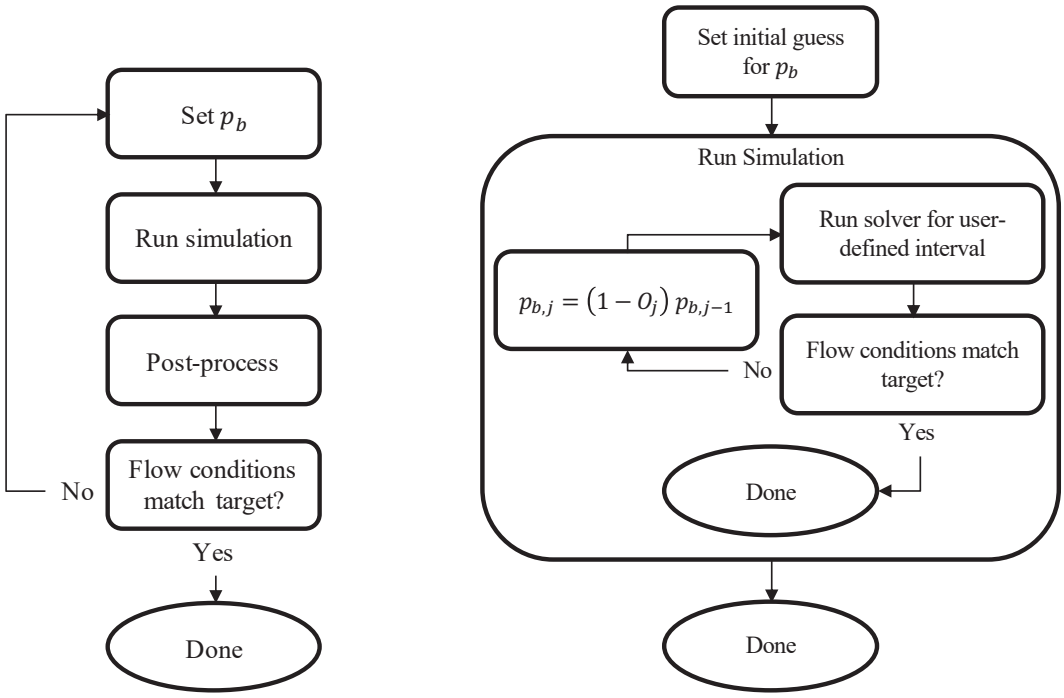

(a) Trial and error.

(b) PID controller.

Figure 1. Methods for achieving target flow conditions.

$$O_j = k_p e_j + k_i \sum_{n=0}^{j} e_n + k_d (e_j - e_{j-1}) \tag{1}$$

3 Boundary Layer Ingestion (BLI) Inlet

The first installed inlet configuration considered for this work was a BLI inlet mounted to a wall, which is shown in Figure 2. This inlet was tested in the 0.3-Meter Transonic Cryogenic Tunnel (0.3M TCT) at the NASA Langley Research Center [10]. The BLI inlet is evaluated at a high-speed, subsonic Mach number to assess the sensitivies of the inlet predictions to simulation strategy, recommend best practices for this type of configuration, and to provide a starting point for the next step, which consists of evaluating an installed inlet at transonic and supersonic speeds.

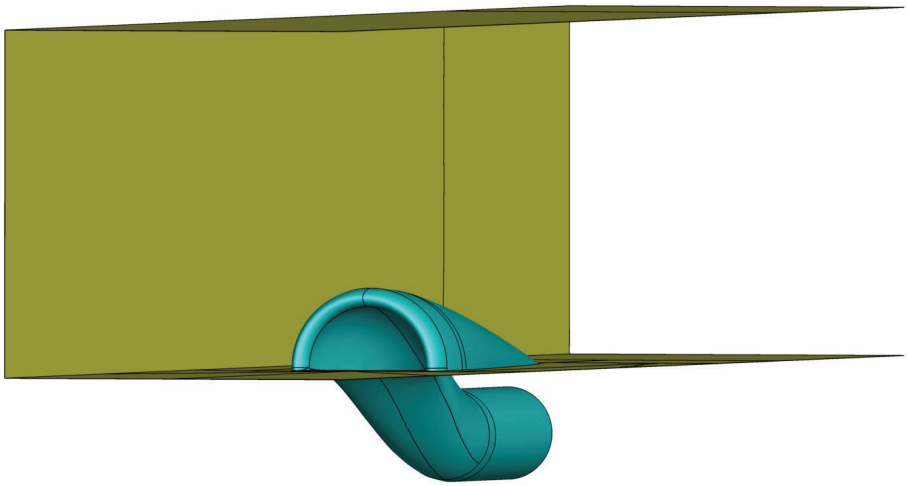

Figure 2. Downstream view of inlet geometry from upstream vantage point.

3.1 Problem Description

The computational model for the BLI inlet included the inlet, as well as a simplified definition of the 0.3M TCT test section. The Aerodynamic Interface Plane (AIP) diameter for this geometry was 1.25 inches and was located at x = 7.534 inches. This problem consists of three flow-through boundaries, as illustrated in Figure 3; an inflow boundary at the test section entrance, an outflow boundary at the test section exit, and an outflow boundary at the inlet outflow, which is located six AIP diameters downstream of the AIP. The tunnel inflow boundary utilized a subsonic inflow BC, which requires definitions of both the total pressure and temperature. The two outflow boundaries were defined using subsonic outflow BCs. This BC type requires a user-defined value for the back pressure. However, since this value is unknown, the PID-controller discussed in Section 2.2 was used to set the back pressure at the two outflow boundaries based on user-defined targets. This is discussed further in the following subsection.

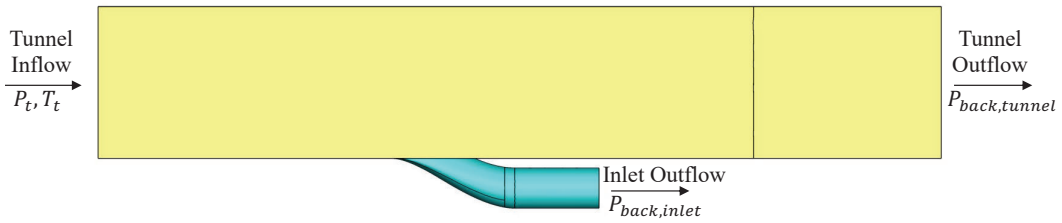

Figure 3. Boundary conditions illustration.

3.1.1 Outflow Boundary Modeling

The PID-controller, Equation 1, was applied to the two outflow boundaries illustrated in Figure 3 to simultaneously match target flow conditions in both the test section and inlet. For the test section, the flow target was an inflow Mach number of 0.58, as defined in Equation 2. The inlet boundary condition employed a user-defined target of 8.82 $\mathrm{lb_m/s}$ for the integrated mass flow rate at the outflow boundary, Equation 3. Note that the test section Mach number and inlet mass flow rate targets were chosen to be representative of the test conditions.

$$e_{tunnel,j} = 0.58 - M_{tunnel,j} \tag{2}$$

$$e_{inlet,j} = 8.82 lb_m/s - \dot{m}_j \tag{3}$$

3.1.2 Outflow Boundary Location

The results of the isolated inlet studies showed that the solution at the AIP was sensitive to the distance between the AIP and the outflow boundary. Given the differences in the problems, the study was repeated here. This study consisted of performing simulations with the outflow boundary located at distances of 0, 2, 4, 6, 8, and 10 AIP diameters downstream of the AIP. An illustration of the considered locations of the outflow boundary is provided in Figure 4.

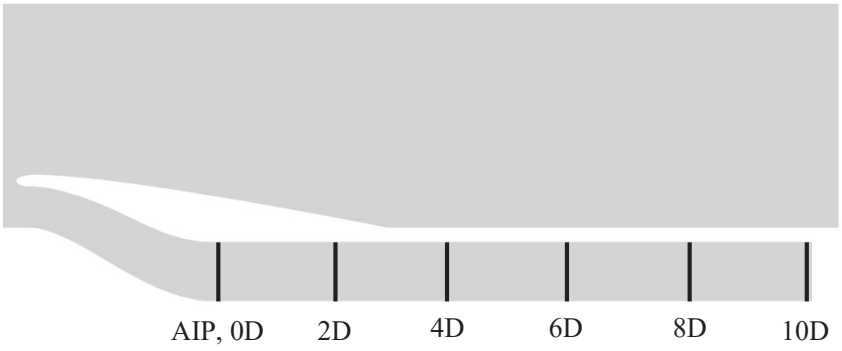

Figure 4. Outflow locations considered in terms of AIP diameters downstream of the AIP.

3.2 ARP1420 Distortion Calculation

The distortion metric, $DPCP_{avg}$, employed for the BLI inlet studies was based on the ARP1420 distortion calculation [11]. This method is illustrated in Figure 5, which provides illustrations of an ARP1420 rake in Figure 5a and the total pressure distortion for a single ring in Figure 5b. The distortion is calculated for each ring using Equation 4, where $P_{t,avg_{low}}$ is defined by Equation 5. The final distortion value is obtained by taking the average over the five equal area rings as shown in Equation 6.

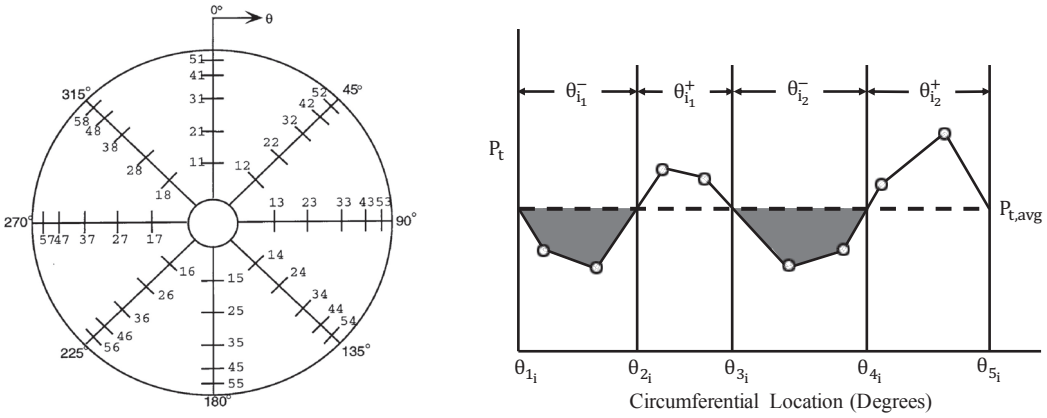

(a) ARP1420 rake.

(b) Total pressure distortion for a single ring.

Figure 5. ARP 1420 distortion illustration.

$$DPCP_i = \frac{P_{t,avg,i} - P_{t,avg_{low},i}}{P_{t,avg,i}} \tag{4}$$

$$P_{t,avg_{low},i} = \frac{1}{\theta_{\bar{i}}} \sum_{k=1}^{Q} \int_{\theta_{i\bar{k}}} P_t(\theta)_i \; d\theta \tag{5}$$

$$DPCP_{avg} = \frac{1}{5} \sum_{i=1}^{5} DPCP_i \tag{6}$$

3.3 Discussion

A description of the computational grids is provided in Section 3.3.1 followed by a brief overview of the typical iterative convergence behavior observed for this problem in Section 3.3.2. The results and discussion for the grid refinement, outflow boundary location, and turbulence model studies performed are provided in Sections 3.3.3, 3.3.4, and 3.3.5. Finally, a brief summary of the BLI inlet studies is provided in Section 3.4.

3.3.1 Computational Grids

Mixed-element, viscous grids were generated for the described geometry using the Heldenmesh™ v3.08 grid generation software [12]. Heldenmesh™ is an unstructured grid generator developed by the Helden Aerospace Corporation that utilizes multi-threading for the rapid generation of both tetrahedral and mixed-element grids. Prior to generating the grids in Heldenmesh™, GridTool [13], a geometry tool contained in the TetrUSS software package developed at the NASA Langley Research Center, was used to create a water-tight geometry with user-defined patch names. Once the geometry definition is provided by GridTool, Heldenmesh™ allows the user to specify the desired resolution of the surface grid through a series of inputs for each of the unique patch names defined in the GridTool model. This process is fairly automated depending on the complexity of the geometry and user preferences.

The baseline grid for this geometry is illustrated in Figure 6. The initial wall spacing for the baseline grid was determined based on a desired y^+ of 1 for a flow condition corresponding to Mach and unit Reynolds numbers of 0.58 and 68×10^6/ft, which were chosen to be representative of the conditions considered in the wind tunnel test. The resulting grid consisted of 2.27×10^6 nodes.

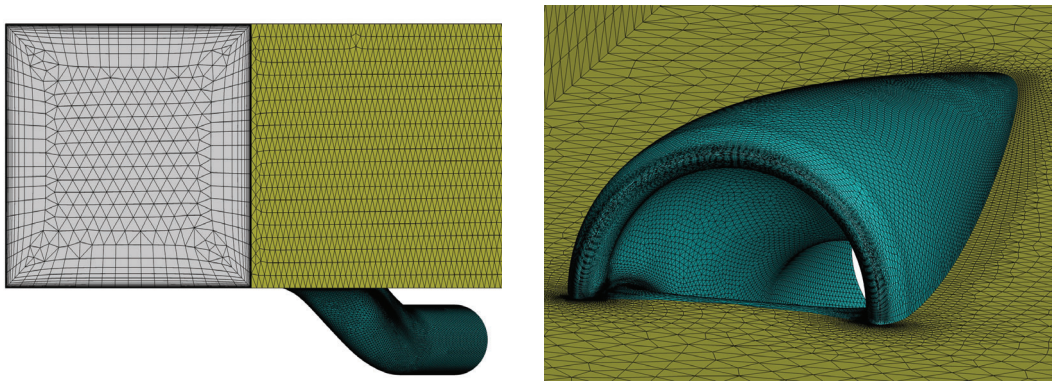

(a) Perspective view.

(b) Zoomed-in view of BLI inlet.

Figure 6. Illustration of baseline grid for BLI inlet configuration.

To enable an assessment of the impact of grid refinement on the BLI inlet predictions, a series of grids were generated using the baseline as the starting point. Heldenmesh offers a user-defined refinement factor to scale the inviscid portion of the grid. In an effort to obtain a series of uniformly scaled grids, the refinement factor (h) was also manually applied to scale the y^+ and growth rate parameters (r_1, r_2) for the cells in the boundary layer. For this study, the refinement factor was determined through trial and error to provide approximately a factor of 2 difference in the number of nodes between two successive grid refinements. The resulting grid sizes are provided in Table 1 and illustrated in Figure 7. Note that the baseline grid was designated as the coarse grid in Table 1.

Table 1. Grid sizes for BLI inlet geometry.

	h	y^+	r_1	r_2	Nodes (Millions)
Tiny	1.225	1.225	0.238	0.015	1.122
Coarse	1.000	1.000	0.125	0.015	2.271
Medium	0.837	0.837	0.058	0.015	4.587
Fine	0.715	0.715	0.022	0.015	9.265
Extra Fine	0.625	0.625	0.005	0.015	18.44

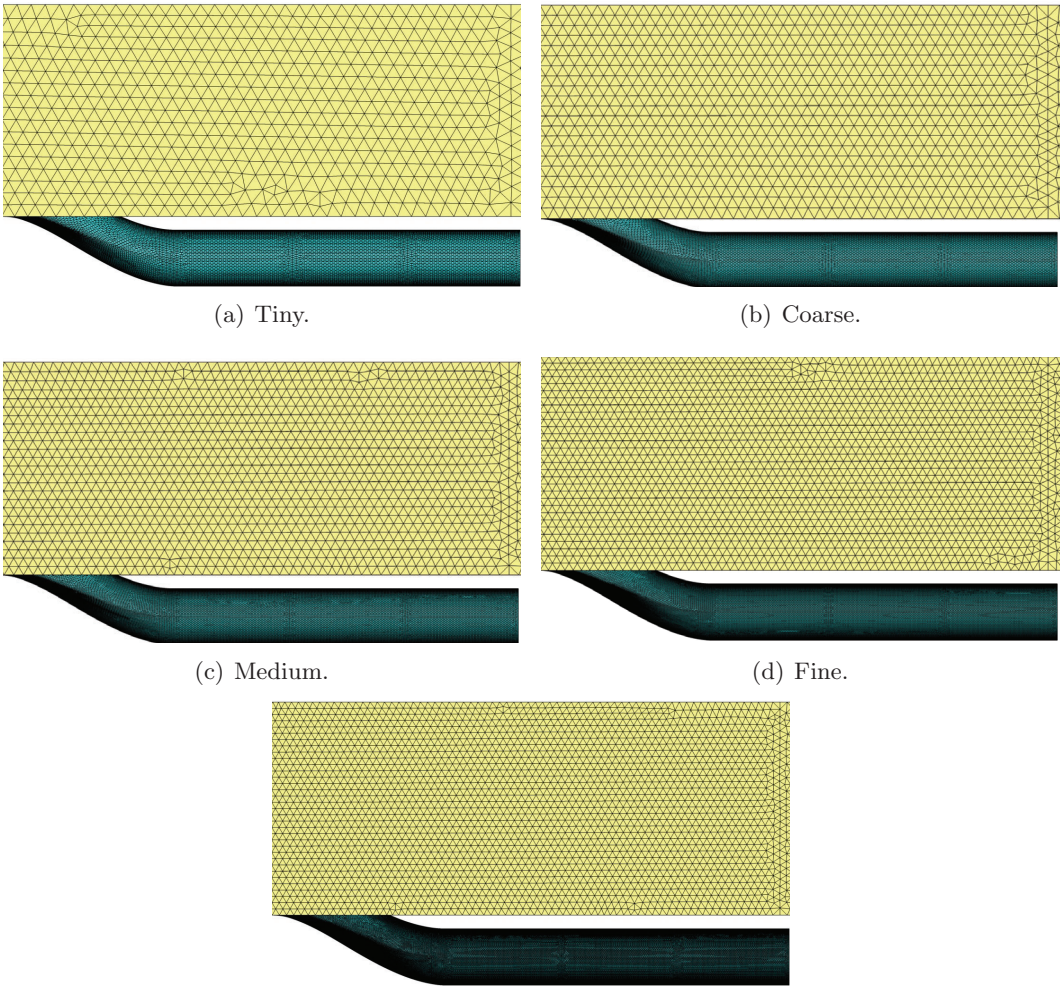

(a) Tiny.

(b) Coarse.

(c) Medium.

(d) Fine.

(e) Extra Fine.

Figure 7. Grid refinement series.

3.3.2 Convergence History

Iterative convergence was monitored by simultaneously tracking the residual and controller histories. The primary goal was to converge on the flow condition targets

using the PID-controller. Once the PID-controller converged on the target flow conditions, the secondary goal was then to achieve an adequate reduction in the residuals. The residual history for the baseline grid is provided in Figure 8 and the controller history is provided in Figure 9.

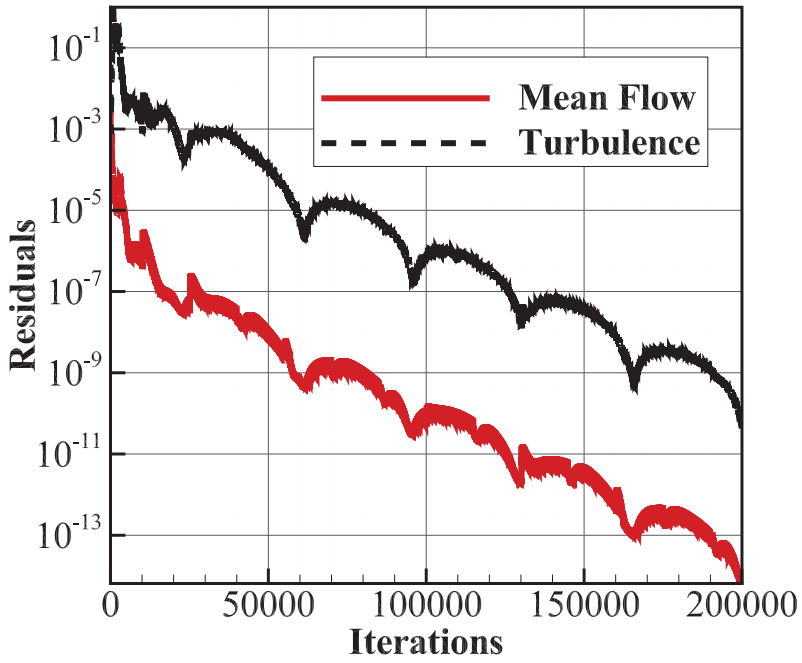

Figure 8. Residual history for baseline grid, outflow boundary located six AIP diameters downstream of the AIP, and mass flow rate target.

The convergence history provided in Figure 8 illustrates favorable convergence behavior with the mean flow residual approaching 10^{-14} and the turbulence residual approaching 10^{-11}. Both residuals appear to still be decreasing even after 200,000 iterations. Figures 9a and 9c illustrate the histories of the PID-controller terms and output, O_j, and Figures 9b and 9d illustrate the histories of the resulting back pressure updates and flow quantities of interest for the tunnel and inlet controllers, respectively. The results show that even though the residuals are still decreasing after 200,000 iterations, both inlet and tunnel controllers are converged after approximately 80,000 iterations, with the inlet controller requiring the most iterations to converge. Note that the iterative convergence illustrated here is representative of the typical behavior observed for the BLI inlet simulations.

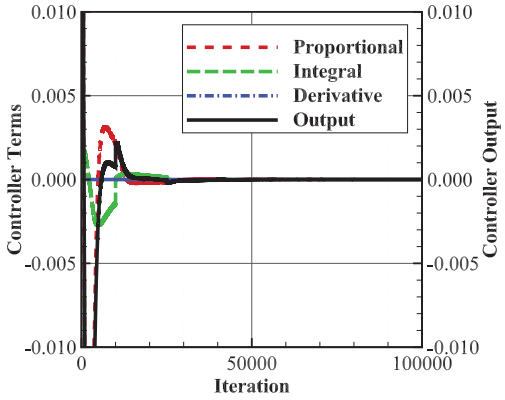

(a) Tunnel - controller history.

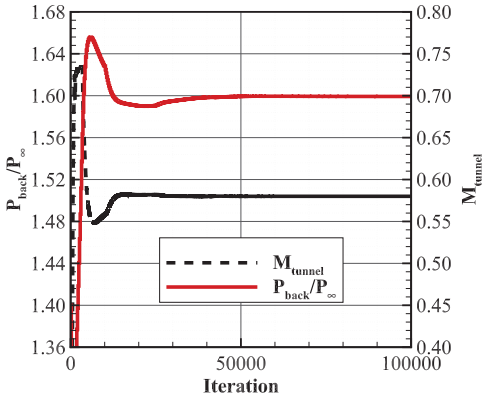

(b) Tunnel - back pressure and mass flow rate histories.

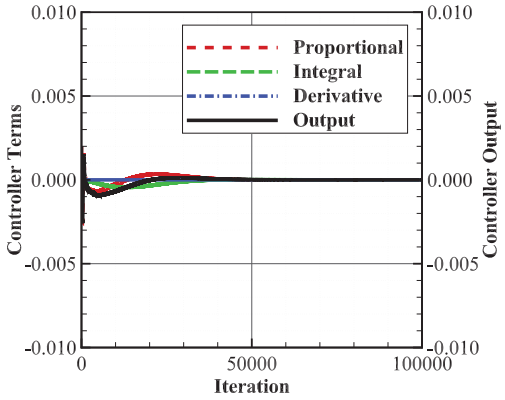

(c) Inlet - controller history.

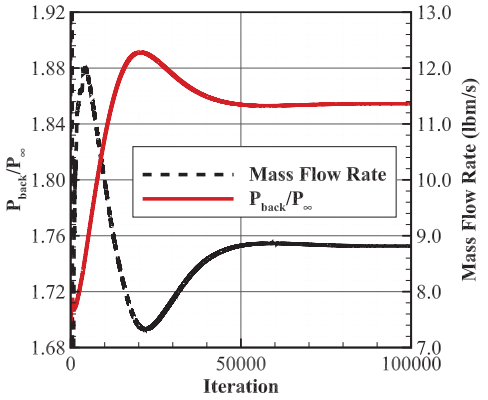

(d) Inlet - back pressure and mass flow rate histories.

Figure 9. Controller histories for baseline grid, outflow boundary located two AIP diameters downstream of AIP, and mass flow rate target.

3.3.3 Grid Refinement Study

The results provided in Figures 10 and 11 illustrate the total pressure and Mach number contours at the AIP for the five levels of grid refinement. The results show slight differences in the shape of the low-pressure region at the AIP, with the region appearing to become increasingly narrow with increasing grid size. However, the qualitative comparisons shown here illustrate only minor differences with no definitive indication of the impact of grid refinement on the flow quantities of interest. The results provided in Figures 12 and 13 illustrate the total pressure and Mach number contours at $y = 0$ inches for the five levels of grid refinement. Both the total pressure and Mach number contours show good qualitative agreement between the various grid sizes.

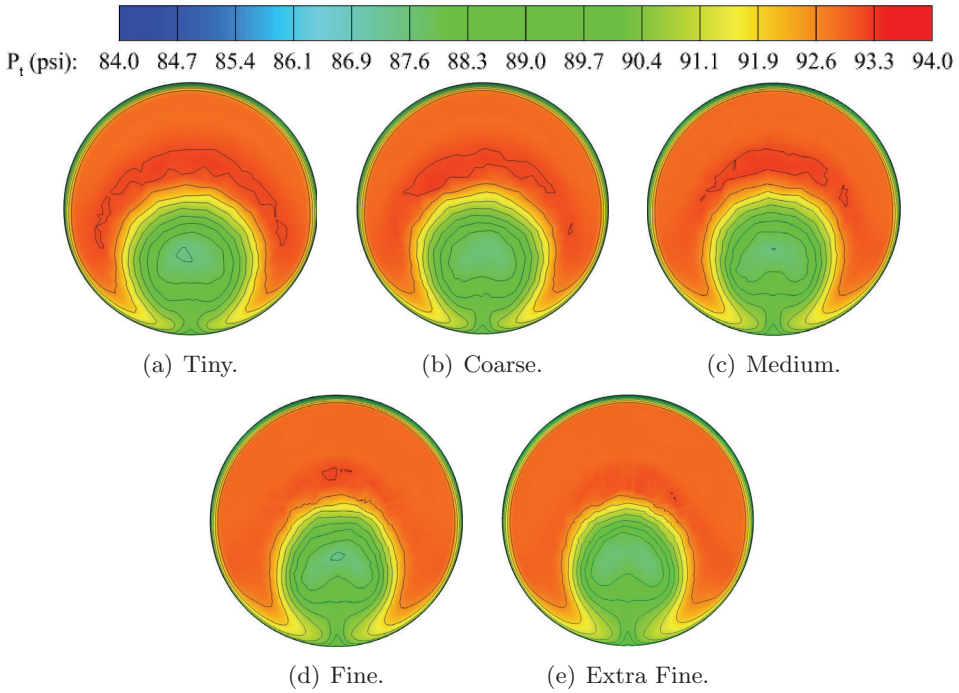

(a) Tiny. (b) Coarse. (c) Medium.

(d) Fine. (e) Extra Fine.

Figure 10. Total pressure contours at the AIP as a function of grid refinement.

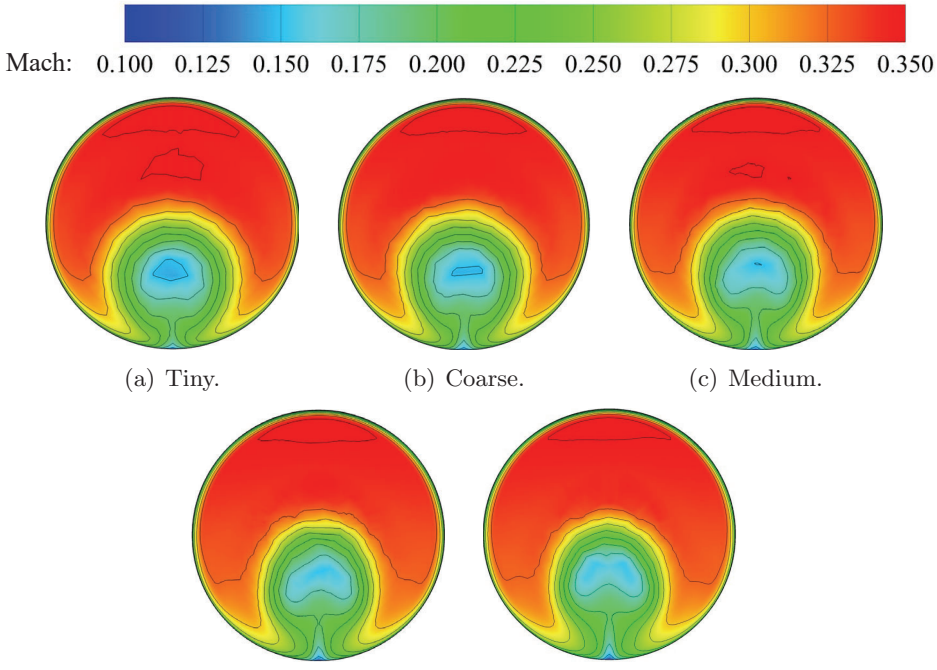

(a) Tiny. (b) Coarse. (c) Medium.

(d) Fine. (e) Extra Fine.

Figure 11. Mach number contours at the AIP as a function of grid refinement.

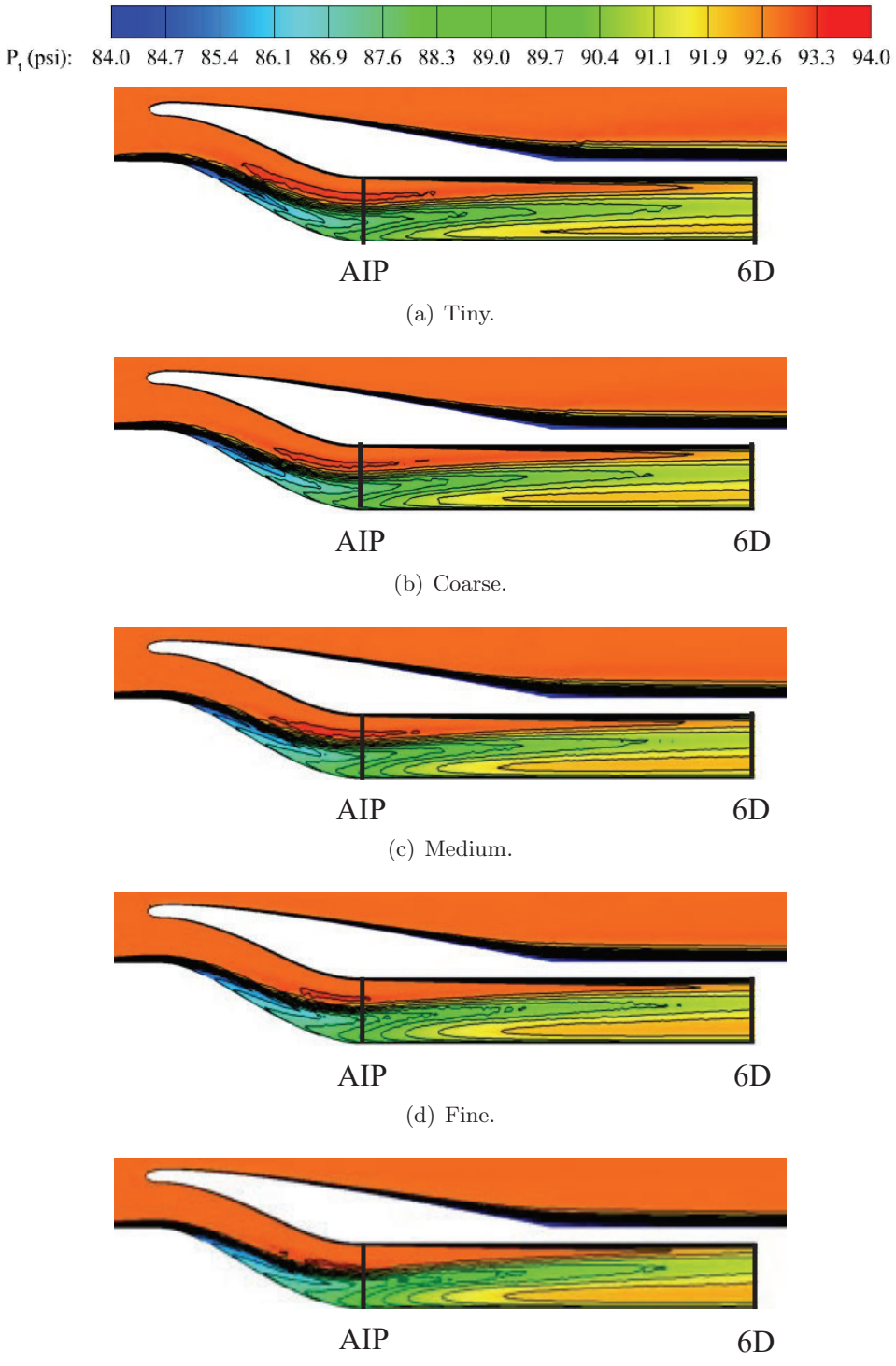

(a) Tiny.

(b) Coarse.

(c) Medium.

(d) Fine.

(e) Extra Fine.

Figure 12. Total pressure contours at the y = 0 plane as a function of grid refinement.

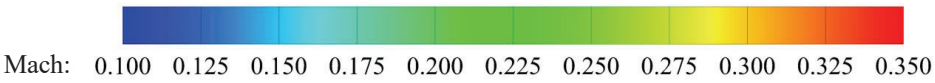

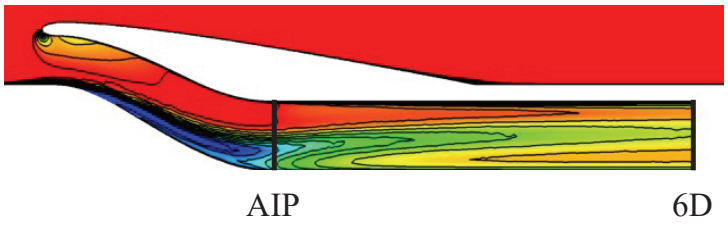

(a) Tiny.

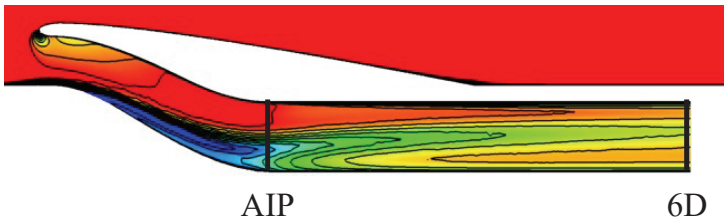

(b) Coarse.

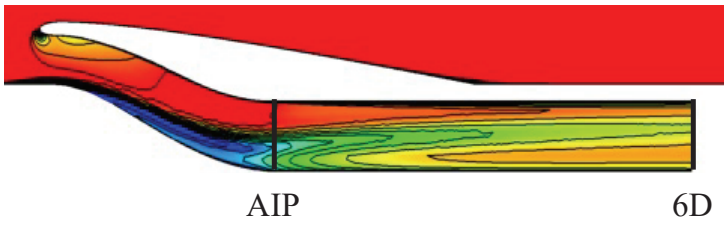

(c) Medium.

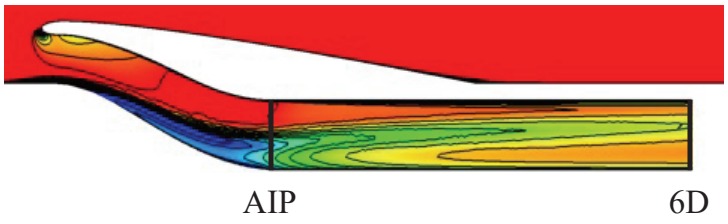

(d) Fine.

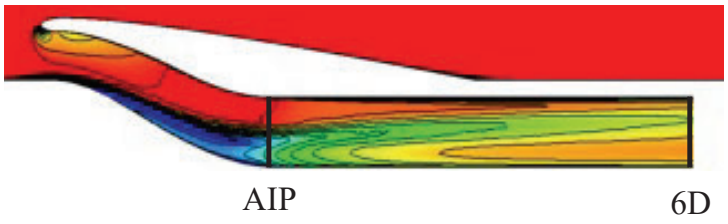

(e) Extra Fine.

Figure 13. Mach contours at the y = 0 plane as a function of grid refinement.

The quantitative results of the grid refinement study are provided in Figure 14 in the form of the flow quantities of interest at the AIP plotted against grid size. The grid size is presented as $N^{-2/3}$, where N is the number of nodes. Similar to the qualitative comparisons, the results show that grid refinement has only a minor impact on the flow at the AIP for the given problem. One of the reasons for this is the application of the mass flow rate controller. Because of the controller, the mass flow rate is nearly identical between the grid levels. The result is that the flow quantities are very similar between the grid levels. This is in contrast to the results that would have been obtained if a fixed back pressure was applied at the inlet outflow boundary, which would have resulted in variation of the mass flow rate with grid refinement level. Comparing the distortion ($DPCP_{avg}$), Mach number at the AIP ($M_{AIP,avg}$), and mass flow rate results, the mass flow rate appears to have the strongest impact on the predicted distortion and Mach number at the AIP. The finest grid has a slightly lower mass flow rate relative to the other grid refinements, which shows up as a slight increase in distortion along with a slight decrease in Mach number at the AIP. Note that this difference in mass flow rate for the finest grid level was due to convergence. The application of the PID controller to the finest grid proved difficult for converging the solution relative to the other cases. This likely could have been fixed with modifications to the controller weighting terms and/or controller update frequencies of the two boundaries. However, the difference was only minor and easily explained. Based on the results provided in this section, the baseline (coarse) grid was chosen for the remaining studies.

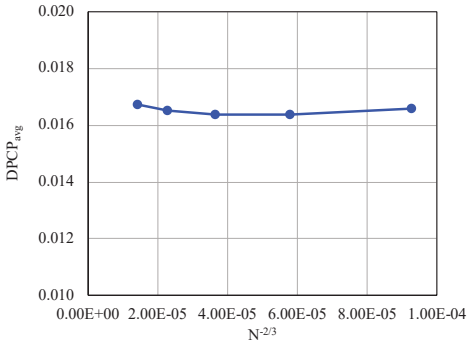

(a) Distortion at AIP, $DPCP_{avg}$.

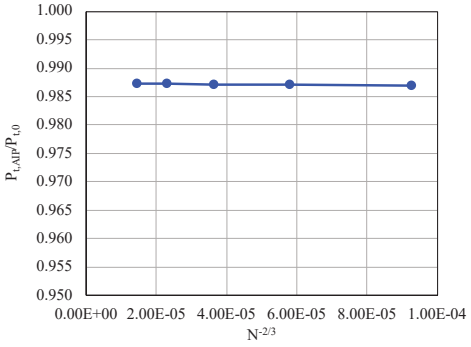

(b) Pressure recovery at AIP, $P_{t,AIP}/P_{t,0}$.

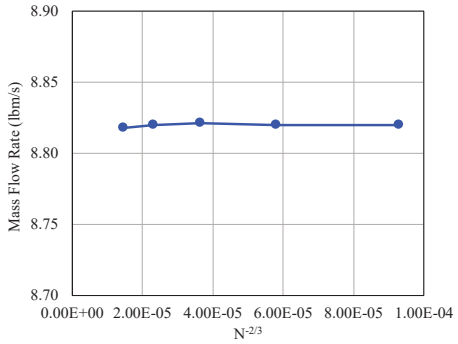

(c) Mass flow rate at AIP.

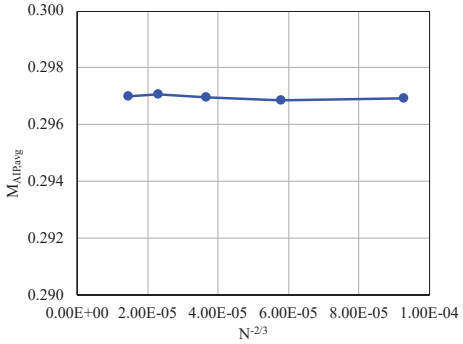

(d) Mach number at AIP, $M_{AIP,avg}$.

Figure 14. Integrated quantities at the AIP as a function of grid size.

3.3.4 Outflow Boundary Location Studies

The results of the outflow boundary location study are provided in Figures 15 through 19. For this study, the PID controller was applied to achieve the target mass flow rate at the outflow boundary for locations corresponding to 0, 2, 4, 6, 8, and 10 AIP diameters downstream of the AIP. The total pressure and Mach number contours at the AIP for each of the described outflow boundary locations are provided in Figures 15 and 16. Comparing the total pressure contours for the six outflow boundary locations, the results look qualitatively similar for all locations except for the case with the outflow boundary located at the AIP ($0D$). For the $0D$ case, the low pressure region is noticeably smaller than the other five locations. The same observation can be made from the Mach number contours. Also, the Mach number contour plots show that the $0D$ case exhibits a noticeably thicker boundary layer around the top of the AIP relative to the other locations. The contour plots at the $y = 0$ plane provided in Figures 17 and 18 illustrate the same trends discussed for the AIP. The results compare favorably for all outflow boundary locations with the largest qualitative differences observed for the $0D$ case.

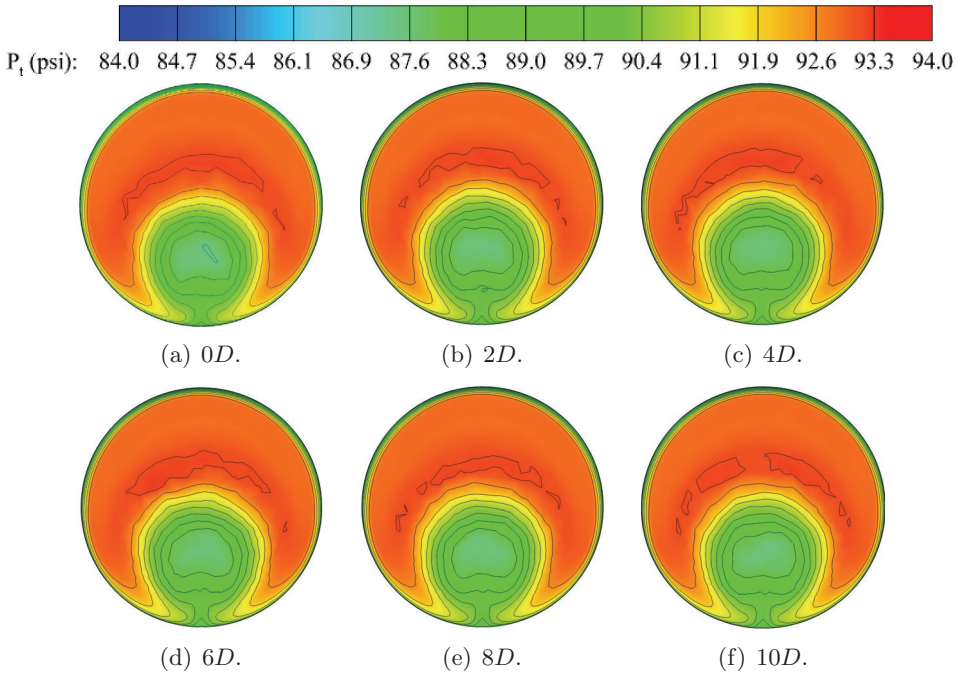

(a) $0D$. (b) $2D$. (c) $4D$.

(d) $6D$. (e) $8D$. (f) $10D$.

Figure 15. Total pressure contours at the AIP as a function of outflow boundary location; mass flow rate controller.

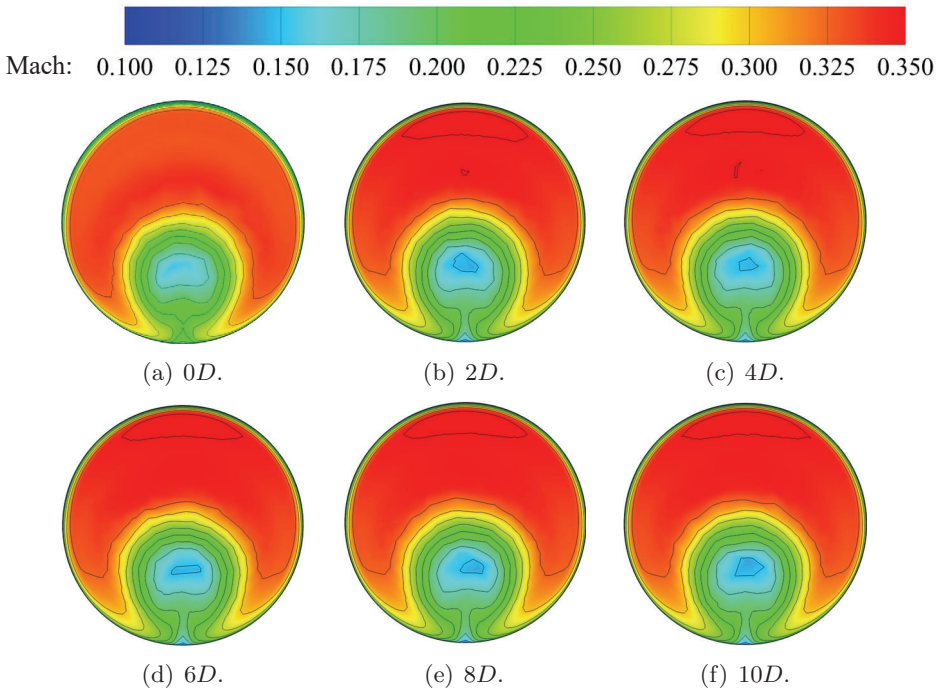

(a) $0D$. (b) $2D$. (c) $4D$.

(d) $6D$. (e) $8D$. (f) $10D$.

Figure 16. Mach contours at the AIP as a function of outflow boundary location; mass flow rate controller.

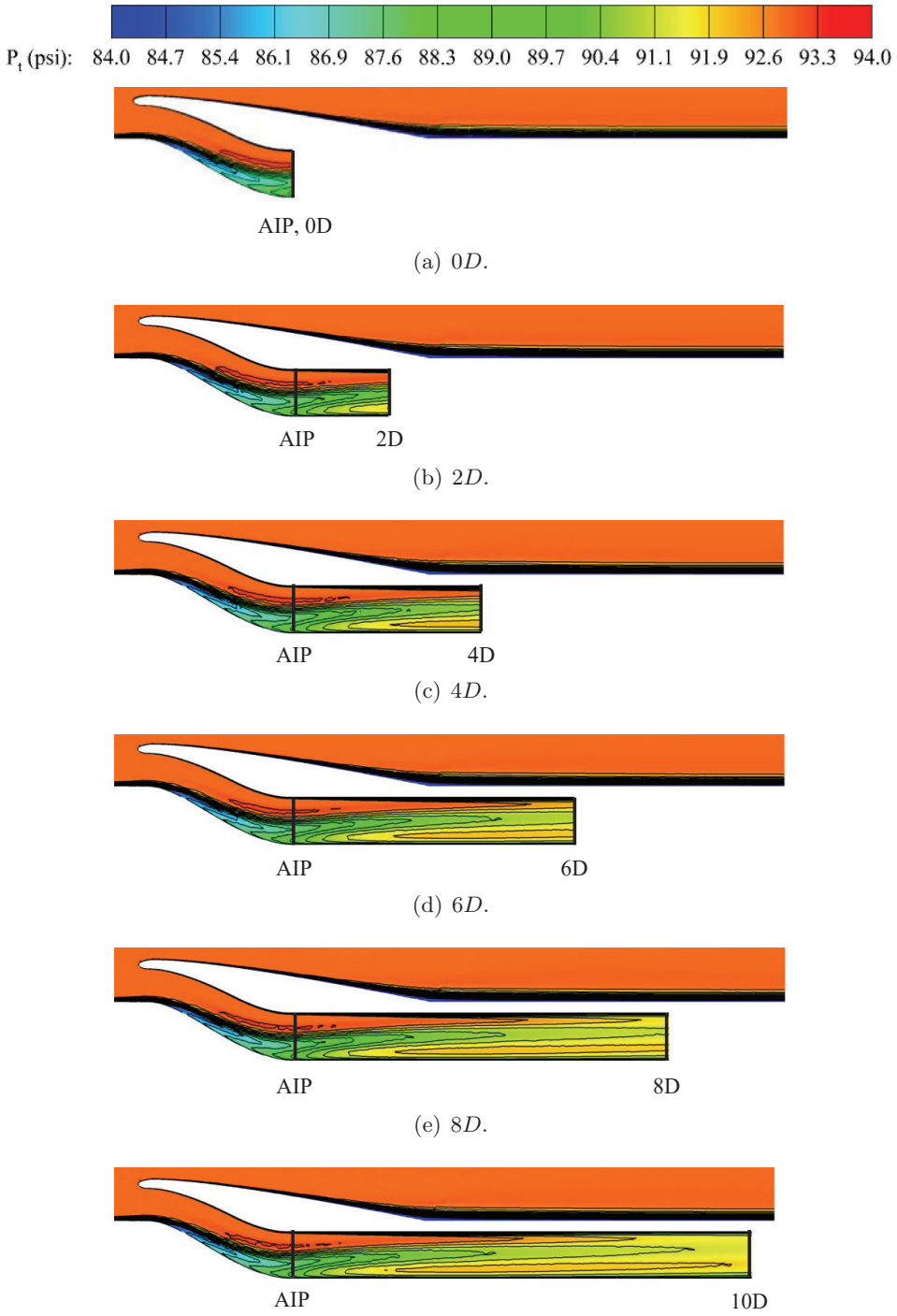

(a) $0D$.

(b) $2D$.

(c) $4D$.

(d) $6D$.

(e) $8D$.

(f) $10D$.

Figure 17. Total pressure contours at the y = 0 plane as a function of outflow boundary location; mass flow rate controller.

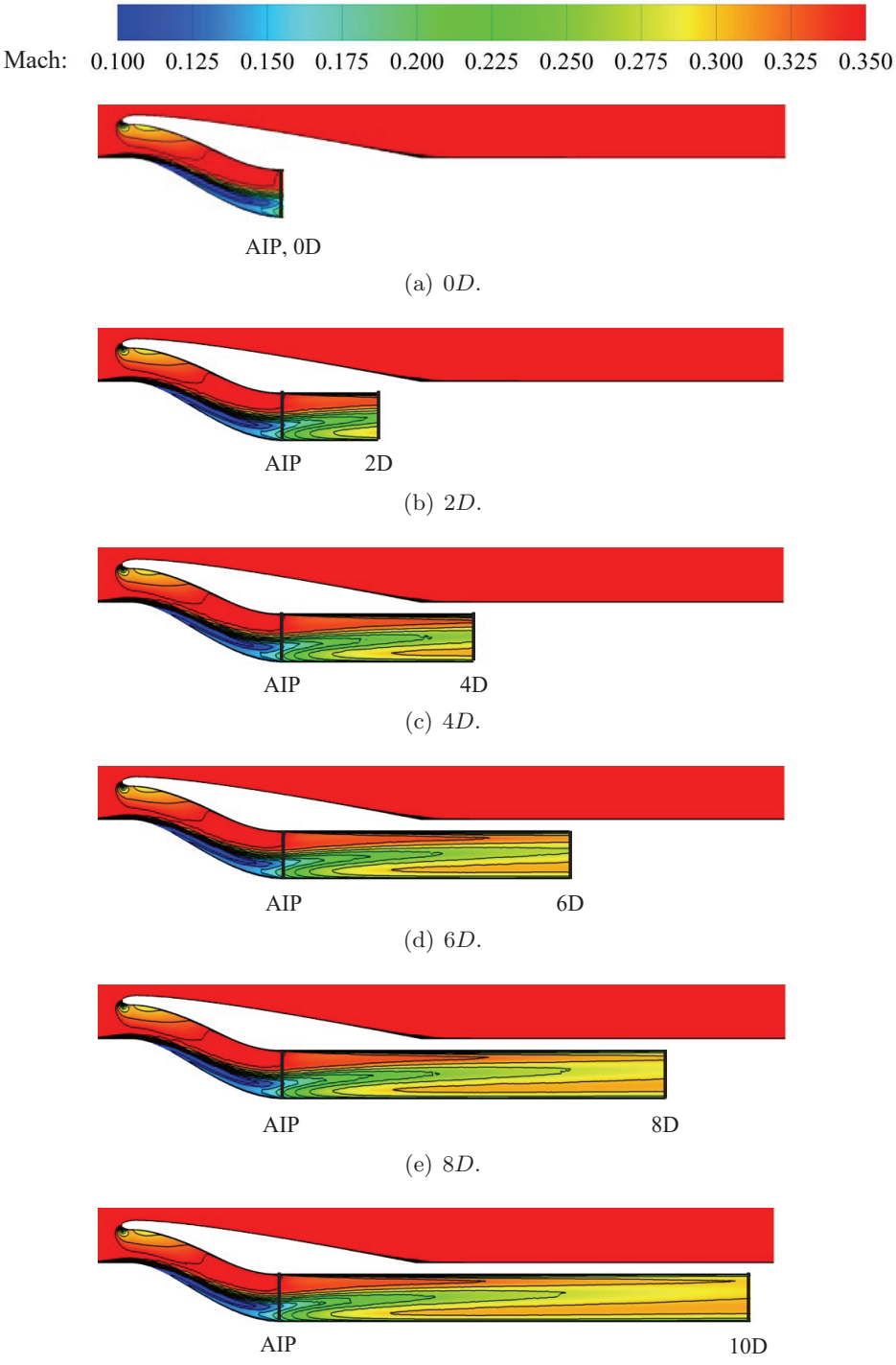

(a) $0D$.

(b) $2D$.

(c) $4D$.

(d) $6D$.

(e) $8D$.

(f) $10D$.

Figure 18. Total pressure contours at the y = 0 plane as a function of outflow boundary location; mass flow rate controller.

Finally, Figure 19 illustrates the resulting distortion, pressure recovery, mass flow rate, and Mach number at the AIP as a function of outflow boundary location. The results show that, while there are variations in the quantities of interest with outflow boundary location, the differences are relatively small. From the provided results, there does not appear to be a trend that would indicate a benefit to placing the outflow boundary further than two AIP diameters downstream of the AIP. However, the results show some differences for the $0D$ case. The $0D$ case shows a higher average Mach number at the AIP for a given mass flow rate relative to the other outflow boundary locations. The results provided in Figure 16a show a lower Mach number outside of the low-momentum region and a higher Mach number in the low-momentum region for the $0D$ case. Considering this observation and the higher average Mach number at the AIP, the results indicate that placing the outflow boundary at the AIP impacts the low-momentum region of the flow at the AIP. Also, even though the differences are relatively small for this problem, this result indicates that the best practice would be to avoid placing the outflow boundary directly at the region of interest.

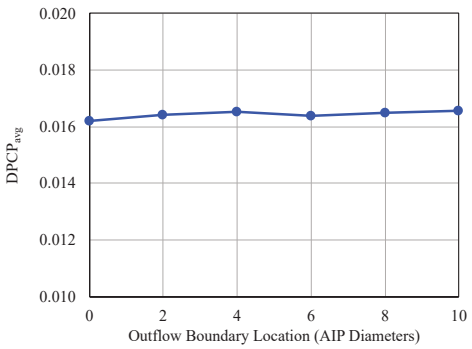

(a) Distortion at AIP, $DPCP_{avg}$.

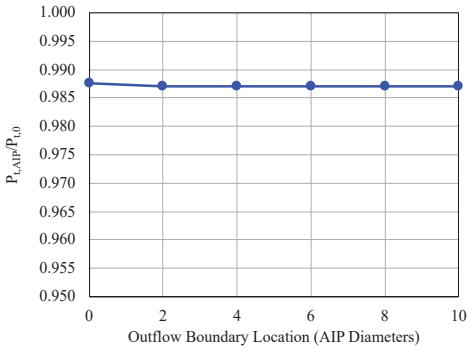

(b) Pressure recovery at AIP, $P_{t,AIP}/P_{t,0}$.

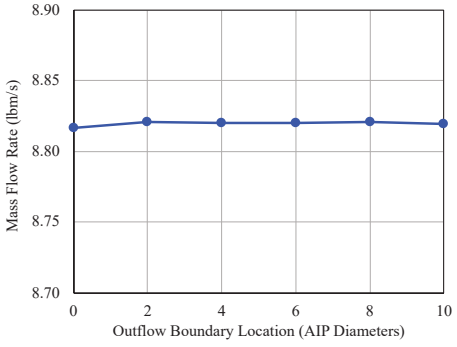

(c) Mass flow rate at AIP.

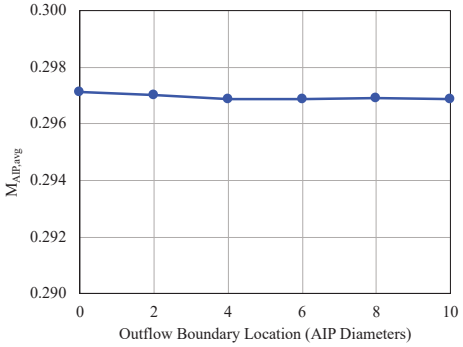

(d) Mach number at AIP, $M_{AIP,avg}$.

Figure 19. Integrated quantities at the AIP as a function of outflow boundary location and controller target.

3.3.5 Turbulence Model Study

The final study performed for the BLI inlet geometry investigated the impact of the turbulence model on the inlet predictions. In addition to the SA-neg-RC-QCR model, the turbulence model study also considered the standard Spalart Allmaras (SA) model [5], the two-equation Menter Shear Stress Transport (SST) model [14], and the SSG/LRR-ω seven-equation, omega-based, full Reynolds Stress Model (RSM) [15]. Additionally, this study was performed using both the coarse and fine grids to provide confidence that the findings hold for higher grid refinements.

The total pressure contours at the AIP are provided in Figures 20 and 21 for the coarse and fine grids, respectively. The coarse grid solutions exhibit qualitative differences in the flow at the AIP for the four turbulence models considered. The SA-neg-RC-QCR model results, Figure 20a, exhibit the lowest total pressure in the low-momentum region relative to the other turbulence models, which is apparent from the size of the inner-most contour line within the low-momentum region of the solution. Another interesting observation is that the SA, Figure 20b, and SST, Figure 20c, solutions appear qualitatively similar in terms of the size and shape of the low-momentum region. Finally, the RSM solution, Figure 20d, exhibits a noticeably different shape for the low-momentum region, which appears shorter and wider than the other three solutions. Comparing the solutions obtained using the coarse and fine grids, the relative differences appear to be consistent.

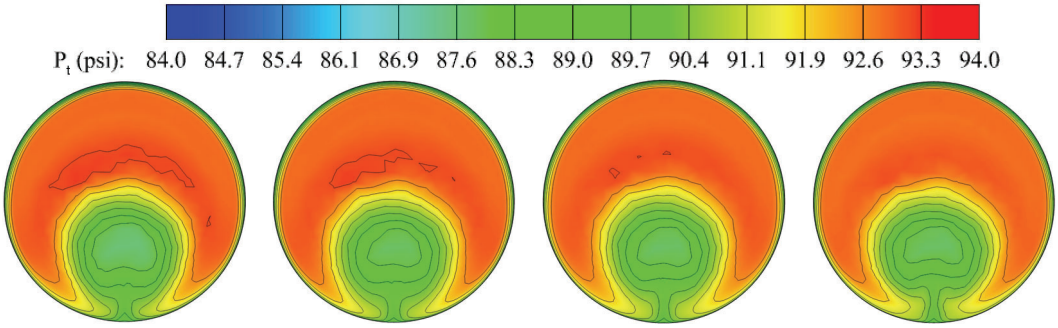

(a) SA-neg-RC-QCR. (b) SA. (c) SST. (d) RSM.

Figure 20. Total pressure contours at the AIP as a function of turbulence model; coarse grid.

Similarly, the Mach number contours at the AIP are provided in Figures 22 and 23 for the coarse and fine grids. The solution produced using the SA-neg-RC-QCR model, Figure 22a, exhibits the lowest Mach number in the low-momentum region relative to the other turbulence models. As also observed from the total pressure contour plots, the SA and SST results agree favorably and the RSM model exhibits a low-momentum region that is shorter and wider than the other three models.

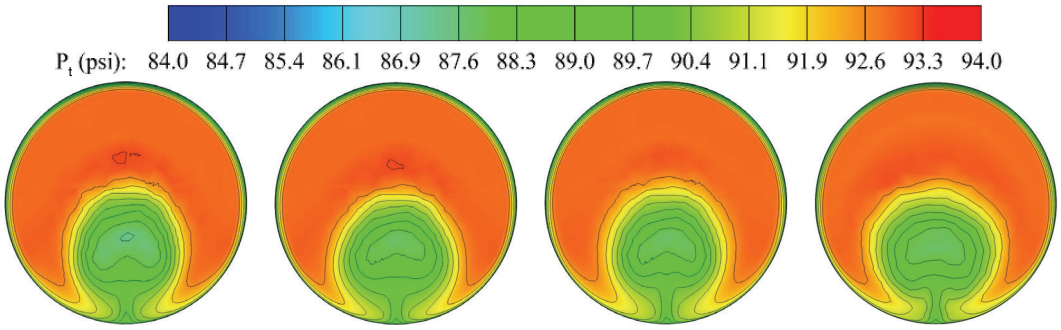

(a) SA-neg-QCR-RC. (b) SA. (c) SST. (d) RSM.

Figure 21. Total pressure contours at the AIP as a function of turbulence model; fine grid.

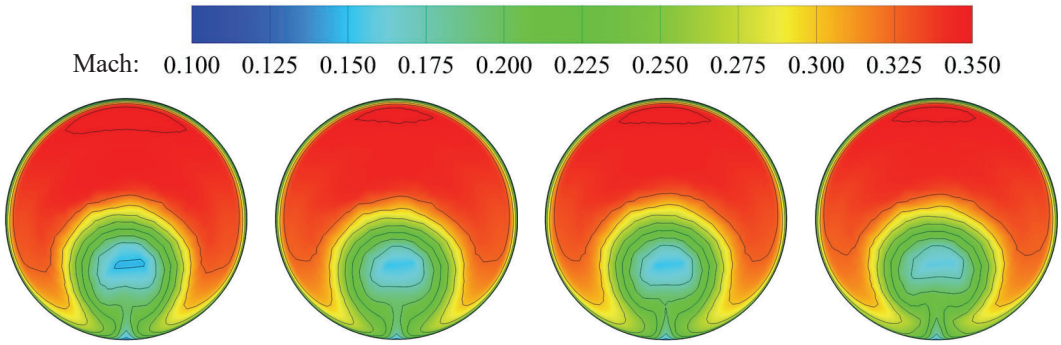

(a) SA-neg-RC-QCR. (b) SA. (c) SST. (d) RSM.

Figure 22. Mach contours at the AIP as a function of turbulence model; coarse grid.

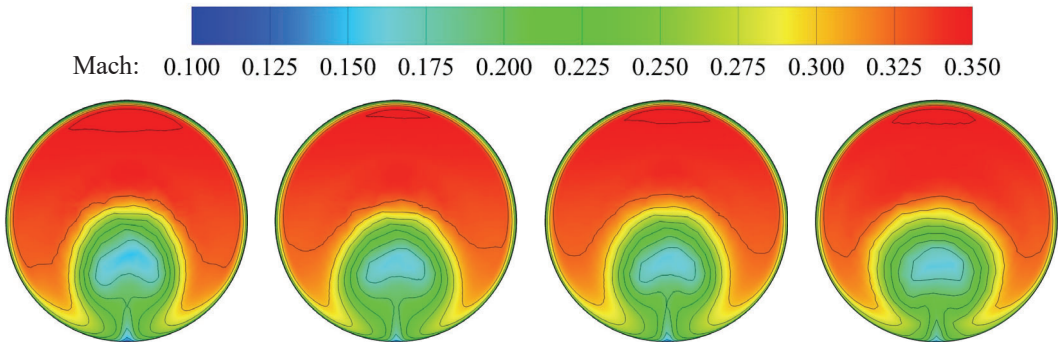

(a) SA-neg-RC-QCR. (b) SA. (c) SST. (d) RSM.

Figure 23. Mach contours at the AIP as a function of turbulence model; fine grid.

The total pressure and Mach contours at the $y = 0$ slice for the coarse and fine grids are provided in Figures 24 through 27. The contour plots at the $y = 0$ slice confirm the findings discussed for the AIP contour plots.

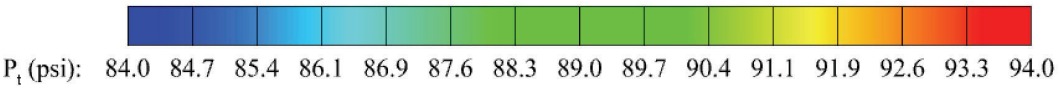

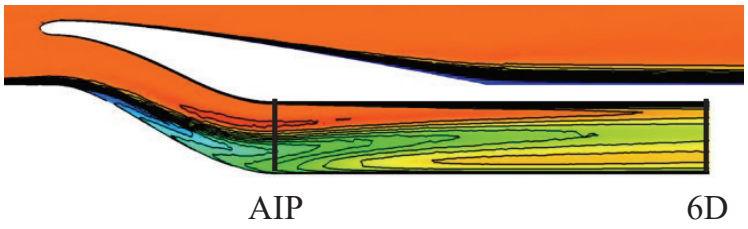

(a) SA-neg-RC-QCR.

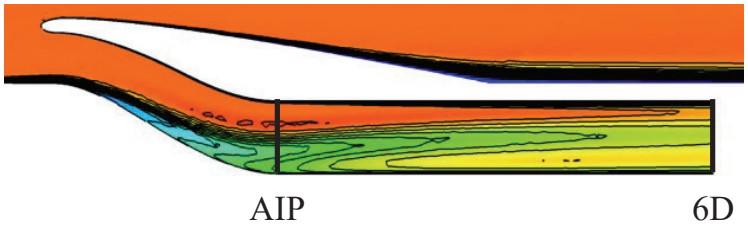

(b) SA.

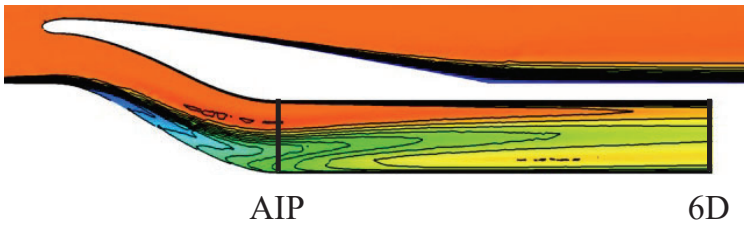

(c) SST.

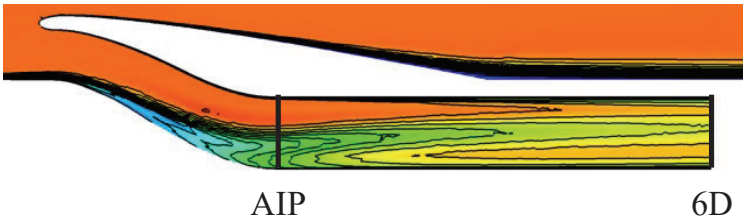

(d) RSM.

Figure 24. Total pressure contours at the y = 0 plane as a function of turbulence model; coarse grid.

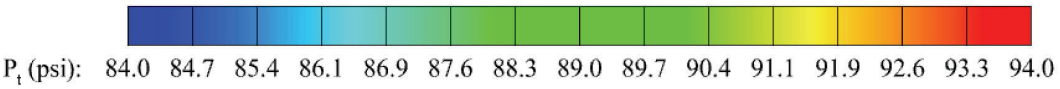

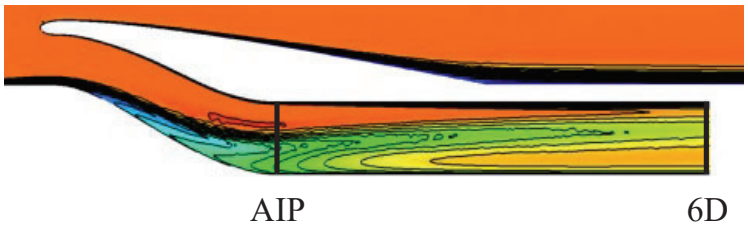

(a) SA-neg-RC-QCR.

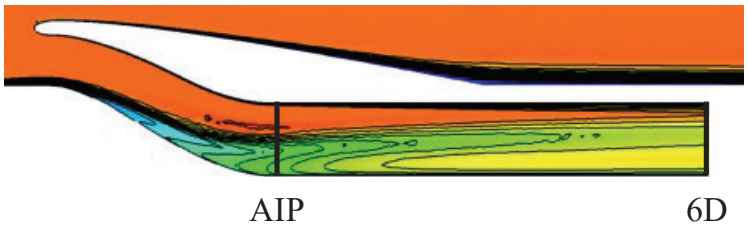

(b) SA.

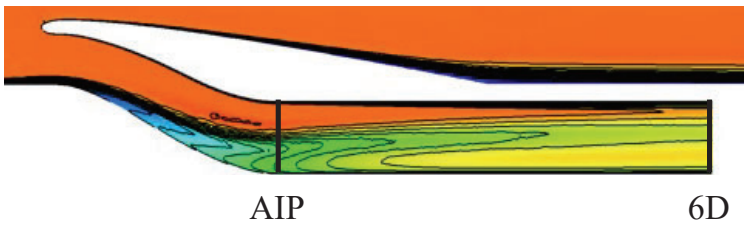

(c) SST.

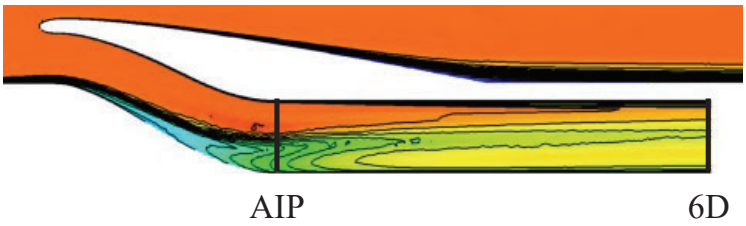

(d) RSM.

Figure 25. Total pressure contours at the y = 0 plane as a function of turbulence model; fine grid.

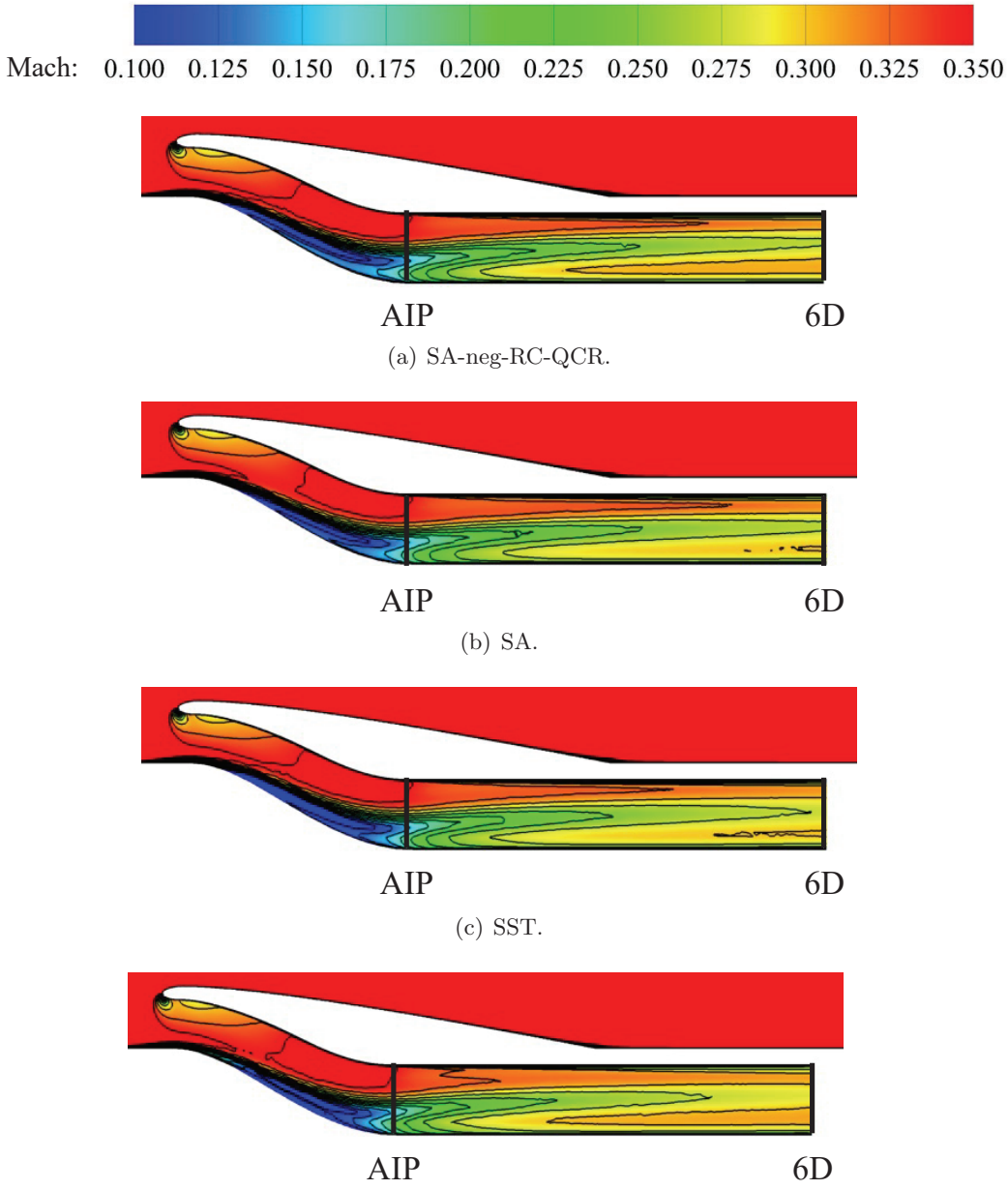

(a) SA-neg-RC-QCR.

(b) SA.

(c) SST.

(d) RSM.

Figure 26. Mach contours at the y = 0 plane as a function of turbulence model; coarse grid.

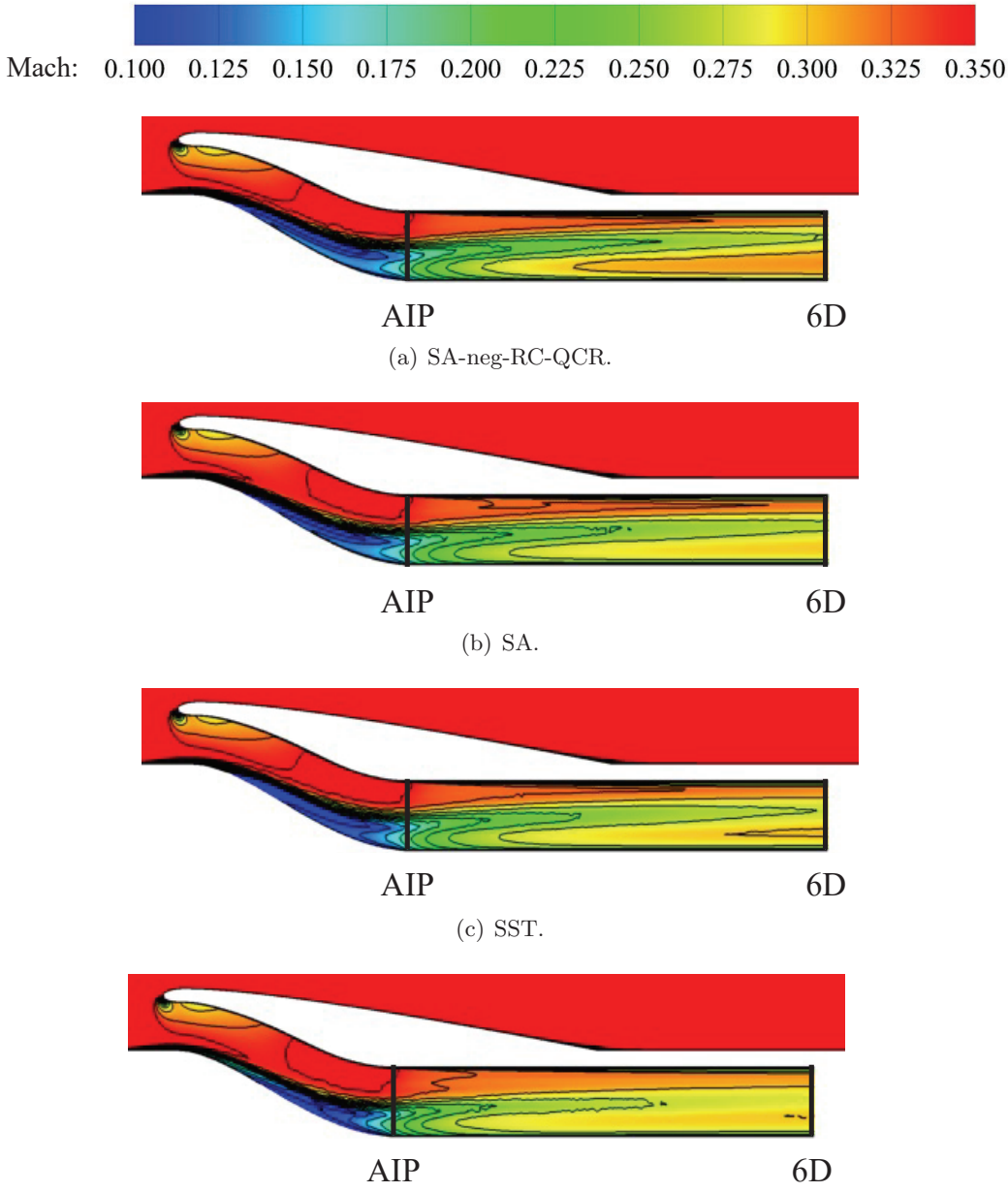

(a) SA-neg-RC-QCR.

(b) SA.

(c) SST.

(d) RSM.

Figure 27. Mach contours at the y = 0 plane as a function of turbulence model; fine grid.

The results provided in Figure 28 illustrate the distortion, pressure recovery, mass flow rate, and average Mach number at the AIP. The results are provided for all five grid refinements for the baseline turbulence model (SA-neg-RC-QCR). Additionally, both coarse and fine grid solutions are provided for the SA, SST, and RSM turbulence models. The results show that the SA-neg-RC-QCR and SA-RC-QCR models generally predict the highest distortion and average Mach number at

the AIP relative to the other four models. For the coarse grid, the SST, SA, and SA-QCR results agree very well, while the RSM model predicts the lowest distortion. On the other hand, the fine grid results show that the SA and RSM models agree very well, with the SST model predicting the lower value of distortion at the AIP. The SA model predicts the highest value of pressure recovery at the AIP. The mass flow rate at the AIP shows favorable agreement between all of the models, which is to be expected given that the mass flow rate was set consistently for all models using the PID controller. However, it is interesting that the RSM predicts slightly lower mass flow rate at the AIP relative to the other models. Note that this difference is small ($<<$ 1%). Finally, the average Mach number at the AIP is shown to be larger for the SA-neg-RC-QCR and SA-RC-QCR models than any of the other four models, which all agree favorably.

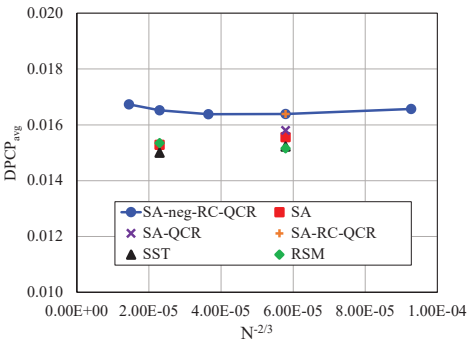

(a) Distortion at AIP, $DPCP_{avg}$.

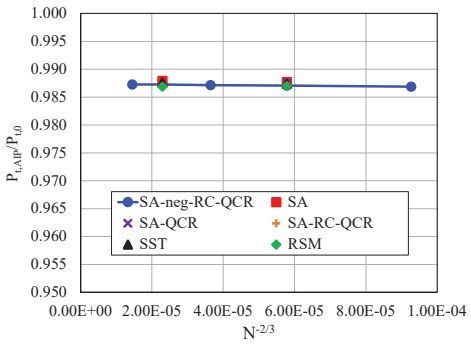

(b) Pressure recovery at AIP, $P_{t,AIP}/P_{t,0}$.

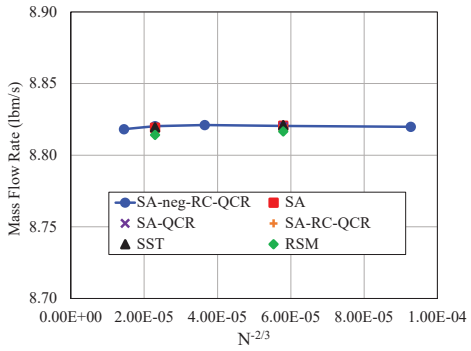

(c) Mass flow rate at AIP.

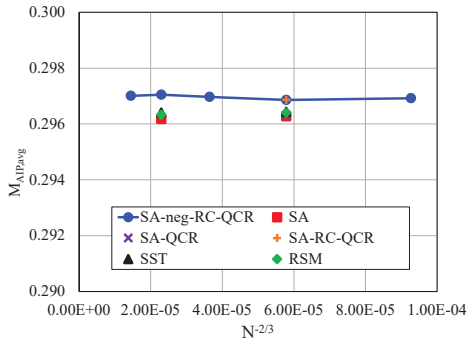

(d) Mach number at AIP, $M_{AIP,avg}$.

Figure 28. Integrated quantities at the AIP as a function of grid refinement and turbulence model.

3.4 Summary

Studies were performed to investigate the impact of grid refinement, outflow boundary location, and turbulence model on the predictions for a wall-mounted BLI inlet. The impact of grid refinement was minimal for the given problem, which used a PID

controller to match the target mass flow rate for all grid refinements. Note that this finding may not hold if the mass flow rate were not matched for all grid refinements. Also, the impact of grid refinement could vary for different configurations. The outflow boundary study showed that the location of the outflow boundary does not have a significant impact on the flow at the AIP for this problem. This is in contrast to the findings from the isolated inlet studies. However, the flow at the AIP was shown to be slightly different when the outflow boundary was placed directly at the AIP. Due to this observation, it is recommended that the outflow boundary be placed downstream of the AIP, with the necessary distance appearing to be problem dependent. For this particular case, a distance of two AIP diameters was found to be sufficient to not significantly modify the flow at the AIP. Finally, the results of the turbulence model study showed differences between the SA-neg-RC-QCR predictions relative to the other turbulence models considered. Interestingly, the SA, SST, and RSM models agreed favorably. However, it is unclear which model would be most suitable for this problem given the lack of comparisons to experimental data. This finding will be further investigated in the study to follow, which includes comparisons to experimental data for a relevant configuration.

4 C607 Propulsion Model

The next configuration considered for the installed inlet studies was the C607 supersonic transport model that was tested in the 8x6 Supersonic Wind Tunnel at the NASA Glenn Research Center in 2017 [1]. Note that the wind tunnel test considered two versions of the model: an aerodynamic model and a propulsion model. This work is focused on the propulsion model, shown in Figure 29. The propulsion model featured an adjustable mass flow plug to allow for sweeps of mass flow rate through a top-mounted inlet. Additionally, experimental data were obtained over a range of Mach numbers, angles of attack, and angles of sideslip. The goals of the present task were to assess the sensitivity of the predicted inlet performance to FUN3D input parameters, such as turbulence model and flux limiter, boundary condition type, and boundary condition location. Additionally, the results of the simulations were compared to experimental data for an assessment of the accuracy of FUN3D for predicting inlet performance for the C607 propulsion model.

4.1 Problem Description

For this work, simulations were performed over a range of mass flow rates considered in the wind tunnel test. Additionally, the simulations were performed for Mach numbers of 0.80, 1.18, and 1.46. These Mach numbers were chosen to evaluate the predictions at a transonic, low supersonic, and an approximate cruise Mach number. For each Mach number, an angle of attack near the proposed cruise angle of 2° was chosen. The selected conditions are provided in Table 2.

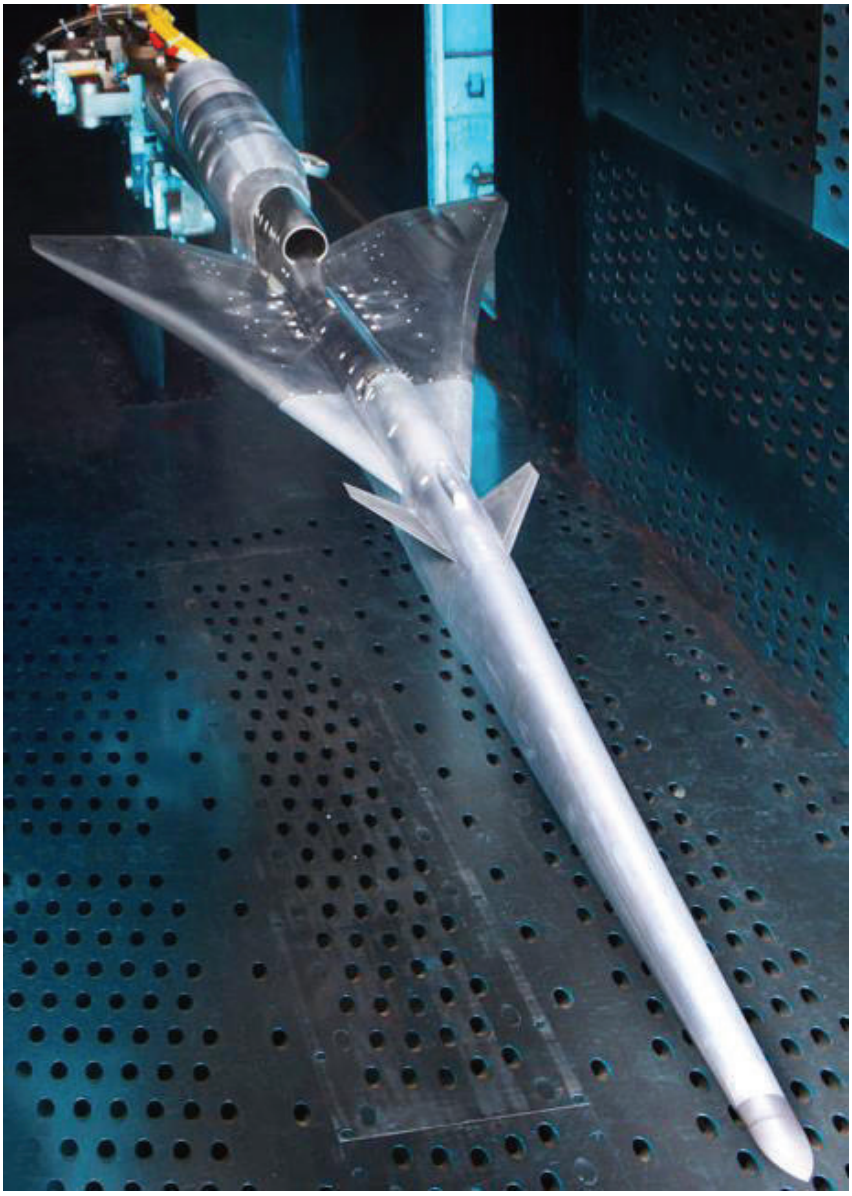

Figure 29. C607 Propulsion Model.

Table 2. Nominal conditions simulated for C607 propulsion model studies.

Mach	α	β
0.80	3.0°	0°
1.18	3.0°	0°
1.46	2.0°	0°

4.1.1 Geometry and Instrumentation

The 8x6 Supersonic Wind Tunnel test considered several variations of the geometry including two inlet geometries and four vortex generator (VG) configurations. This work considered the C607.2 inlet geometry, designated as the C607 propulsion model, with the baseline vortex generators, as shown in Figure 30. The C607 propulsion model was instrumented with a series of 16 static pressure ports along the centerline of the model along with a 40-probe rake at the AIP, see Figure 31. Note that the 40-probe rake additionally featured dynamic probes on selected rakes and 8 static ports on the walls of the inlet, in between the rakes. However, data taken from the dynamic probes were not considered for this work. For more information regarding the other geometry variations, the reader is referred to the wind tunnel test report [1].

(a) Baseline VGs.

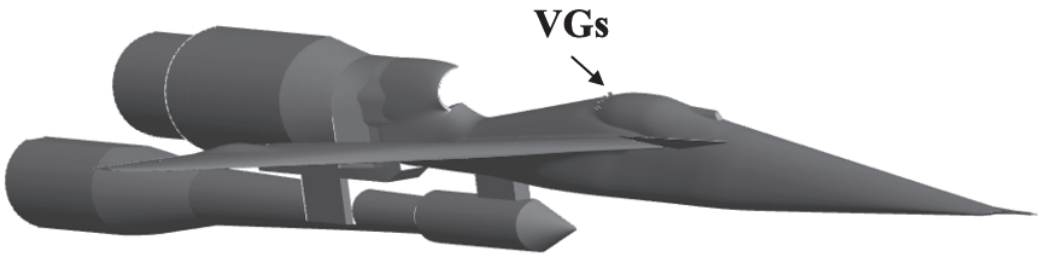

(b) C607 propulsion model with baseline VGs.

Figure 30. Illustration of VG configuration.

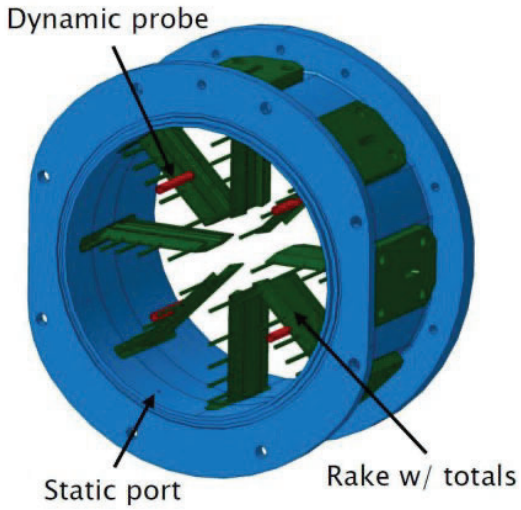

(a) AIP instrumentation.

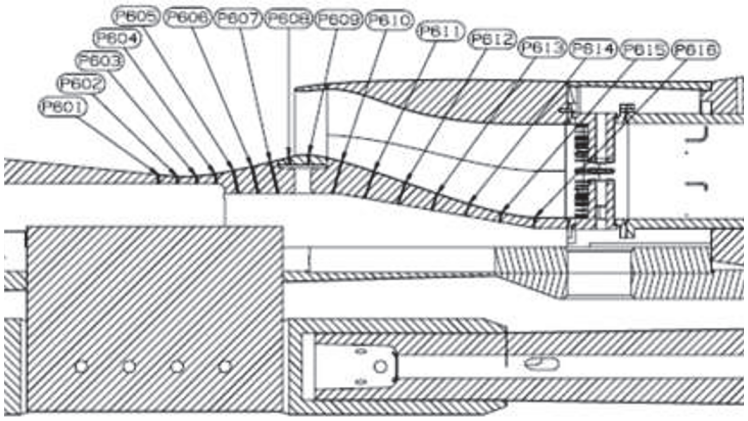

(b) Static pressure ports.

Figure 31. C607 Propulsion Model Instrumentation.

4.1.2 Outflow Boundary Modeling

Two versions of the computational geometry were considered for this work. The primary model, illustrated in Figure 32, employed an outflow boundary 0.5 AIP diameters downstream of the AIP. The majority of the simulations performed for the C607 propulsion model employed this version of the geometry to enable control of the mass flow rate through modification to the back pressure at the outflow boundary. The secondary model, illustrated in Figure 33, included a simplified representation of the mass flow plug assembly utilized for the wind tunnel test. Note that this version of the geometry required more effort to control the mass flow rate since the plug itself must be translated. As a result, only a select number of simulations were performed with this geometry to enable comparisons over an

adequate range of mass flow rates.

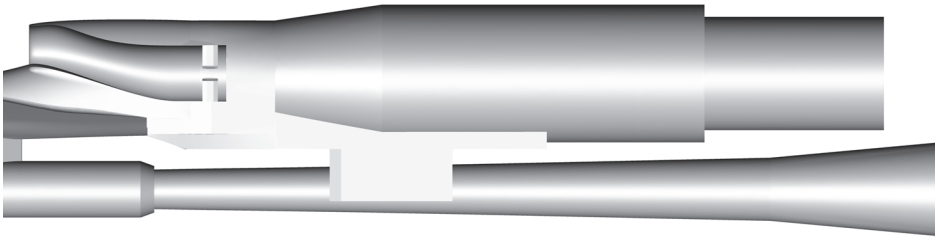

Figure 32. C607 propulsion model with outflow boundary.

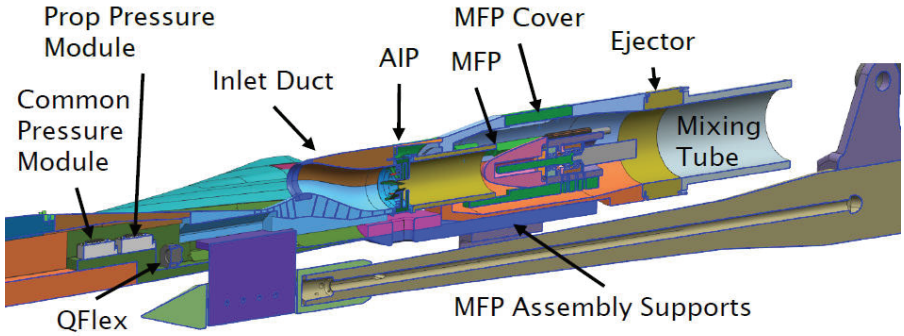

(a) MFP assembly.

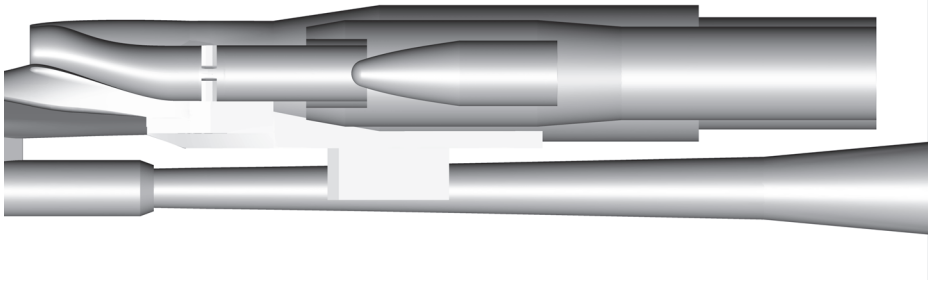

(b) C607 propulsion model with mass flow plug.

Figure 33. Illustration of MFP geometry.

4.1.3 Outflow Boundary Location

A study was performed to assess the impact of the distance between the AIP and the outflow boundary. Previous work has shown that, for some cases, the solution at the AIP is impacted by the location of the outflow boundary. The present study

considered six locations including the baseline, which is located at 0.5 AIP diameters downstream of the AIP. The five additional locations include distances of 2.5, 4.5, 6.5, 8.5, and 10.5 AIP diameters downstream of the AIP, see Figure 34.

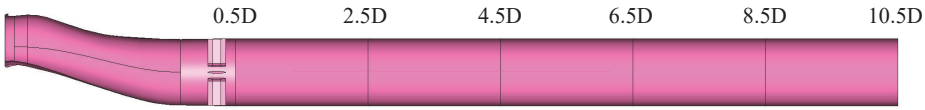

Figure 34. Outflow boundary locations measured in AIP diameters downstream of the AIP.

4.2 Discussion

A description of the computational grids is provided in Section 4.2.1. The results and discussion for the grid refinement and outflow boundary location studies are provided in Sections 4.2.2 and 4.2.3. Section 4.2.4 includes comparisons to experimental data over a range of mass flow rates. The comparisons are repeated to investigate the impact of turbulence model in Section 4.2.6, boundary condition type in Section 4.2.5, and flux limiter in Section 4.2.7. Next, predictions obtained using the outflow version of the model are compared to those obtained using the MFP geometry over a range of mass flow rates in Section 4.2.8. Finally, a summary of the C607 propulsion model studies is provided in Section 4.3.

4.2.1 Computational Grids

Mixed-element, viscous grids were generated using the Heldenmesh™ v3.08 grid generation software [12]. The baseline grid for this geometry is illustrated in Figure 35. The initial wall spacing for the baseline grid was determined based on a desired y^+ of 1 for a flow condition corresponding to Mach and unit Reynolds numbers of 1.46 and 4.95×10^6/ft, which represents the most limiting condition considered for this study. The resulting grid consisted of 3.13×10^6 nodes for the half-span geometry.

To enable an assessment of the impact of grid refinement on the C607 predictions, a series of grids were generated using the baseline as the starting point. Note that the process described in Section 3.3.1 was applied to generate the grids for the C607 propulsion model. The resulting grid sizes are provided in Table 3 and illustrated in Figure 36.

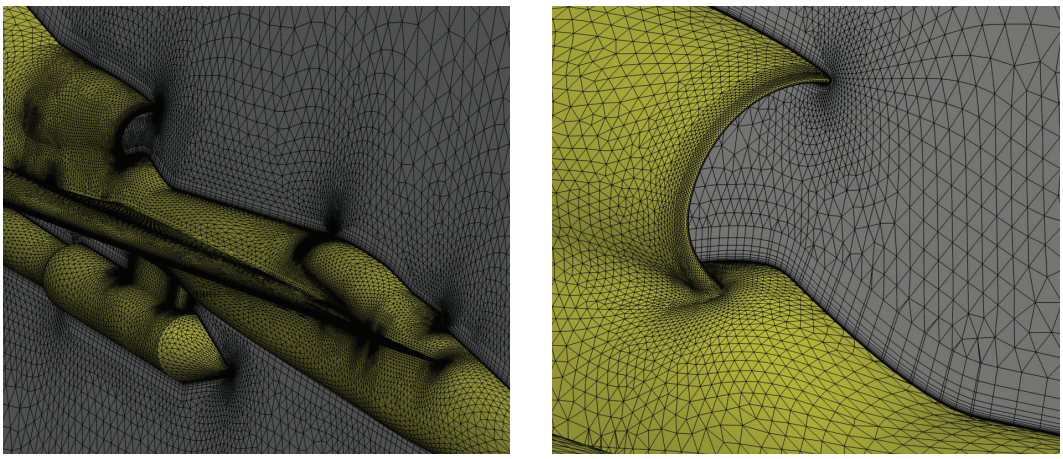

(a) Perspective view.

(b) Zoomed-in view of inlet.

Figure 35. Illustration of baseline grid for C607 propulsion model.

Table 3. Grid sizes for C607 propulsion model.

	h	y^+	r_1	r_2	Nodes (Millions)
Tiny	1.000	1.000	0.200	0.02	3.13
Coarse	0.690	0.690	0.138	0.02	5.59
Medium	0.455	0.455	0.092	0.02	10.9
Fine	0.320	0.320	0.064	0.02	20.0
Extra Fine	0.225	0.225	0.045	0.02	37.8

4.2.2 Grid Refinement Study

For the grid refinement study, a single mass flow rate was chosen for comparison at each of the three flow conditions considered. The plot provided in Figure 37 illustrates the experimentally obtained pressure recovery as a function of the corrected flow for the three flow conditions of interest. As illustrated in the plot, the corrected flow value of approximately 1.25 $\mathrm{lb_m/s}$ was chosen for the grid refinement study. For this study, the PID controller, discussed in Section 2.2, was applied at the outflow boundary to update the back pressure every 250 iterations until the target mass flow rate was achieved.

This problem poses challenges with startup transients that can potentially lead to divergence. To prevent this issue, a multistep process was employed. The first step was to perform 1^{st}-order iterations using a Mach BC at the outflow boundary with a Mach number target of 0.35. The next two steps employ a fixed SPR at the outflow boundary, utilizing both 1^{st}- and 2^{nd}-order iterations, to allow the solution to set up prior to any back pressure updates. The final step consisted of activating the PID controller to achieve the target mass flow rate. This solution process worked

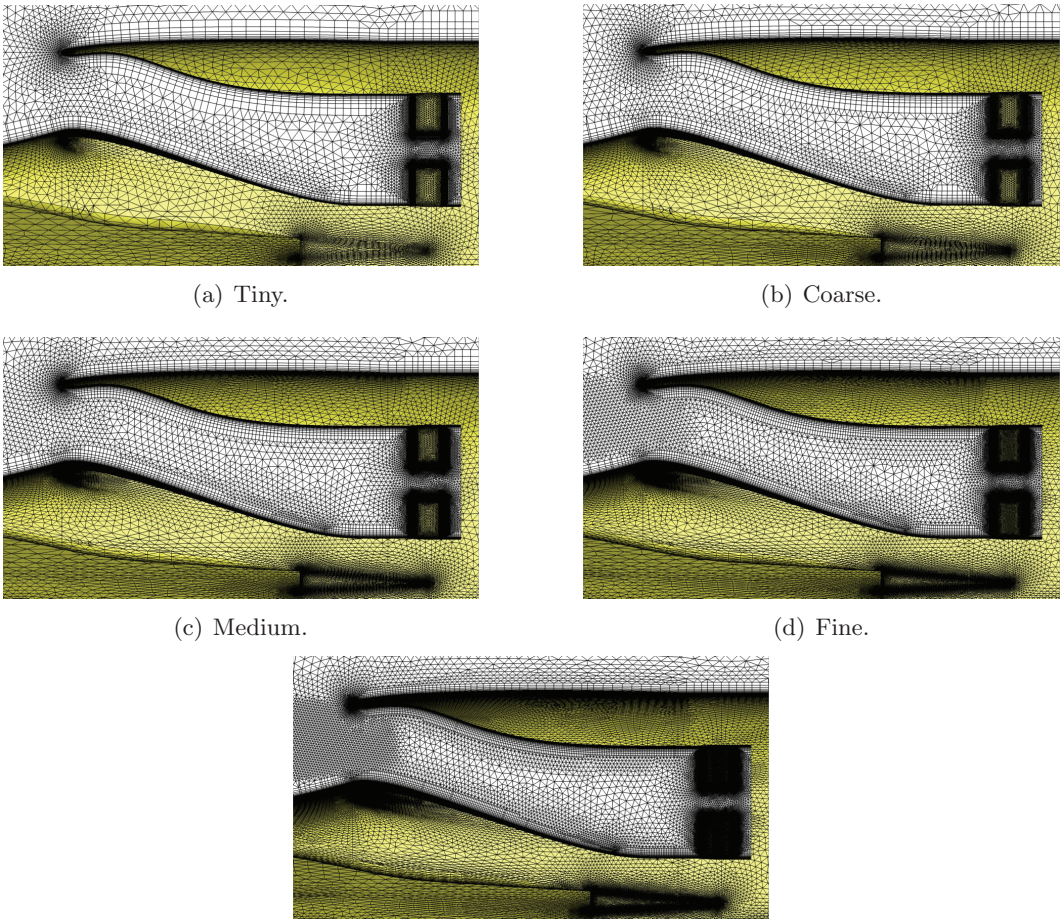

(a) Tiny.

(b) Coarse.

(c) Medium.

(d) Fine.

(e) Extra Fine.

Figure 36. Grid refinement series for C607 propulsion model.

well for all cases discussed. The question of whether to freeze the limiter or not was posed due to the observation that freezing the limiter prematurely can lead to issues with the PID controller. The solution required that the controller be fully converged prior to freezing the limiter, which added to the computational cost. Based on this observation, a study was performed to assess the impact of freezing the limiter on the predicted inlet performance. The convergence history is provided in Figure 38 for the case of Mach 1.46 and the medium grid.

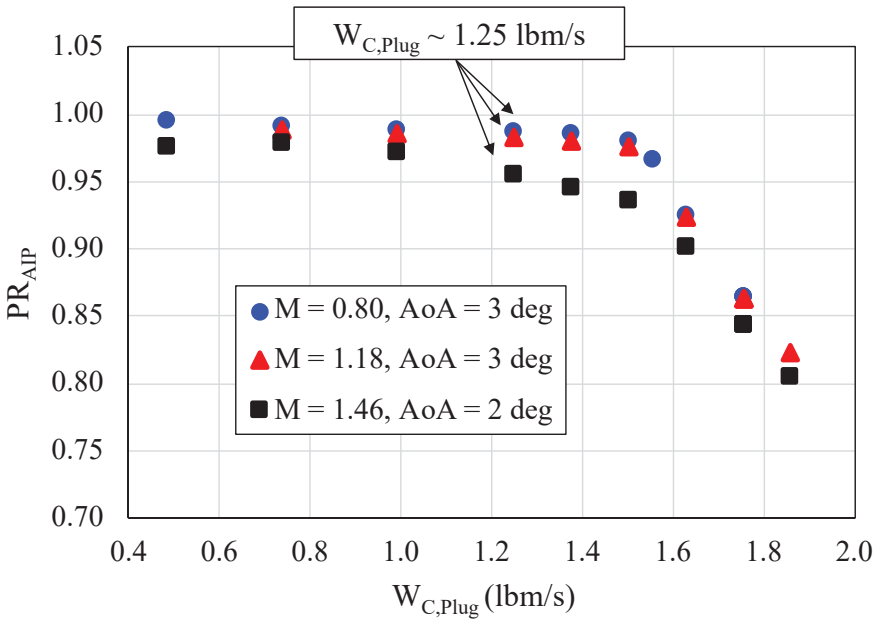

Figure 37. Simulated flow conditions for C607 propulsion model.

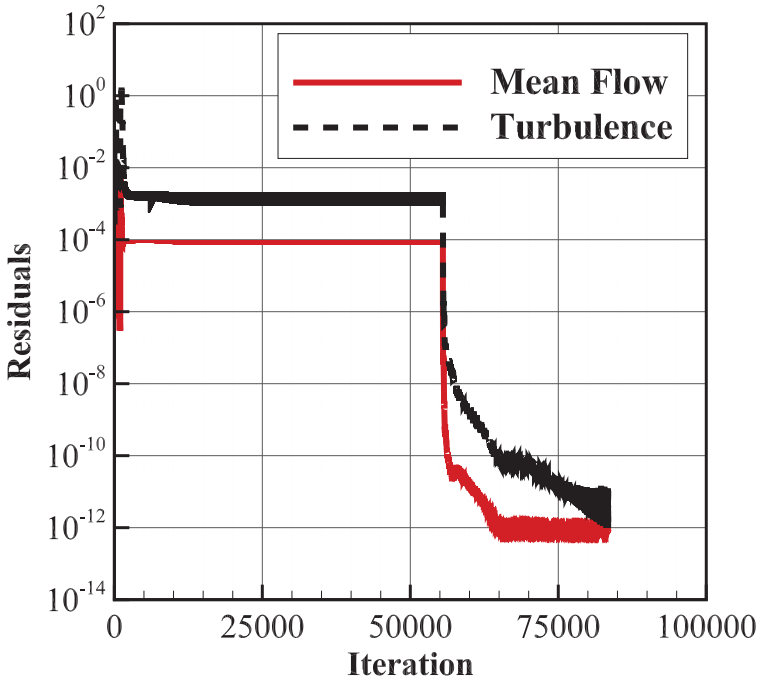

(a) Residual history.

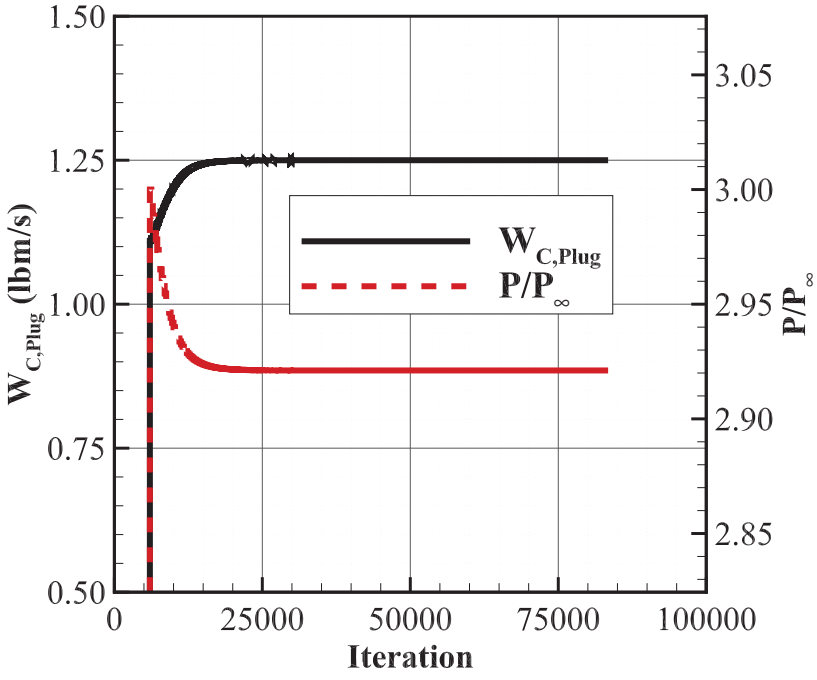

(b) Controller history.

Figure 38. Iterative convergence for medium grid at condition corresponding to M = 1.46, Re = 4,947,000/ft, $\alpha = 2°$, $\beta = 0°$, and $W_{C,Plug}$ = 1.25 $\mathrm{lb_m/s}$.

The results provided in Figure 38a illustrate the iterative histories of the mean flow and turbulence residuals. The residuals are shown to exhibit limit cycle behavior until the limiter is frozen after 55,000 iterations. Once the limiter is frozen, the residuals drop down to near machine zero. The results provided in Figure 38b illustrate the convergence of the PID controller. The PID controller history shows that the mass flow rate is converged after 25,000 iterations.

In order to assess the impact of freezing the limiter on the predicted inlet performance, the solution at the AIP was extracted before and after freezing the limiter. Contour plots of the pressure recovery at the AIP are provided in Figure 39. The resulting values for the average pressure recovery (PR_{AIP}), radial distortion metric (IDR_{max}), and circumferential distortion metric (IDC_{max}) are also provided for the two solutions. The distortion metrics, IDR_{max} and IDC_{max}, correpond to the maximum values of the General Electric distortion metrics, IDC and IDR [16]. Freezing the limiter results in improved convergence of the residuals, but does not appear to have an impact on the flow at the AIP. Note that this assumes that both solutions, before and after freezing the limiter, have achieved the target mass flow rate. Due to this result, the limiter was not frozen for any solutions utilizing the PID controller.

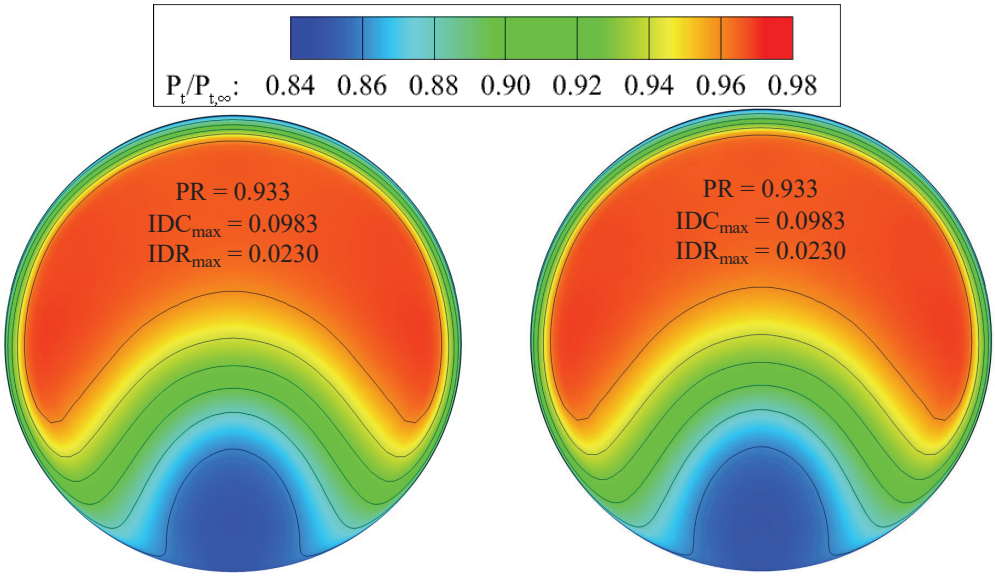

(a) Before freezing limiter.

(b) After freezing limiter.

Figure 39. Contours plots of pressure recovery at the AIP with and without freezing the flux limiter; medium grid, $M = 1.46$, Re = 4,947,000/ft, $\alpha = 2°$, $\beta = 0°$, and $W_{C,Plug} = 1.25$ $\mathrm{lb_m/s}$.

Results: Mach 0.80

The results of the grid refinement study for the case of Mach 0.8 are provided in Figures 40 through 43. Figure 40 provides the predicted values for IDC_{max}, IDR_{max}, and PR_{AIP} as a function of grid refinement, where N is the number of nodes. Note that the experimental values are provided as dashed black lines for reference. The results show that the FUN3D predicted IDC_{max} increases as the grid refinement increases, while both the IDR_{max} and pressure recovery at the AIP decrease with increasing grid refinement. Also, the trends show that the FUN3D predictions are moving away from the experimental values of IDC_{max} and IDR_{max} with differences of 15% and -7.6% between the experimental values and the finest grid solutions, respectively. The pressure recovery results show that FUN3D is trending towards the experimental data with increasing grid refinement with a difference of less than 1% between the experimental value and the finest grid level. Note that grid convergence was not achieved for this flow condition.

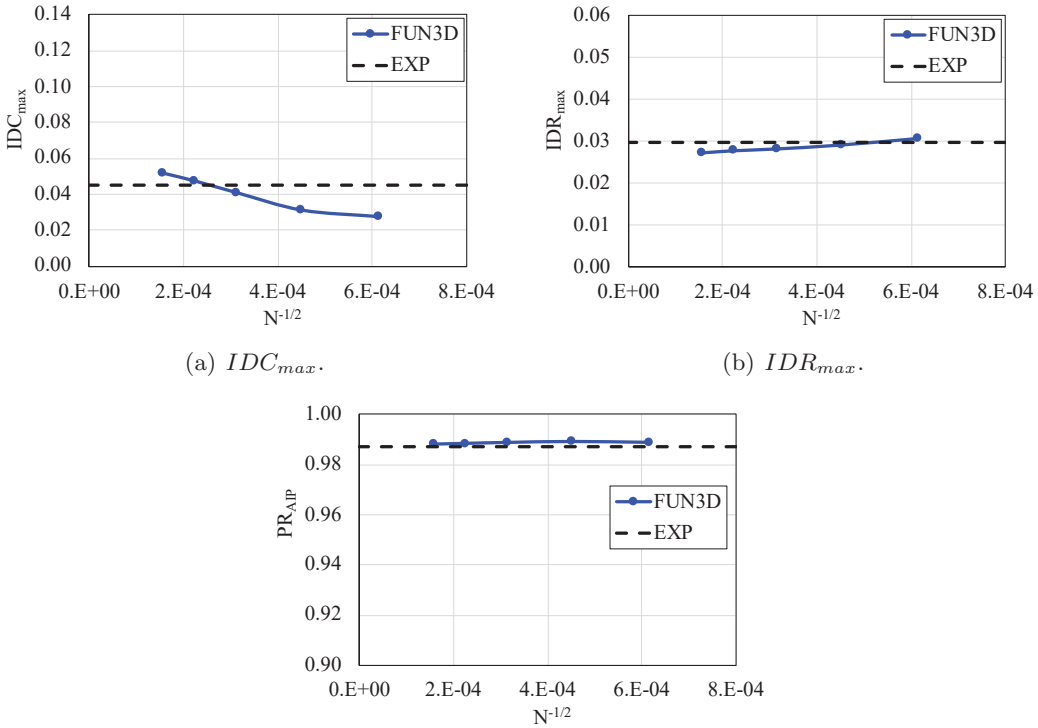

(a) IDC_{max}.

(b) IDR_{max}.

(c) PR_{AIP}.

Figure 40. Inlet distortion and pressure recovery predictions as a function of grid refinement; $M = 0.8$, Re = 4,191,000/ft, $\alpha = 3°$, $\beta = 0°$, and $W_{C,Plug} = \mathrm{lb_m/s}$.

The predicted distributions of pressure recovery for AIP rings 1 through 5 and static pressure along the centerline are provided in Figure 41 as a function of grid refinement. For rings 1 through 3, the results show favorable agreement, with FUN3D tending to slightly over- or underpredict the pressure recovery at 180 degrees. Also, the FUN3D predictions generally trend toward the experimental data with increas-

ing grid refinement. The maximum absolute difference between the FUN3D predicted pressure recovery and experimental values occurs at 180 degrees, and is observed to be 1% or less for rings 1 through 3. For rings 4 and 5, the maximum absolute differences are observed to be 2% or less, and occur at the 135 and 225 degree locations. Note that the largest differences are observed for ring 5, which consists of the probes closest to the inlet surface. Rings 4 and 5 display asymmetry in the experimentally obtained pressure recovery values that do not show up in the FUN3D predictions. The FUN3D simulations were performed using a half-span grid with a symmetry condition enforced at the centerline plane. As a result, the FUN3D predictions are forced to be symmetric. However, a one-off study was performed to compare FUN3D solutions obtained using both half- and full-span grids, which showed identical predictions. Finally, the static pressure values provided in Figure 41f illustrate favorable agreement between FUN3D and experiment both upstream and downstream of the inlet face.

Pressure recovery contour plots at the AIP are provided for the five grid refinement levels in Figure 42. The results show that the low-pressure region at the bottom of the AIP increases in size with increasing grid refinement. The solution is still slightly changing with grid refinement, which was also evident in the results provided in Figures 40 and 41.

Finally, Mach contour plots at the $y = 0$ plane are provided in Figure 43 for the five grid refinement levels. Again, the low-pressure region at the bottom of the inlet is shown to increase in size with increasing grid refinement. The remainder of the domain appears qualitatively similar for all grid levels shown.

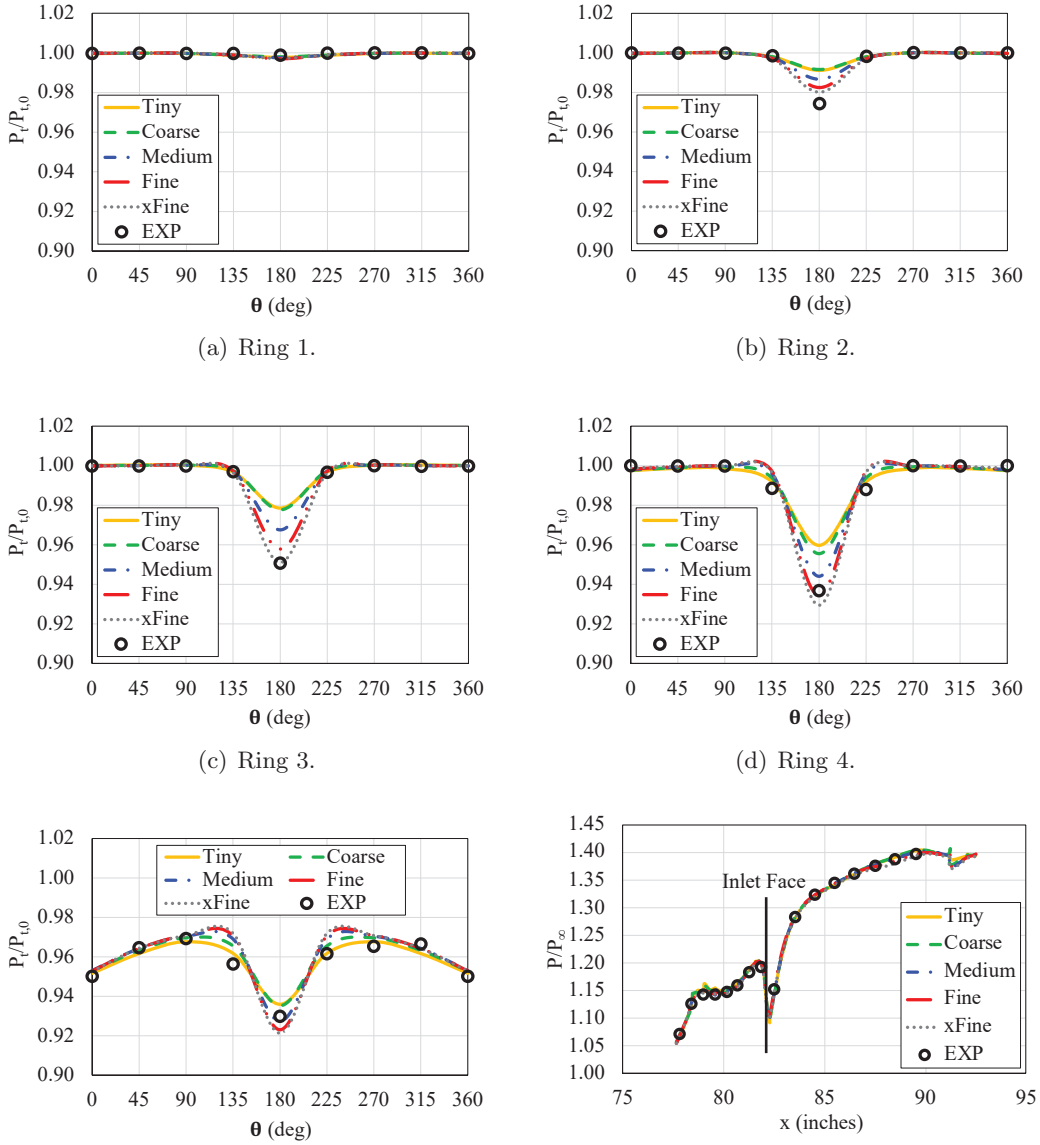

(a) Ring 1.

(b) Ring 2.

(c) Ring 3.

(d) Ring 4.

(e) Ring 5.

(f) Static pressure ports.

Figure 41. Comparisons to experimental data as a function of grid refinement at the AIP and static pressure ports; $M = 0.8$, Re = 4,191,000/ft, $\alpha = 3°$, $\beta = 0°$, and $W_{C,Plug} = 1.25$ $\mathrm{lb_m/s}$.

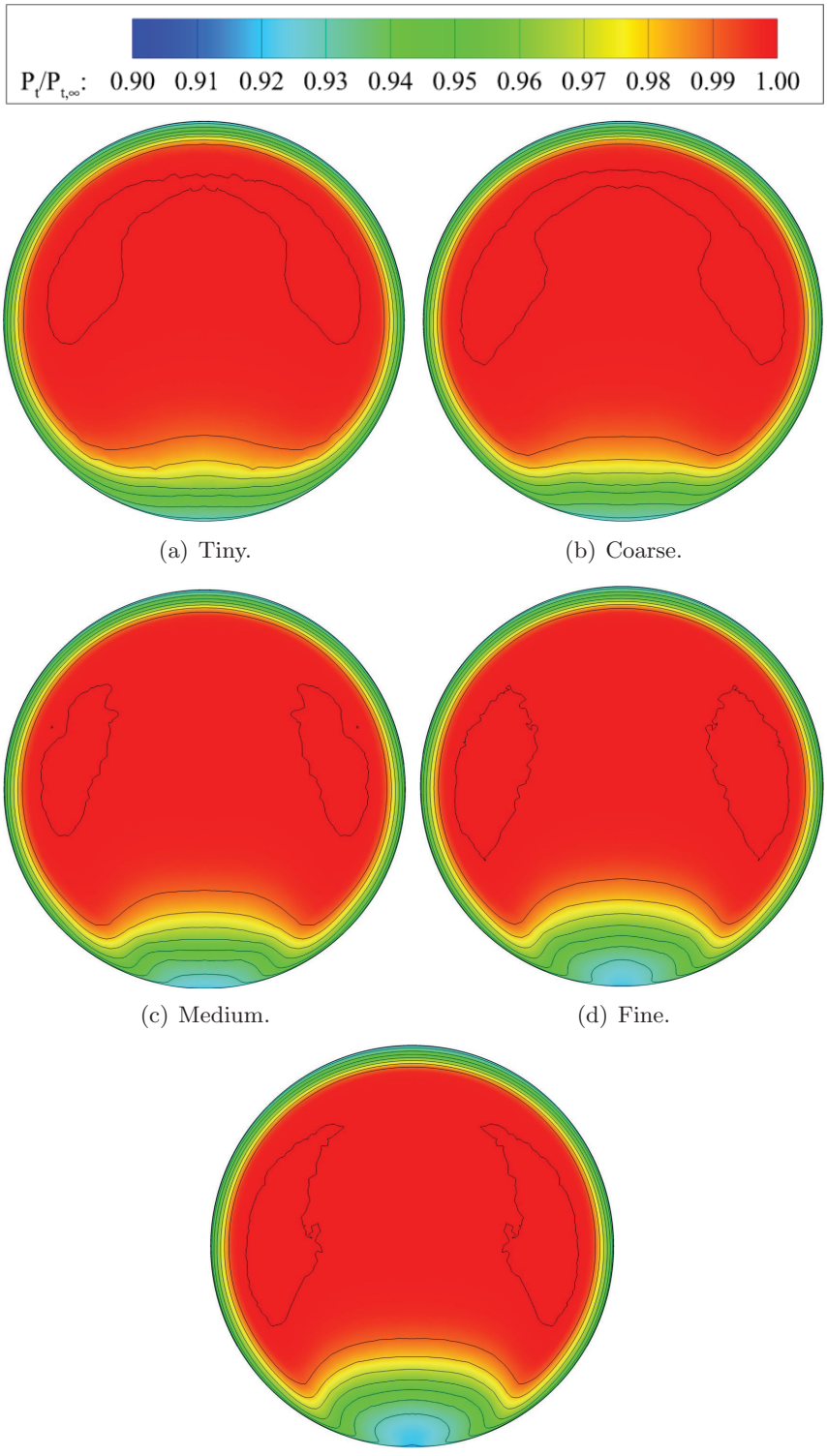

(a) Tiny.

(b) Coarse.

(c) Medium.

(d) Fine.

(e) Extra Fine.

Figure 42. Pressure recovery contours at the AIP as a function of grid refinement; $M = 0.8$, Re = 4,191,000/ft, $\alpha = 3°$, $\beta = 0°$, and $W_{C,Plug} = 1.25$ $\mathrm{lb_m/s}$.

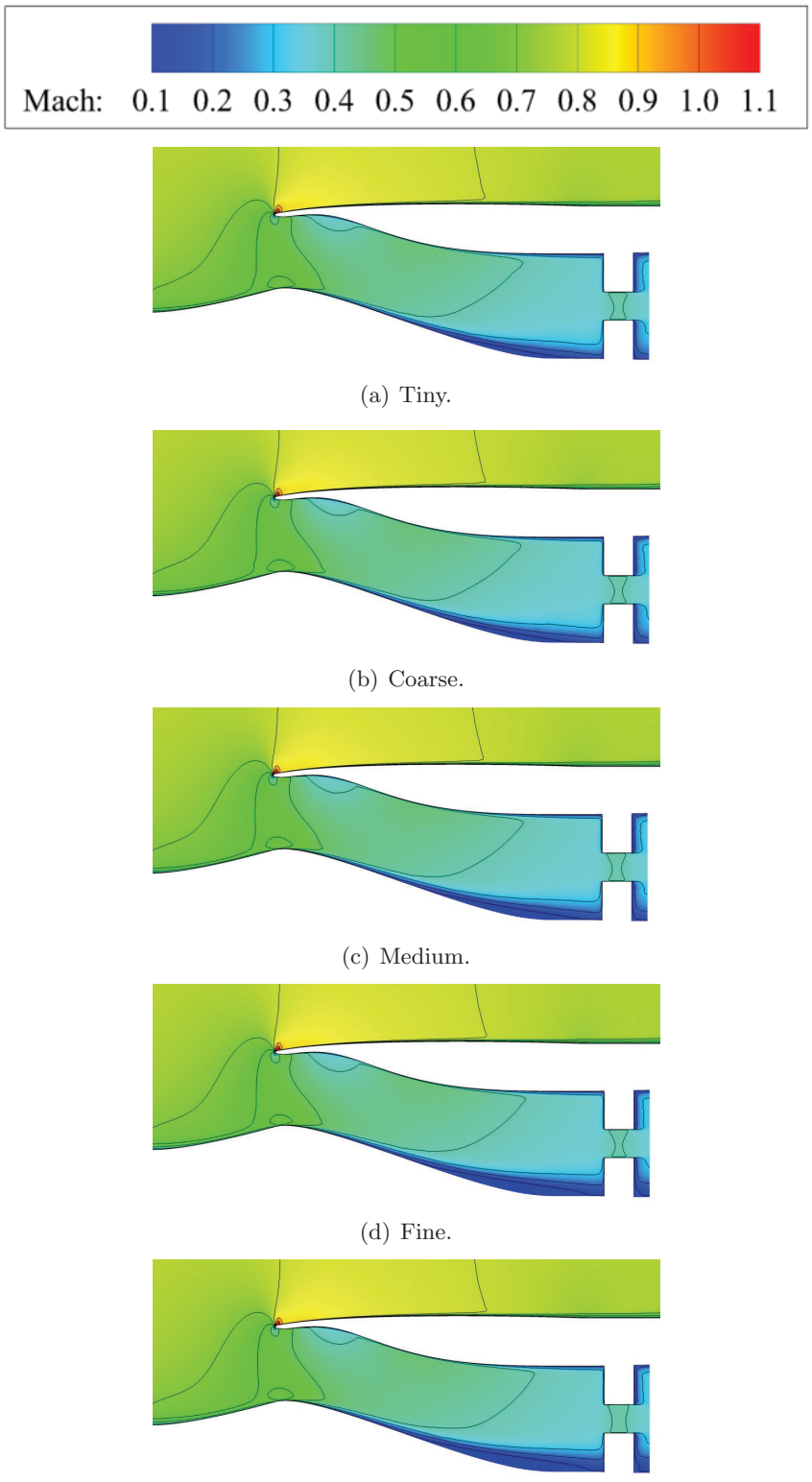

(a) Tiny.

(b) Coarse.

(c) Medium.

(d) Fine.

(e) Extra Fine.

Figure 43. Mach number contours at $y = 0$ plane as a function of grid refinement; $M = 0.8$, Re = 4,191,000/ft, $\alpha = 3°$, $\beta = 0°$, and $W_{C,Plug} = 1.25$ $\mathrm{lb_m/s}$.

Results: Mach 1.18

The results of the grid refinement study for the case of Mach 1.18 are provided in Figures 44 through 47. Figure 44 provides the predicted values for IDC_{max}, IDR_{max}, and PR_{AIP} as a function of grid refinement, where N is the number of nodes. The results show that the FUN3D predicted IDC_{max} value increases as the grid refinement increases, while both the IDR_{max} and PR_{AIP} values at the AIP decrease with increasing grid refinement. Also, the trends show that the FUN3D predictions are moving away from the experimental values with increasing grid refinement. The FUN3D results on the finest grid level show absolute differences of 42%, 21%, and 1% relative to the experimental values for IDC_{max}, IDR_{max}, and PR_{AIP}, respectively. Note that grid convergence was also not achieved for this flow condition.

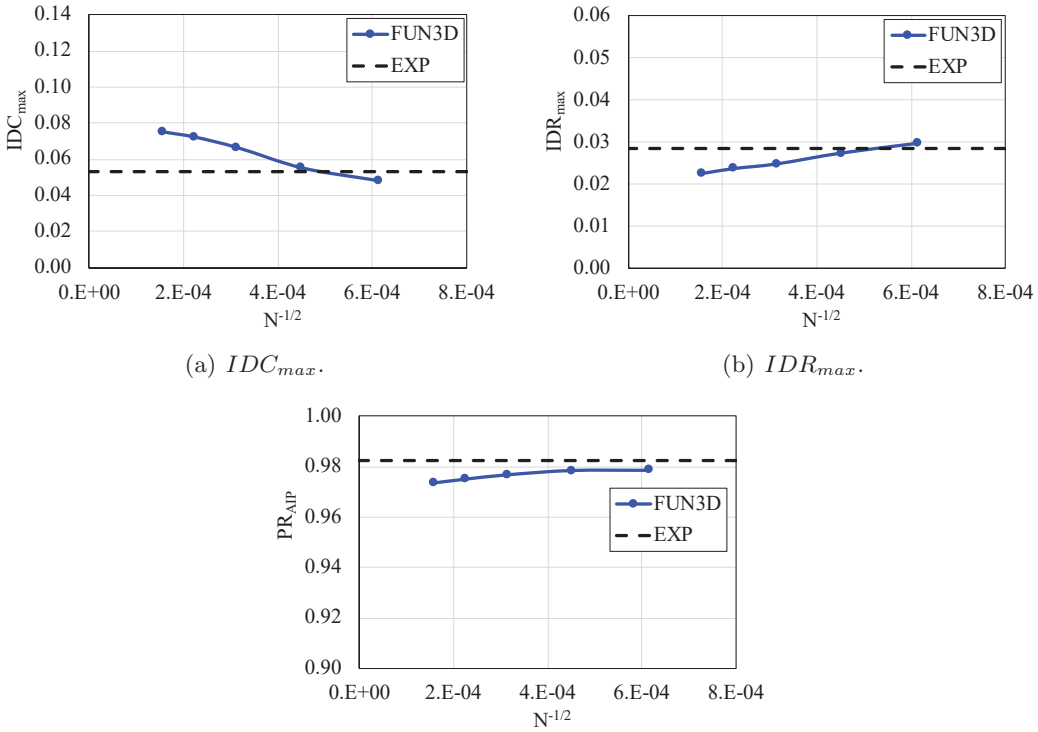

(a) IDC_{max}.

(b) IDR_{max}.

(c) PR_{AIP}.

Figure 44. Inlet distortion and pressure recovery predictions as a function of grid refinement; $M = 1.18$, Re = 4,838,000/ft, $\alpha = 3°$, $\beta = 0°$, and $W_{C,Plug} = 1.25$ lb_m/s.

The predicted distributions of pressure recovery for AIP rings 1 through 5 and static pressure along the centerline are provided in Figure 45 as a function of grid refinement. For this flow condition, FUN3D shows a tendency to underpredict the pressure recovery for all five AIP rings with the largest differences occuring at the 180-degree location. The FUN3D predictions are observed to trend away from the experimental data with increasing grid refinement, which was also observed in the

results shown in Figure 44. The maximum absolute differences in pressure recovery for the Mach 1.18 comparisons are observed to be 2.3%, 3.6%, 3.3%, 2.8%, and 2.2% for rings 1 through 5. Finally, the static pressure comparisons, shown in Figure 45f, show that the FUN3D predicted values match the experimental data very well upstream of the inlet face. Downstream of the inlet face, FUN3D underpredicts the static pressure with the differences between the experimental data and FUN3D increasing with increasing grid refinement. For the data shown, the maximum absolute difference in static pressure between the experimental data and finest grid solution is roughly 1.8%.

Pressure recovery contour plots at the AIP are provided for the five grid refinement levels in Figure 46. The results show that the low-pressure region at the bottom of the AIP increases in size with increasing grid refinement. The solution appears to still be changing with grid refinement, which was also evident in the results provided in Figures 44 and 45.

Finally, Mach contour plots at the $y = 0$ plane are provided in Figure 47 for the five grid refinement levels. Again, the low-pressure region at the bottom of the inlet is shown to increase in size with increasing grid refinement. The remainder of the domain appears qualitatively similar for all grid levels shown.

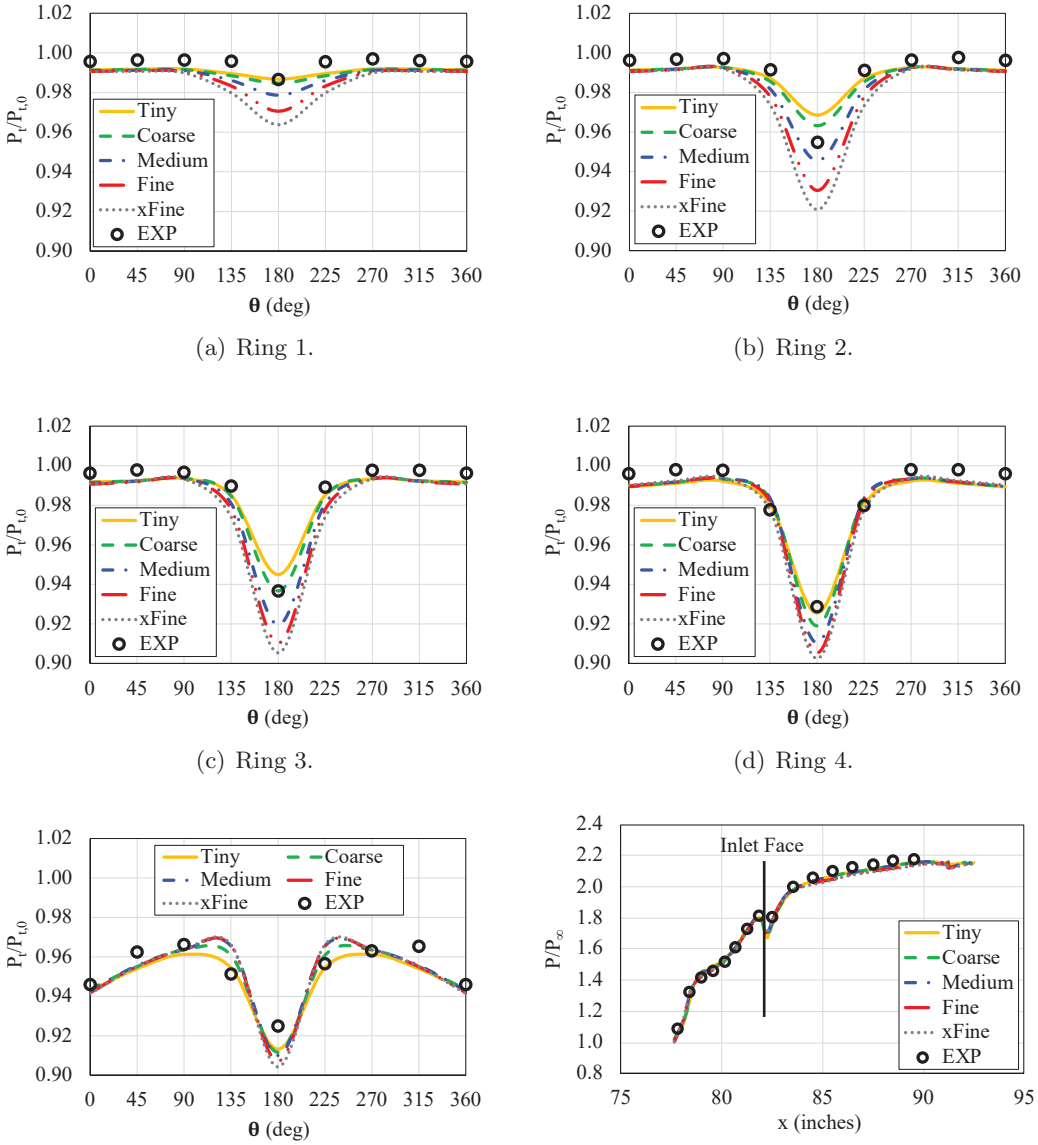

(a) Ring 1.

(b) Ring 2.

(c) Ring 3.

(d) Ring 4.

(e) Ring 5.

(f) Static pressure ports.

Figure 45. Comparisons to experimental data as a function of grid refinement at the AIP and static pressure ports; $M = 1.18$, Re = 4,838,000/ft, $\alpha = 3°$, $\beta = 0°$, and $W_{C,Plug} = 1.25$ $\mathrm{lb_m/s}$.

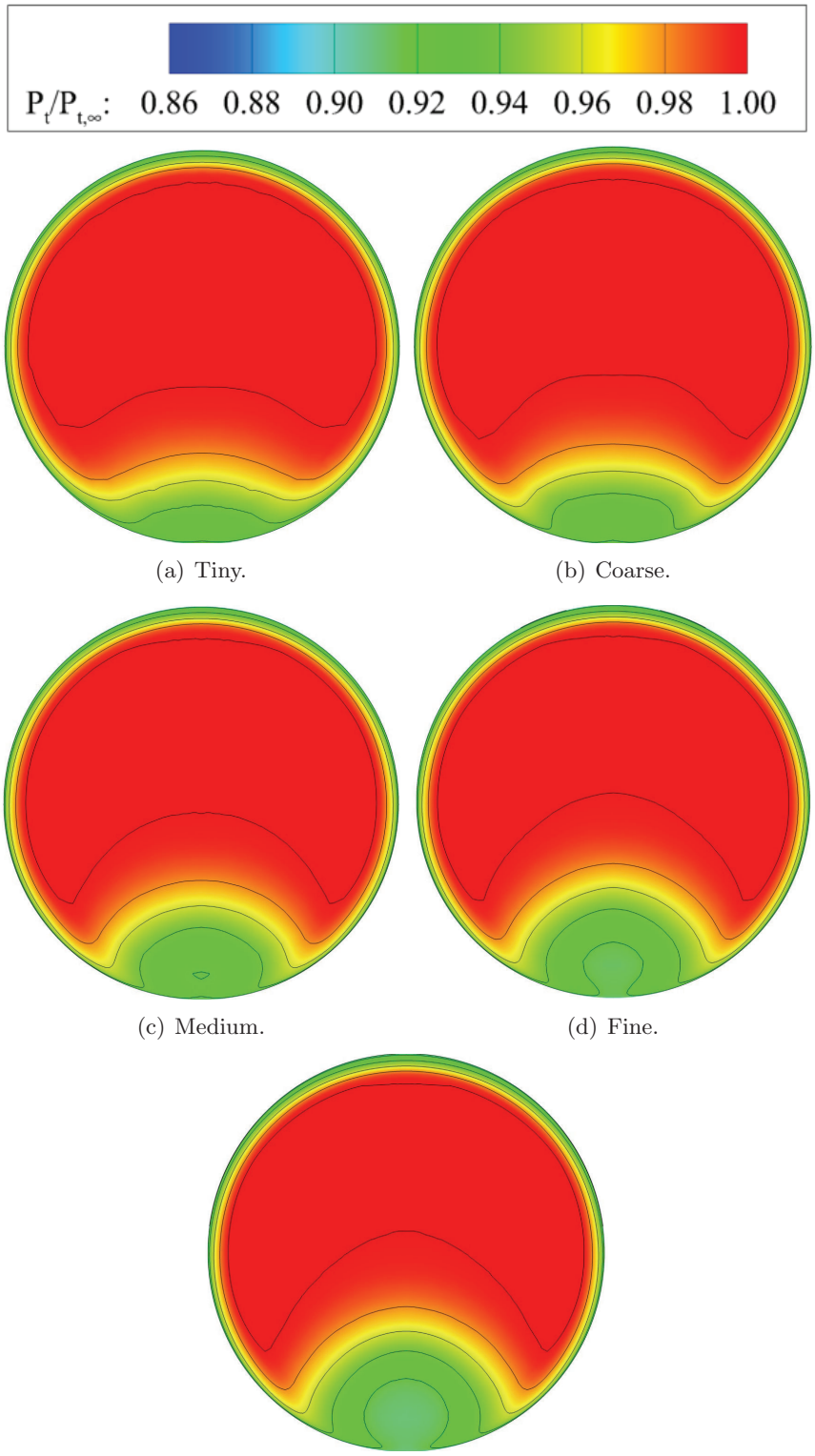

(a) Tiny.

(b) Coarse.

(c) Medium.

(d) Fine.

(e) Extra Fine.

Figure 46. Pressure recovery contours at the AIP as a function of grid refinement; $M = 1.18$, Re = 4,838,000/ft, $\alpha = 3°$, $\beta = 0°$, and $W_{C,Plug} = 1.25$ $\mathrm{lb_m/s}$.

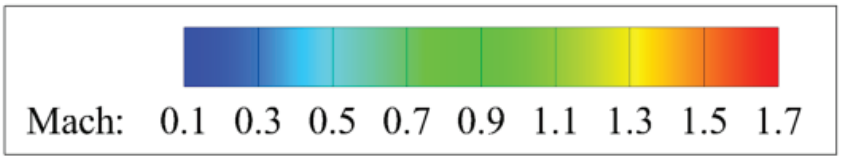

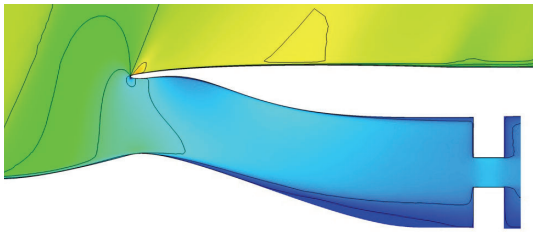

(a) Tiny.

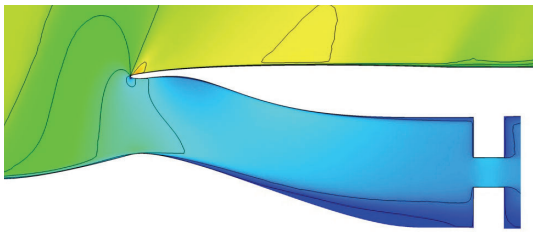

(b) Coarse.

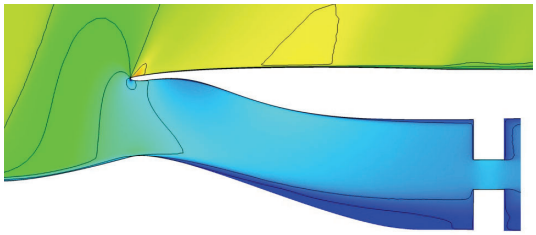

(c) Medium.

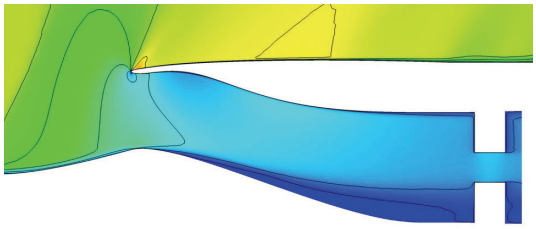

(d) Fine.

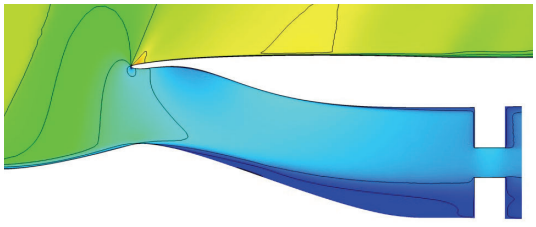

(e) Extra Fine.

Figure 47. Mach number contours at $y = 0$ plane as a function of grid refinement; $M = 1.18$, Re = 4,838,000/ft, $\alpha = 3°$, $\beta = 0°$, and $W_{C,Plug} = 1.25$ $\mathrm{lb_m/s}$.

Results: Mach 1.46

The results of the grid refinement study for the case of Mach 1.46 are provided in Figures 48 through 51. The FUN3D results shown in Figure 48 illustrate a trend of increasing IDC_{max}, and decreasing IDR_{max} and PR_{AIP} with increasing grid refinement. Also, the trends show that, once again, the FUN3D predictions are moving away from the experimental values with increasing grid refinement. The FUN3D results on the finest grid level show absolute differences of 102%, 40%, and 3.3% relative to the experimental values for IDC_{max}, IDR_{max}, and PR_{AIP}, respectively. Also, the results indicate that the differences could potentially increase with further increases in grid resolution. However, it is unclear whether this trend would continue on its current path, and no definitive conclusion can be made in that regard.

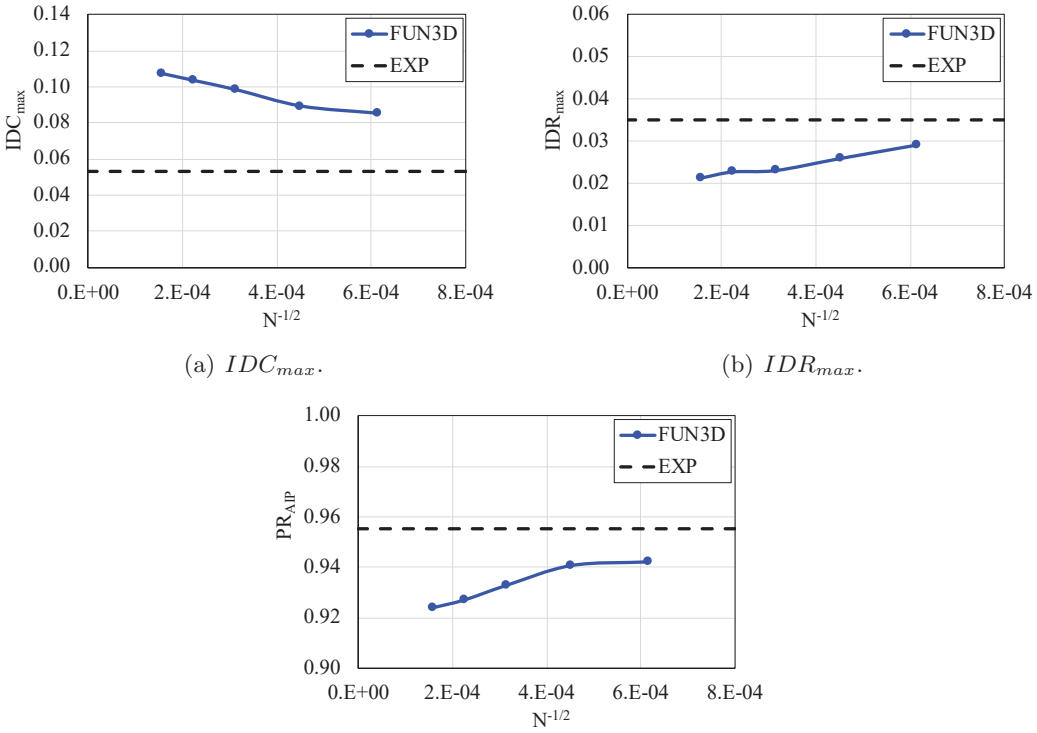

(a) IDC_{max}.

(b) IDR_{max}.

(c) PR_{AIP}.

Figure 48. Inlet distortion and pressure recovery predictions as a function of grid refinement; $M = 1.46$, Re = 4,947,000/ft, $\alpha = 2°$, $\beta = 0°$, and $W_{C,Plug} = 1.25$ lb_m/s.

The predicted distributions of pressure recovery for AIP rings 1 through 5 and static pressure along the centerline are provided in Figure 49 as a function of grid refinement. For this flow condition, FUN3D shows a tendency to underpredict the pressure recovery for all five AIP rings with the largest differences occuring at the 180-degree location. Additionally, the FUN3D predictions are observed to trend away from the experimental data with increasing grid refinement, which was also

observed in the results shown in Figure 48. The maximum absolute differences in pressure recovery for the Mach 1.46 comparisons are observed to be 9.4%, 9%, 8.4%, 7.9%, and 7.3% for rings 1 through 5. Finally, the static pressure comparisons, shown in Figure 49f, show that the FUN3D predicted values match the experimental data very well upstream of the inlet face, and even appears to accurately capture the location of the shock present on the inlet bump. Downstream of the inlet face, FUN3D underpredicts the static pressure with the differences between the experimental data and FUN3D increasing with increasing grid refinement. For the data shown, the maximum absolute difference is roughly 6% for the finest grid level.

Pressure recovery contour plots at the AIP are provided for the five grid refinement levels in Figure 50. The results show that the low-pressure region at the bottom of the AIP increases in size with increasing grid refinement. Once again, the solution is still slightly changing with grid refinement, which agrees with the results provided in Figures 48 and 49.

Finally, Mach contour plots at the $y = 0$ plane are provided in Figure 51 for the five grid refinement levels. Again, the low-pressure region at the bottom of the inlet is shown to increase in size with increasing grid refinement. The remainder of the domain appears qualitatively similar for all grid levels shown.

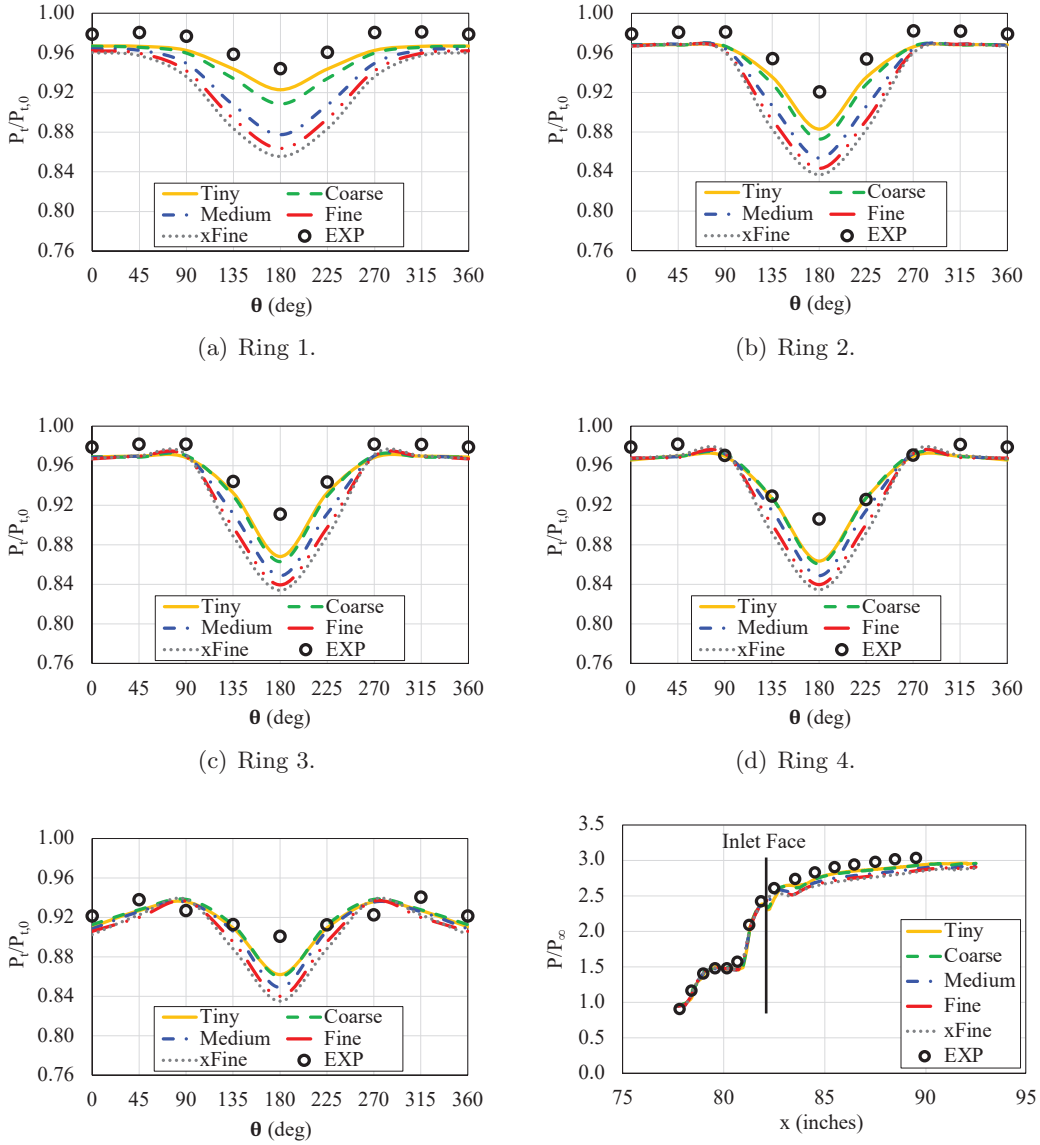

(a) Ring 1.

(b) Ring 2.

(c) Ring 3.

(d) Ring 4.

(e) Ring 5.

(f) Static pressure ports.

Figure 49. Comparisons to experimental data as a function of grid refinement at the AIP and static pressure ports; $M = 1.46$, Re = 4,947,000/ft, $\alpha = 2°$, $\beta = 0°$, and $W_{C,Plug} = 1.25$ $\mathrm{lb_m/s}$.

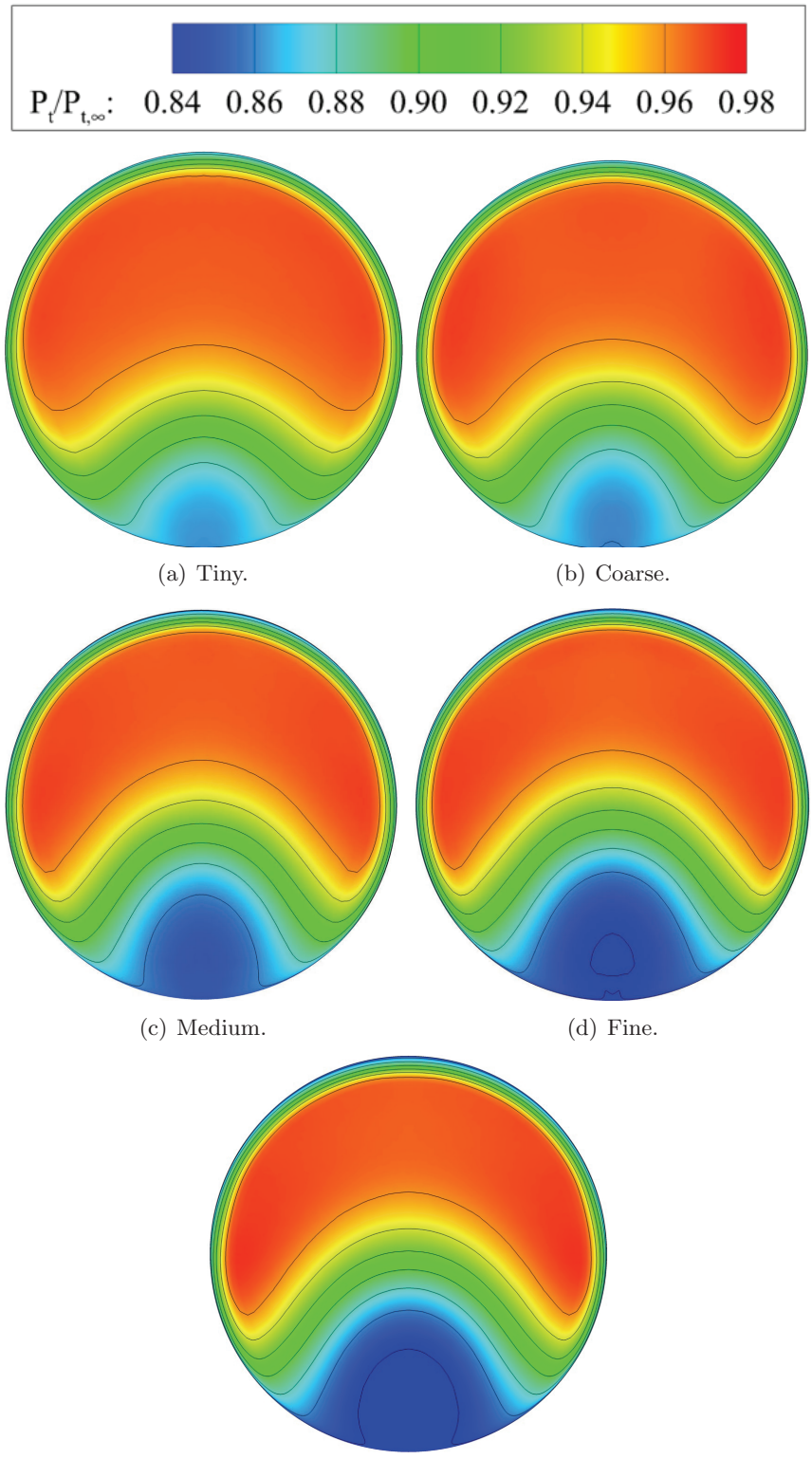

(a) Tiny.

(b) Coarse.

(c) Medium.

(d) Fine.

(e) Extra Fine.

Figure 50. Pressure recovery contours at the AIP as a function of grid refinement; $M = 1.46$, Re = 4,947,000/ft, $\alpha = 2°$, $\beta = 0°$, and $W_{C,Plug} = 1.25$ $\mathrm{lb_m/s}$.

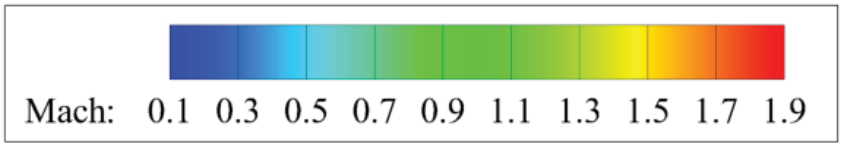

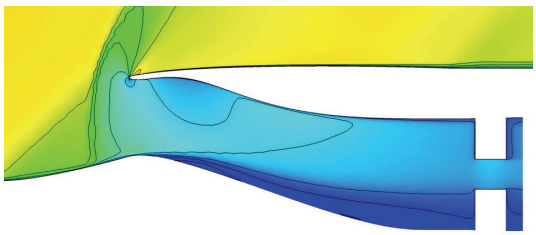

(a) Tiny.

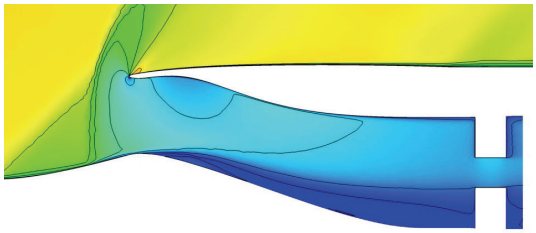

(b) Coarse.

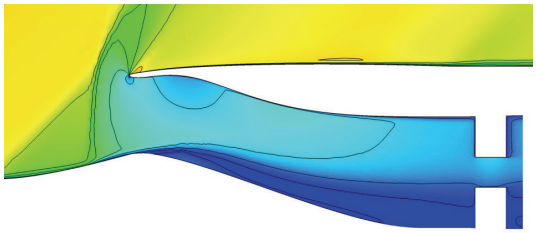

(c) Medium.

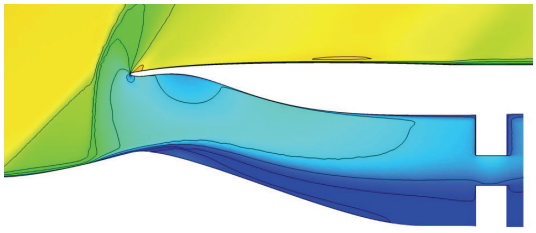

(d) Fine.

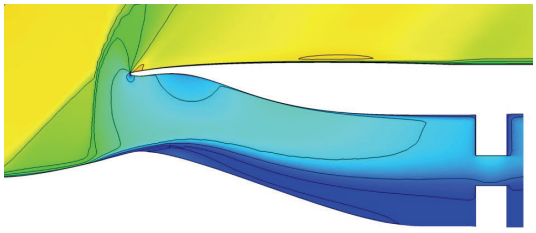

(e) Extra Fine.

Figure 51. Mach number contours at $y = 0$ plane as a function of grid refinement; $M = 1.46$, Re = 4,947,000/ft, $\alpha = 2°$, $\beta = 0°$, and $W_{C,Plug} = 1.25$ $\mathrm{lb_m/s}$.

The results of the grid refinement study performed for Mach numbers of 0.8, 1.18, and 1.46 were discussed in this subsection. For each Mach number, a corrected flow rate of 1.25 lb_m/s was achieved using the PID-controller capability available in FUN3D. The simulations considered half-span grid sizes ranging from 3 to 38 million nodes. The grid refinement study results showed that grid convergence was not achieved for any case. Of the metrics considered, the pressure recovery at the AIP tends to agree most favorably with the experimental data, while the FUN3D predicted values for IDC_{max} and IDR_{max} exhibited the largest differences relative to the experimental data. Interestingly, the FUN3D predictions were shown to generally trend away from the experimental data with increasing grid refinement with FUN3D showing the tendency to underpredict the total pressure at the AIP. Also, the observed differences between FUN3D and the experimental data were shown to increase with increasing Mach number. Overall, the FUN3D predicted total pressure distributions at the AIP show qualitative agreement with the experimental data.

Based on the results shown, further grid refinement is needed for this problem. Of the grids considered, the finest grid would ideally be employed for the studies to follow. However, the medium grid was chosen for the remainder of the studies to reduce the computational cost and to enable a broader investigation of the configuration.

4.2.3 Outflow Boundary Location Study

The grid refinement study showed that the Mach 1.46 solutions exhibited the largest differences relative to the experimental data. As a result, the Mach 1.46 condition was chosen for the outflow boundary location study discussed in this subsection. The results of the outflow boundary location study are provided in Figure 52, which shows the FUN3D predicted values for IDC_{max}, IDR_{max}, and PR_{AIP} plotted against the distance from the AIP in AIP diameters. Also, the experimentally obtained values are included on the plots as a dashed line. The results show that moving the outflow boundary further from the AIP does not have a significant impact for this problem. Therefore, there is no indication that improved results could be obtained by moving the outflow boundary further downstream. This result confirms the findings discussed for the BLI inlet problem.

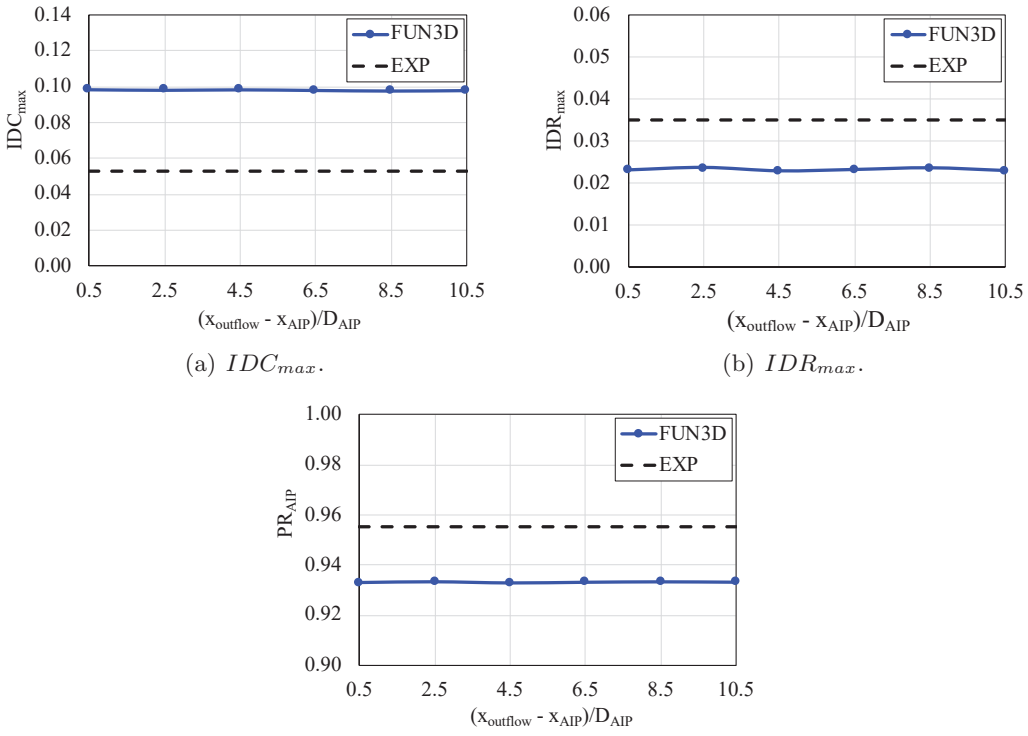

(a) IDC_{max}.

(b) IDR_{max}.

(c) PR_{AIP}.

Figure 52. Inlet distortion and pressure recovery predictions as a function of outflow boundary location; medium grid, $M = 1.46$, Re = 4,947,000/ft, $\alpha = 2°$, $\beta = 0°$, and $W_{C,Plug} = 1.25$ $\mathrm{lb_m/s}$.

4.2.4 Mass Flow Rate Sweeps

The grid refinement study focused on a single mass flow rate through the inlet for each of the three Mach numbers considered. For this part of the study, static pressure ratio (SPR) sweeps are performed for each of the three Mach numbers to enable comparisons to experimental data over a range of mass flow rates. Note that the choice to vary the SPR means that the mass flow rate is an output of the analysis. The mass flow rate controller is critical for simulations where the goal is to match a specific mass flow rate. However, the iterative nature of the controller makes it more computationally expensive relative to a fixed outflow condition, such as the SPR condition utilized in this study. And since the goal is to assess the trends as opposed to a single mass flow rate, the SPR condition was employed for this study to reduce the computational cost of the simulations. The SPR values employed for the sweeps, provided in Table 4, were chosen by trial and error to ensure an adequate range of mass flow rates were obtained.

The results of the SPR sweeps performed for Mach 0.8 are provided in Figure 53, which compares the FUN3D predicted values of IDC_{max}, IDR_{max}, and PR_{AIP} to the experimental data over a range of corrected flow rates at the AIP, $W_{C,Plug}$. For the lower values of corrected flow rate, the FUN3D results agree favorably

Table 4. SPR sweeps performed for each Mach number.

	SPR = P_{back}/P_∞			
Mach = 0.80	1.0	1.2	1.4	1.5
Mach = 1.18	1.8	2.0	2.2	2.3
Mach = 1.46	2.6	2.8	3.0	3.2

with the experimental data. However, the predictions appear to diverge from the experimental data as mass flow rate is increased. Note that only four points are plotted for the FUN3D curves. Lines were added between the FUN3D points to make it easier to differentiate between the experimental data and the CFD. However, the lines can be misleading since there are not enough data to fully resolve the nonlinear portions.

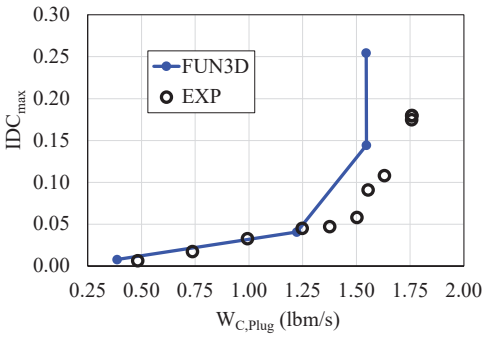

(a) IDC_{max}.

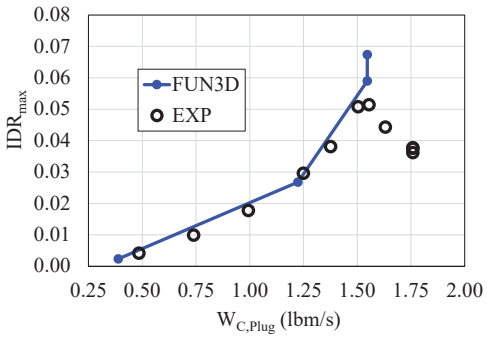

(b) IDR_{max}.

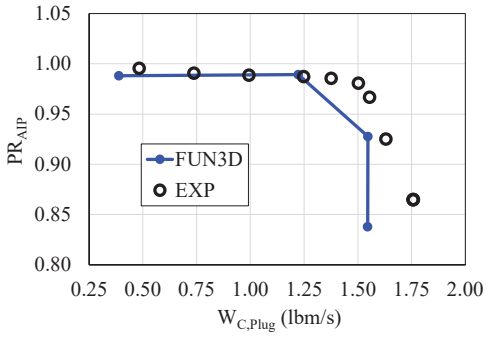

(c) PR_{AIP}.

Figure 53. Inlet distortion and pressure recovery predictions as a function of corrected flow rate; medium grid, $M = 0.8$, Re = 4,191,000/ft, $\alpha = 3°$, and $\beta = 0°$.

The results of the SPR sweeps performed for Mach 1.18 are provided in Figure 54. Similar to the results shown for Mach 0.8, the FUN3D predictions agree better at lower flow rates and appear to diverge from the experimental data at higher flow rates. Again, the lines can be misleading since there are not enough data to fully

resolve the nonlinear portions.

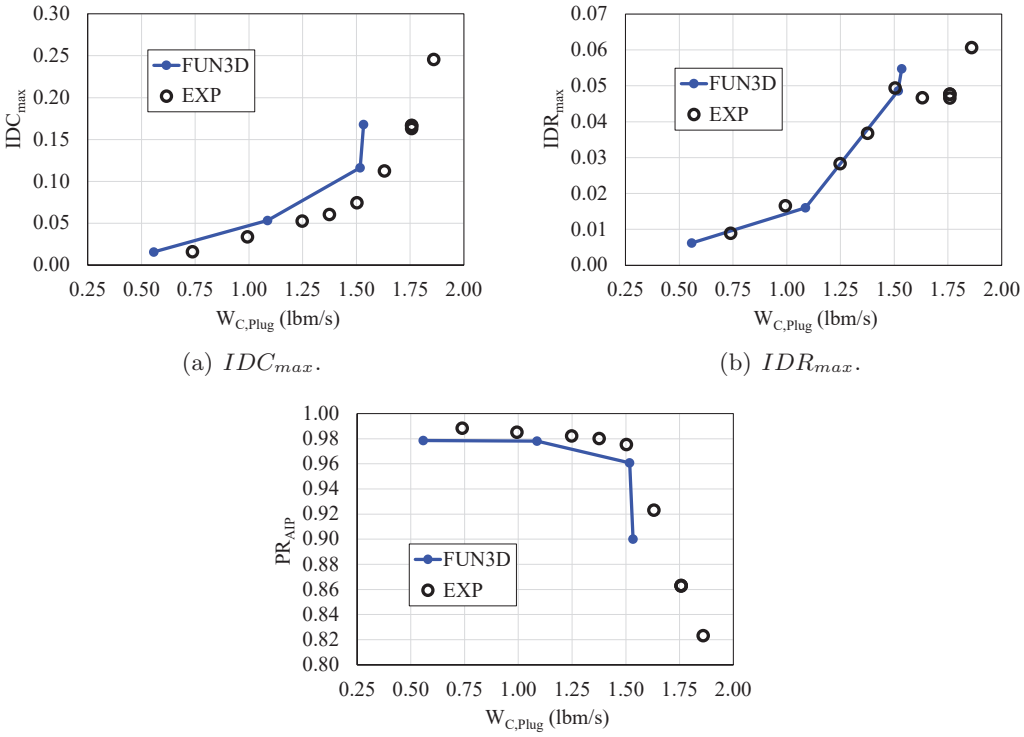

(a) IDC_{max}.

(b) IDR_{max}.

(c) PR_{AIP}.

Figure 54. Inlet distortion and pressure recovery predictions as a function of corrected flow rate; medium grid, $M = 1.18$, Re = 4,838,000/ft, $\alpha = 3°$, and $\beta = 0°$.

Finally, the results of the SPR sweeps performed for Mach 1.46 are provided in Figure 55. The results show that the FUN3D predicted trends agree favorably with the trends from the experiment. However, the separation between the predictions and the experimental data is noticeably larger for this Mach number. This observation agrees with the results of the grid refinement study.

For all of the results shown thus far, the specified mass flow rate from the CFD simulations corresponds to the integrated value at the outflow boundary. Previous studies have shown that this method can be inconsistent with experiment due to limited instrumentation in the wind tunnels. For example, some inlet tests calculate the mass flow rate from the 40-probe rake along with static pressure measurements at the AIP. When comparing this mass flow rate to an integrated value in CFD, there will be differences due to the higher resolution of the flow field at the AIP in the CFD results.

The wind tunnel test considered in this work employed a mass flow plug. The mass flow rate was defined by a calibration of the plug, which would consist of a finite number of pressure measurements. So, to be consistent with the test, we would need to calculate the mass flow rate using the same method. However, the

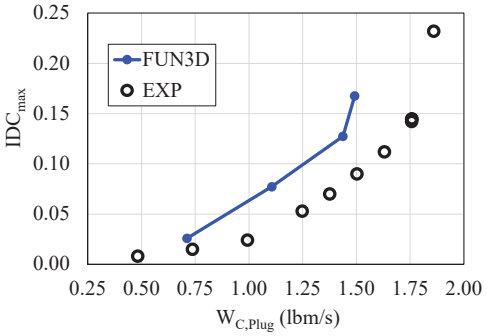

(a) IDC_{max}.

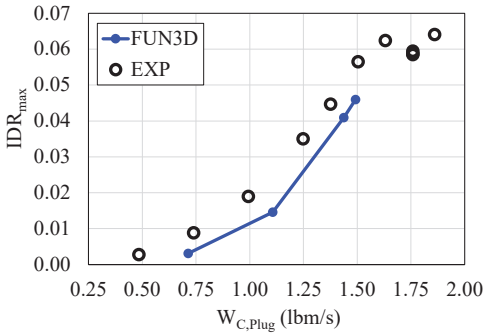

(b) IDR_{max}.

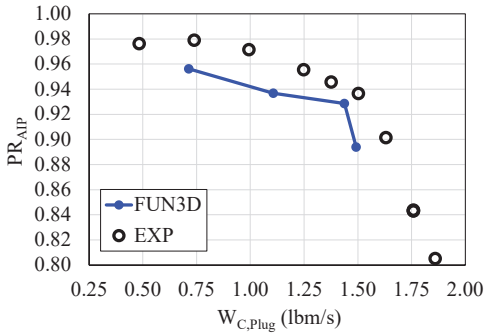

(c) PR_{AIP}.

Figure 55. Inlet distortion and pressure recovery predictions as a function of corrected flow rate; medium grid, $M = 1.46$, Re = 4,947,000/ft, $\alpha = 2°$, and $\beta = 0°$.

mass flow plug is not included in the present analyses. Therefore, the method of calculating the mass flow rate from the 40-probe rake measurements was utilized for this part of the study. The goal of this study is to assess the trends shown in Figures 53 through 55, but with the mass flow rate calculated from the 40-probe rake. The method used to calculate the mass flow rate is provided in Equations 7 through 10, which is the same method used for comparison to experimental data for an s-duct geometry simulated for the 4th Propulsion Aerodynamics Workshop (PAW4) [17]. Note that the provided equations were utilized to calculate the mass flow rate at the AIP for both the FUN3D predictions and the experimental results.

$$P_{t,AIP,avg} = \frac{1}{40}\sum_{40}^{i=1} P_{t,AIP_i} \tag{7}$$

$$P_{AIP,avg} = \frac{1}{8}\sum_{8}^{i=1} P_{AIP_i} \tag{8}$$

$$M_{AIP} = \sqrt{\frac{2}{\gamma - 1}\left(\left(\frac{P_{t,AIP,avg}}{P_{AIP,avg}}\right)^{\frac{\gamma-1}{\gamma}} - 1\right)} \tag{9}$$

$$\dot{m}_{AIP} = \frac{P_{t,AIP,avg}}{\sqrt{RT_{t,\infty}/\gamma}} A_{AIP} M_{AIP} \left(1 + \frac{\gamma - 1}{2} M_{AIP}^2\right)^{\frac{\gamma+1}{2(1-\gamma)}} \tag{10}$$

The updated results of the SPR sweeps performed for Mach 0.8 are provided in Figure 56. Comparing the results provided in Figure 56 to the those shown in Figure 53, the FUN3D predicted trends agree favorably over the entire range shown. The one exception is for the IDR_{max} predicted trend, which still appears to diverge from the experimental results for the two highest flow rates.

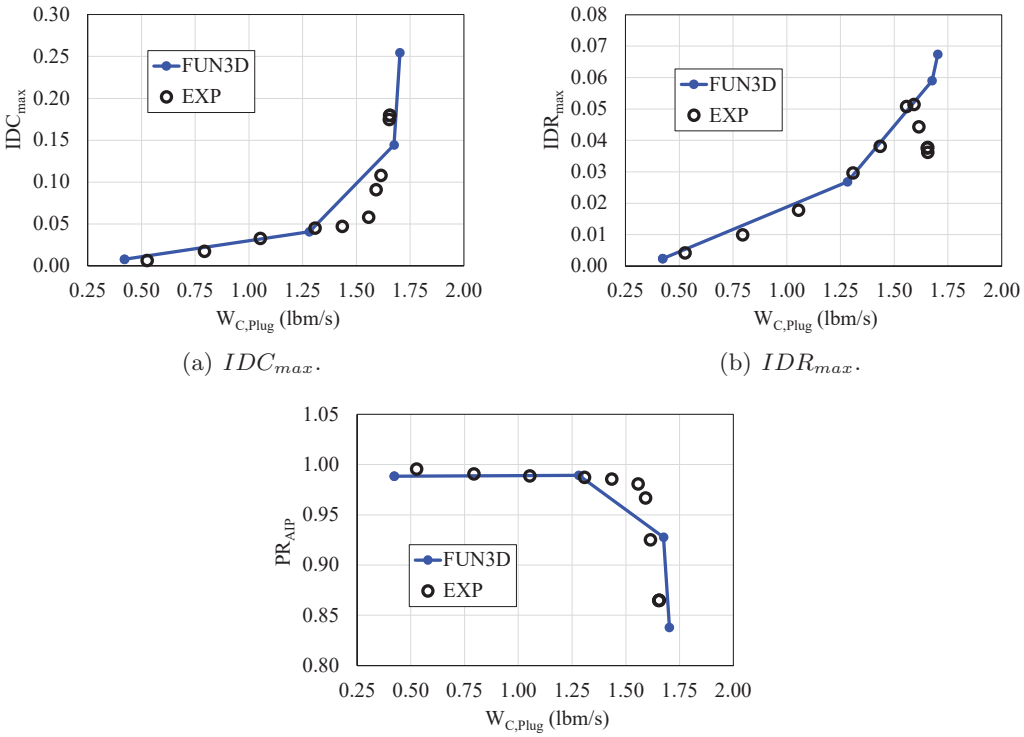

(a) IDC_{max}.

(b) IDR_{max}.

(c) PR_{AIP}.

Figure 56. Inlet distortion and pressure recovery predictions as a function of corrected flow rate; medium grid, $M = 0.8$, Re = 4,191,000/ft, $\alpha = 3°$, and $\beta = 0°$.

Similarly, the Mach 1.18 comparisons shown in Figure 57 illustrate improved agreement between FUN3D and the experimental data. In this case, the trends appear to agree favorably over the entire range of flow rates.

Finally, the Mach 1.46 comparisons provided in Figure 58, while showing the largest differences between the FUN3D and experimental values, show improvements in the trends when plotting against the adjusted mass flow rate.

The results of this study illustrate the significance in the method used to define the mass flow rate. For a case such as this, where the data were available prior to the analyses, the proper strategy for the FUN3D predictions would be to use the available data to calculate the target mass flow rate instead of performing simula-

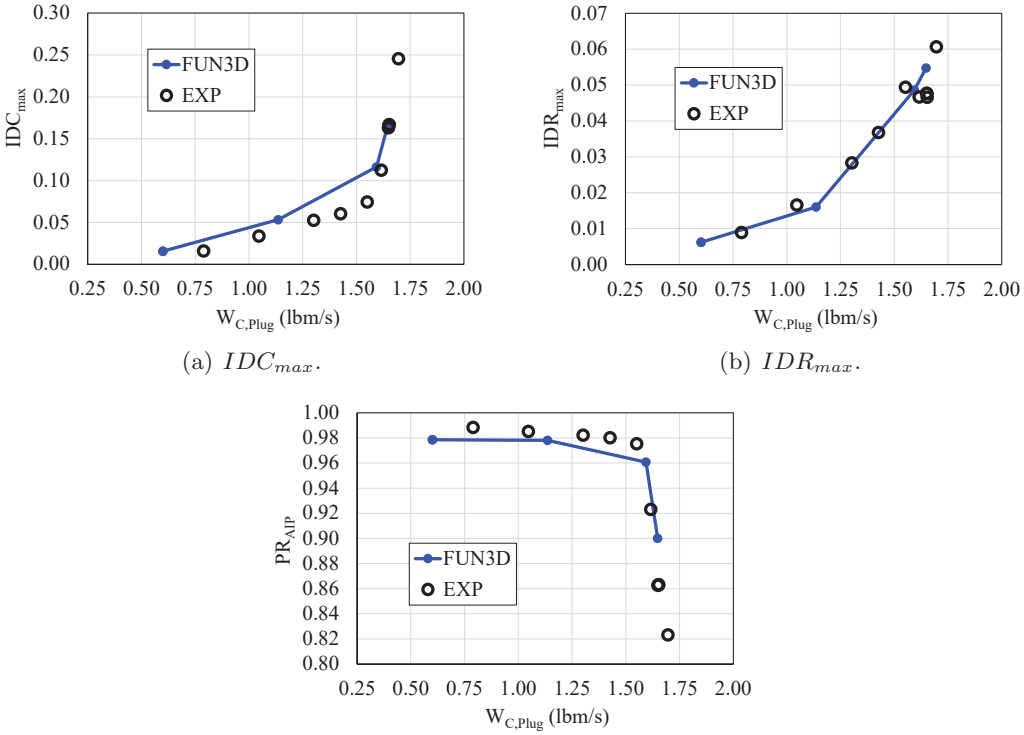

(a) IDC_{max}. (b) IDR_{max}.

(c) PR_{AIP}.

Figure 57. Inlet distortion and pressure recovery predictions as a function of corrected flow rate; medium grid, $M = 1.18$, Re = 4,838,000/ft, $\alpha = 3°$, and $\beta = 0°$.

tions using the nominal value from the experiment. However, the experimental data are not always available prior to performing the simulations. Either way, matching the mass flow rate based on pressure measurements from common locations will generally provide the most consistent comparisons; especially for cases with significant distortion at the AIP.

Of the three Mach numbers considered for this work, the results for Mach 1.46, again, showed the largest differences relative to the experimental data. As a result, this condition was selected for further study to assess the impact of BC type, turbulence model, and flux limiter on the predicted inlet performance. The goal is to determine if there are modeling parameters that would provide improved predictions relative to the baseline simulations that have been discussed so far. These studies are discussed further in the following subsections.

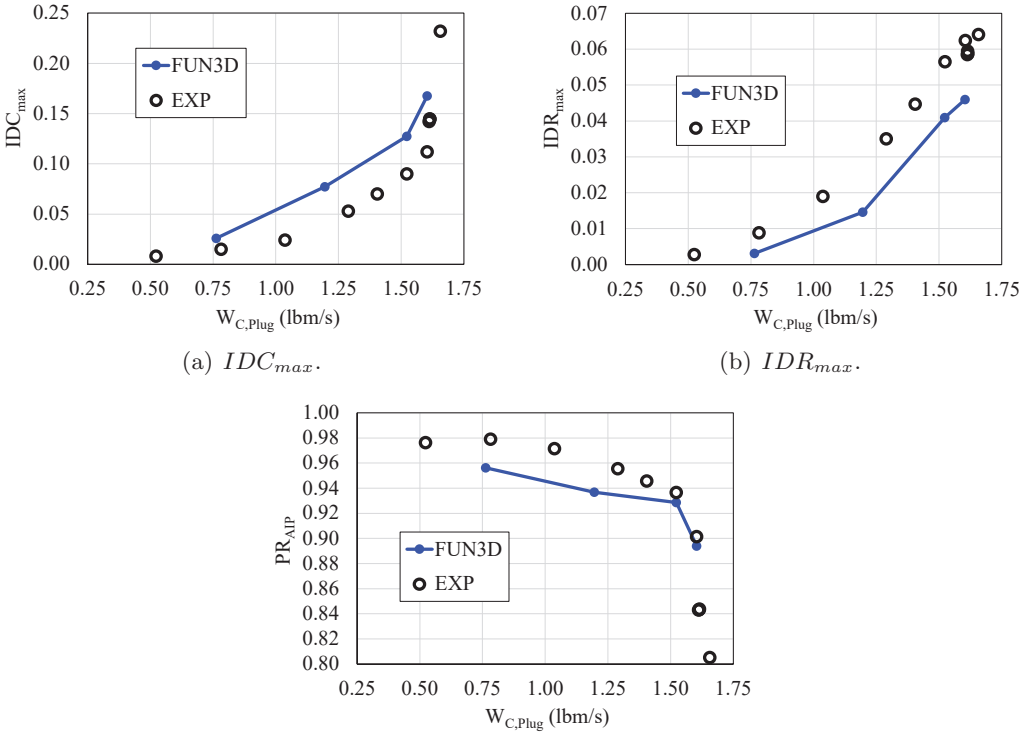

(a) IDC_{max}.

(b) IDR_{max}.

(c) PR_{AIP}.

Figure 58. Inlet distortion and pressure recovery predictions as a function of corrected flow rate; medium grid, $M = 1.46$, Re = 4,947,000/ft, $\alpha = 2°$, and $\beta = 0°$.

4.2.5 Outflow BC Study

For the BC type study, the Mach boundary condition was compared to the SPR condition over a range of mass flow rates. Note that this study was performed for a Mach number of 1.46 and considered the adjusted mass flow rate at the AIP for comparison to experimental data. Mach number values of 0.2, 0.3, 0.4, and 0.5 at the outflow boundary were found to provide an adequate range of mass flow rates to enable comparisons to SPR sweep results shown in Figure 58.

The results of the BC type study are provided in Figure 59, which show that the two BCs produce similar trends. For the IDC_{max} and PR_{AIP} results, the two BCs compare well except for at the highest mass flow rate, where the SPR BC agrees better with the experiment. Interestingly, the Mach BC produces a trend that agrees better with the experimental data for IDR_{max}. However, there does not appear to be a definitive improvement in the trends when using the Mach BC for this problem.

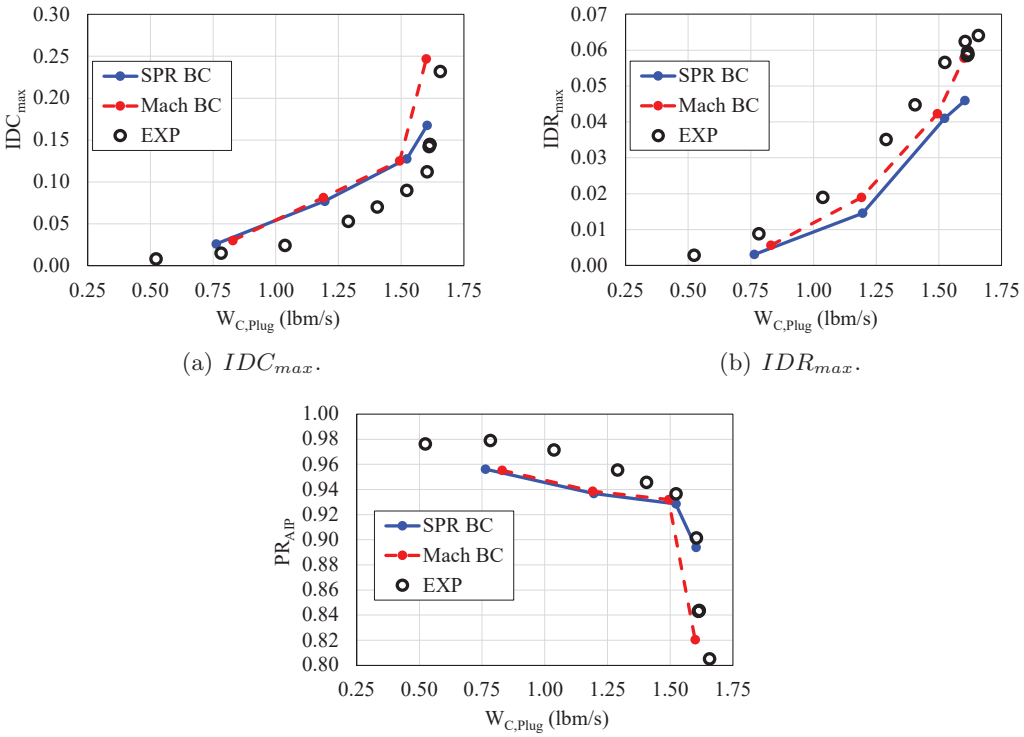

(a) IDC_{max}.

(b) IDR_{max}.

(c) PR_{AIP}.

Figure 59. Inlet distortion and pressure recovery predictions as a function of corrected flow rate and boundary condition type; medium grid, $M = 1.46$, Re = 4,947,000/ft, $\alpha = 2°$, and $\beta = 0°$.

4.2.6 Turbulence Model Study

The next study considered four turbulence models simulated over the range of SPR values provided in Table 4. Note that only the Mach 1.46 condition was considered for this study. The four turbulence models included the baseline model (SA-neg-RC-QCR), the one equation Spalart-Allmaras model with negative provisions and no corrections (SA-neg), the two-equation Menter SST model with vorticity source term (SST-V) [18] , and the SSG/LRR-ω seven-equation, omega-based, full Reynolds Stress Model (RSM) [15].

The results of the turbulence model study are provided in Figure 60, which shows the FUN3D predicted values of IDC_{max}, IDR_{max}, and PR_{AIP} plotted against the adjusted mass flow rate for the four turbulence models considered. For all three metrics, the SA-neg and SA-neg-RC-QCR models agree very well with only slight differences. The SST-V model appears to perform the worst for this problem since the trends produced do not agree with any of the other models or the experimental data. Finally, the RSM results show favorable agreement with both the experimental data and SA-neg model variants. However, the RSM exhibits a tendency to underpredict the pressure recovery relative to the other models. Based on the results shown here, there is no indication that changing turbulence model from the

selected baseline model (SA-neg-RC-QCR) will provide improved predictions.

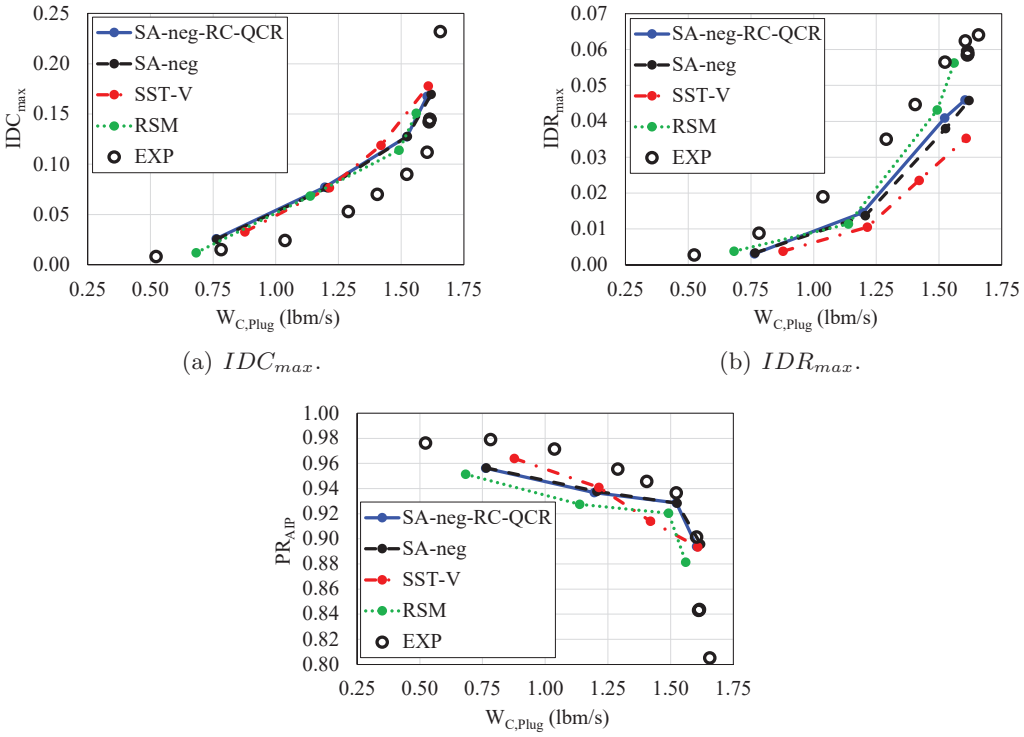

(a) IDC_{max}.

(b) IDR_{max}.

(c) PR_{AIP}.

Figure 60. Inlet distortion and pressure recovery predictions as a function of corrected flow rate and turbulence model; medium grid, $M = 1.46$, Re = 4,947,000/ft, $\alpha = 2°$, and $\beta = 0°$.

4.2.7 Flux Limiter Study

For the flux limiter study, three flux limiters were simulated over a range of fixed SPR values. The three flux limiters included the baseline limiter for this study (hvanleer), the stencil-based van Albada limiter with heuristic pressure limiter (hvanalbada), and the stencil-based Venkatakrishnan limiter with heuristic pressure limiter (hvenkat) [19].

The results of the flux limiter study are provided in Figure 61, which shows the FUN3D predicted values of IDC_{max}, IDR_{max}, and PR_{AIP} plotted against the adjusted mass flow rate for the three flux limiters considered. The hvanleer and hvanalbada flux limiters produce nearly identical predictions for IDC_{max}, IDR_{max}, and PR_{AIP}. However, the hvenkat flux limiter exhibits differences relative to the other two models. The hvenkat trends, in general, do not agree with the experimental trends or the trends produced using the other two models. Similar to the findings of the previous studies, the results of this study do not provide a path forward for improved predictions.

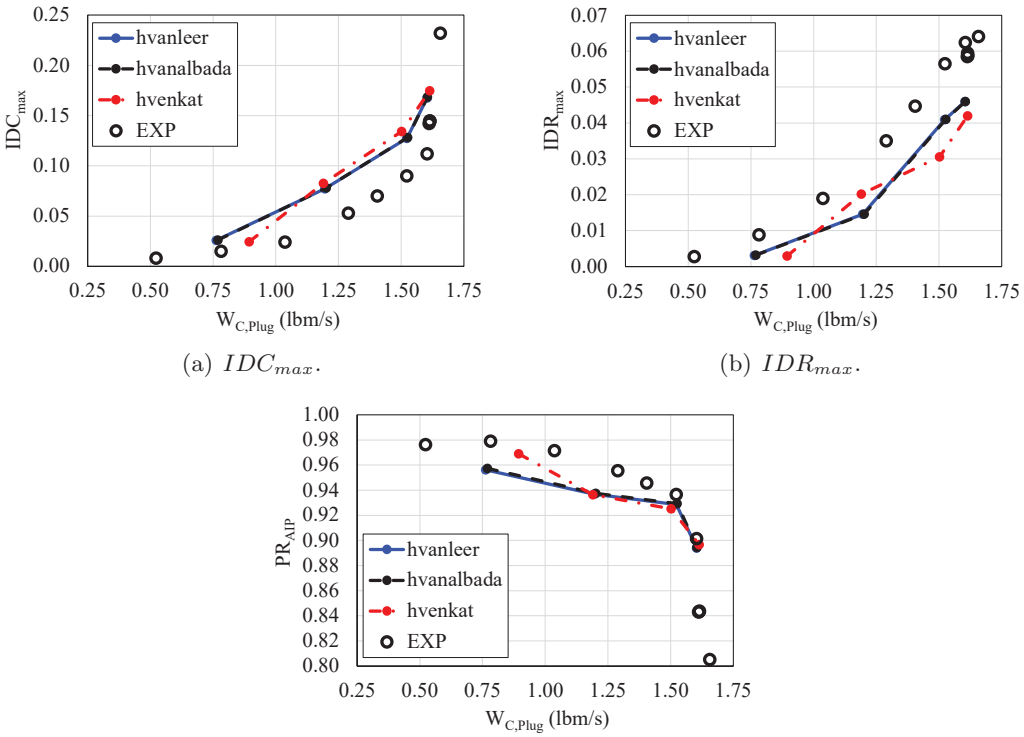

(a) IDC_{max}.

(b) IDR_{max}.

(c) PR_{AIP}.

Figure 61. Inlet distortion and pressure recovery predictions as a function of corrected flow rate and flux limiter; medium grid, $M = 1.46$, Re = 4,947,000/ft, $\alpha = 2°$, and $\beta = 0°$.

4.2.8 Mass Flow Plug Study

The final study performed for the C607 propulsion model considered both versions of the computational geometries shown in Figures 32 and 33b. Once again, the outflow BC version of the model, shown in Figure 32, was used to perform simulations over the range of SPR values provided in Table 4 for a Mach number of 1.46. The mass flow plug geometry was then simulated over a range of plug locations. The mass flow plug assembly, illustrated in Figure 33a, was mounted onto a linear ball-screw mechanism that allowed for up to 2.5 inches of translation. To enable comparisons over a range of mass flow rates, five discrete plug positions ranging from 0.5 to 2.5 inches of forward translation were simulated. This required five distinct grids, which were generated using Heldenmesh™ v3.08 to match the refinement level of the medium grid created for the baseline computational geometry. Note that the additional viscous surfaces in the mass flow plug geometry resulted in an increase in the size of the grids relative to the outflow version of the geometry. The resulting grids for the mass flow plug geometry consisted of roughly 15.5 million nodes for the half-span model with slight deviations depending on the location of the plug.

The results of this study are provided in Figure 62, which shows comparisons of the FUN3D predictions and the experimental data over a range of adjusted mass

flow rate for both versions of the geometry. The FUN3D predictions illustrate favorable agreement for the two versions of the geometry over the range of mass flow rates considered, with the exception of the highest mass flow rate, where the predictions from the two models show differences for all three metrics. Based on this limited study, including the mass flow plug in the computational model does not appear to offer a benefit over the application of the outflow boundary. This result has important implications since the outflow boundary significantly simplifies the simulations by reducing the model complexity and allowing a range of mass flow rates to be obtained without geometry modifications.

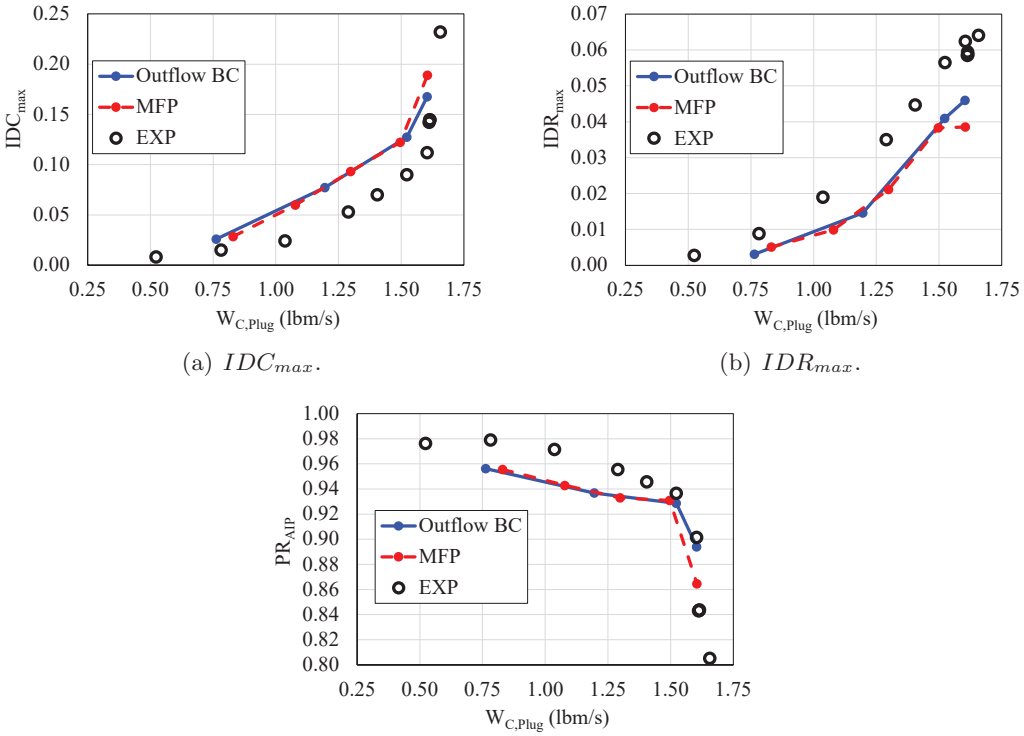

(a) IDC_{max}.

(b) IDR_{max}.

(c) PR_{AIP}.

Figure 62. Inlet distortion and pressure recovery predictions as a function of corrected flow rate and inlet model; medium grid, $M = 1.46$, Re = 4,947,000/ft, $\alpha = 2°$, and $\beta = 0°$.

4.3 Summary

The results of the studies performed for the C607 propulsion model were discussed in the previous subsections. The grid refinement study was performed at freestream Mach numbers of 0.8, 1.18, and 1.46. For each Mach number, the PID-controller in FUN3D was employed to match a target corrected flow rate of 1.25 lb_m/s at the outflow boundary. The results show that grid convergence was not achieved for any case. And while the total pressure distributions illustrate qualitative agreement

between the FUN3D predictions and experimental data, the predictions generally trend away from the experimental data with increasing grid refinement. Additionally, the differences between the FUN3D predictions and experimental data were observed to increase with increasing Mach number. The medium grid was selected to perform the additional studies to enable a broader evaluation of FUN3D for this model by reducing the computational cost relative to the larger grids. The results of the FUN3D input parameter sweeps did not indicate a path forward for improved predictions. Finally, the comparisons between the outflow boundary model and the mass flow plug model illustrated favorable agreement.

5 Summary of Findings

This work investigated the impact of outflow boundary condition and location, grid refinement, turbulence model, and flux limiter, when applicable, on the predicted performance for installed inlet applications. Two configurations were considered; a wall-mounted BLI inlet and the C607 propulsion model tested in the 8x6 Supersonic Wind Tunnel at the NASA Glenn Research Center [1]. For the BLI inlet problem, simulations were performed for a test section Mach number of 0.58 and a mass flow rate of 8.82 $\mathrm{lb_m/s}$. The results showed a minimal impact of grid refinement on the predicted inlet performance. Note that this result corresponds to a constant mass flow rate through the inlet, which was obtained using the PID controller available in FUN3D for each grid refinement. Additionally, the outflow boundary location study showed that the solution at the AIP was not significantly impacted by the outflow boundary location as long as it was not placed at the location of the AIP. Finally, the results of the turbulence model study showed differences between the SA-neg-RC-QCR predictions relative to the other three turbulence models considered. Interestingly, the SA, SST, and RSM models agreed favorably. However, it is unclear which model would be most suitable for this problem given the lack of comparisons to experimental data.

The results of the studies performed for the C607 propulsion model showed that while the FUN3D predictions qualitatively agree with the experimental data, FUN3D showed a tendency to overpredict IDC_{max} and underpredict both IDR_{max} and PR_{AIP}. It is important to note that this problem poses significant challenges for RANS solvers due to the presence of shocks and flow separation in the inlet. However, these flow features are not specific to inlet problems. In order to assess the accuracy of FUN3D for predicting inlet flows, the components of the problem specific to this type of simulation need to be considered. For the work performed, the outflow boundary condition is the only modeling component specific to inlet flows. A study was performed comparing predictions obtained by modeling the mass flow plug to those obtained using an outflow boundary condition to control the mass flow rate. The results illustrated favorable agreement between the two models. Based on this, the components specific to inlet flows do not seem to be significantly contributing to the differences observed between the FUN3D predictions and the experimental data. The impact of outflow boundary location was reevaluated for this geometry, which, once again, showed that the solution at the AIP was not impacted by the

location of the outflow boundary. However, this assumes that the outflow boundary does not coincide with the AIP. Finally, the results of the boundary condition type, turbulence model, and flux limiter studies did not indicate a path for improved predictions for this case.

Acknowledgments

This work was supported by the NASA Commercial Supersonic Technology project. Considerable appreciation is extended to the NASA-Langley Mid-range Computing K-cluster management and system administrators for providing an extremely productive computing environment for performance of this body of work.

References

1. Castner, R. S.; Simerly, S.; and Rankin, M.: Supersonic inlet test for a quiet supersonic transport technology demonstrator in the nasa glenn 8-foot by 6-foot supersonic wind tunnel. *2018 Applied Aerodynamics Conference*, 2018, p. 2850.

2. Carlson, J.-R.: Automated Boundary Conditions for Wind Tunnel Simulations. NASA TM–2018-219812, Mar. 2018.

3. Roe, P. L.: Approximate Riemann Solvers, Parameter Vectors, and Difference Schemes. *J. Comp. Phys.*, vol. 43, 1981, pp. 357–372.

4. van Leer, B.: Towards the Ultimate Conservative Difference Schemes V. A second order sequel to Godunov's Method. *J. Comp. Phys.*, vol. 32, 1979, pp. 101–136.

5. Spalart, P. R.; and Allmaras, S. R.: A One-Equation Turbulence Model for Aerodynamic Flows. *Recherche Aerospatiale*, vol. 1, 1994, pp. 5–21.

6. M. L. Shur, M. K. Strelets, A. K. T.; and Spalart, P. R.: Turbulence Modeling in Rotating and Curved Channels: Assessing the Spalart-Shur Correction. *AIAA Journal*, vol. 38, no. 5, 2000, pp. 784–792.

7. Spalart, P. R.: Strategies for Turbulence Modelling and Simulation. *International Journal of Heat and Fluid Flow*, vol. 21, 2000, pp. 252–263.

8. Biedron, R. T.; Carlson, J.-R.; Derlaga, J. M.; Gnoffo, P. A.; Hammond, D. P.; Jones, W. T.; Kleb, W.; Lee-Rausch, E. M.; Nielsen, E. J.; and Park, M. A.: FUN3D Manual: 13.2. NASA TM–2017-219661, Aug. 2017.

9. `https://fun3d.larc.nasa.gov`. Accessed: 2017-03-20.

10. Owens, L. R.; Allan, B. G.; and Gorton, S. A.: Boundary-layer-ingesting inlet flow control. *Journal of Aircraft*, vol. 45, no. 4, 2008, pp. 1431–1440.

11. Gas Turbine Engine Inlet Flow Distortion. SAE ARP-1420, Society of Automotive Engineers, March 1978.

12. https://heldenaero.com/heldenmesh/. Accessed: 2021-09-28.

13. Samareh-Abolhassani, J.: GridTool: A Surface Modeling and Grid Generation Tool. *NASA. Lewis Research Center, Surface Modeling, Grid Generation, and Related Issues in Computational Fluid Dynamic (CFD) Solutions*, 1995.

14. Menter, F. R.: Two-Equation Eddy-Viscosity Turbulence Models for Engineering Applications. *AIAA Journal*, vol. 32, no. 8, Aug. 1994, pp. 1598–1605.

15. Eisfeld, B.; and Rumsey, C. L.: Length-scale correction for Reynolds-stress modeling. *AIAA Journal*, vol. 58, no. 4, 2020, pp. 1518–1528.

16. Moore, M. T.: Distortion Data Analysis. , GENERAL ELECTRIC CO CINCINNATI OH AIRCRAFT ENGINE BUSINESS GROUP, 1973.

17. Carter, M. B.; Bozeman, M. D.; and Carlson, J.-R.: USM3D and FUN3D Results for S-duct Configuration. , July 2018.

18. Menter, F. R.: Improved two-equation k-omega turbulence models for aerodynamic flows. NASA TM-103975, Oct. 1992.

19. Venkatakrishnan, V.: Convergence to Steady State Solutions of the Euler Equations on Unstructured Grids with Limiters. *J. Comp. Phys.*, vol. 118, 1995, pp. 120–130.

REPORT DOCUMENTATION PAGE	Form Approved OMB No. 0704–0188

1. REPORT DATE *(DD-MM-YYYY)*	2. REPORT TYPE	3. DATES COVERED *(From - To)*
01-03-2022	Technical Memorandum	

4. TITLE AND SUBTITLE
Identification of Best Practices for Predicting Inlet Performance Using FUN3D Part 2: Installed Inlets.

5a. CONTRACT NUMBER

5b. GRANT NUMBER

5c. PROGRAM ELEMENT NUMBER

6. AUTHOR(S)
Michael D. Bozeman Jr. and Jan-Renee Carlson

5d. PROJECT NUMBER

5e. TASK NUMBER

5f. WORK UNIT NUMBER

7. PERFORMING ORGANIZATION NAME(S) AND ADDRESS(ES)
NASA Langley Research Center
Hampton, Virginia 23681-2199

8. PERFORMING ORGANIZATION REPORT NUMBER
L–

9. SPONSORING/MONITORING AGENCY NAME(S) AND ADDRESS(ES)
National Aeronautics and Space Administration
Washington, DC 20546-0001

10. SPONSOR/MONITOR'S ACRONYM(S)
NASA

11. SPONSOR/MONITOR'S REPORT NUMBER(S)
NASA/TM–2022–20210022214

12. DISTRIBUTION/AVAILABILITY STATEMENT
Unclassified-Unlimited
Subject Category
Availability: NASA STI Program (757) 864-9658

13. SUPPLEMENTARY NOTES
An electronic version can be found at http://ntrs.nasa.gov.

14. ABSTRACT

A series of studies were performed to assess the impacts of boundary condition type and placement, grid refinement, and modeling parameters such as turbulence model and flux limiter on the predicted inlet performance for installed inlet configurations using the FUN3D flow solver. Two configurations were considered for the study; a wall-mounted Boundary Layer Ingestion (BLI) inlet and the C607 propulsion model tested in the 8x6 Supersonic Wind Tunnel at the NASA Glenn Research Center. The results of the studies were to be used to recommend best practices, as well as to assess the accuracy of FUN3D for inlet predictions. The results of BLI inlet studies showed a minimal impact of grid refinement on the predicted inlet performance for a constant mass flow rate through the inlet. For the C607 propulsion model, the results showed that while the FUN3D predictions at the Aerodynamic Interface Plane (AIP) qualitatively agree with the experimental data, FUN3D showed a tendency to overpredict the circumferential distortion metric (IDC_{max}) and underpredict both the radial distortion metric (IDR_{max}) and the pressure recovery at the AIP (PR_{AIP}), with the differences between FUN3D and the experimental data increasing with increasing grid refinement and Mach number. Additionally, the outflow boundary location studies performed for both geometries showed that the solution at the AIP was not significantly impacted by the outflow boundary location as long as it was not placed at the location of the AIP. The modeling parameter studies did not indicate a path forward for improved predictions for either inlet configuration. Finally, comparisons between the mass flow plug and outflow geometry versions of the C607 propulsion model illustrated favorable agreement, which indicates that the differences observed are not caused by the outflow boundary model for this problem. This problem poses significant challenges to Reynolds-averaged Navier-Stokes (RANS) solvers due to the presence of shocks and flow separation in the inlet.

15. SUBJECT TERMS					
16. SECURITY CLASSIFICATION OF:			17. LIMITATION OF ABSTRACT	18. NUMBER OF PAGES	19a. NAME OF RESPONSIBLE PERSON
a. REPORT	b. ABSTRACT	c. THIS PAGE			STI Information Desk (help@sti.nasa.gov)
U	U	U	UU		19b. TELEPHONE NUMBER *(Include area code)* (757) 864-9658